

SNOWFALL OVER THE CENTRAL GREENLAND ICE SHEET

by
Claire Pettersen

A dissertation submitted in partial fulfillment of
the requirements for the degree of

Doctor of Philosophy
(Atmospheric and Oceanic Sciences)

at the
UNIVERSITY OF WISCONSIN – MADISON
2017

Date of final oral examination: October 23, 2017

The dissertation is approved by the following members of the Final Oral Committee:

Grant W. Petty, Professor, Atmospheric and Oceanic Sciences

Ankur R. Desai, Professor, Atmospheric and Oceanic Sciences and Nelson Institute
for Environmental Sciences

Tristan S. L'Ecuyer, Associate Professor, Atmospheric and Oceanic Sciences

Daniel J. Vimont, Professor, Atmospheric and Oceanic Sciences

Ralf Bennartz, Professor, Earth & Environmental Science, Vanderbilt University

ProQuest Number: 10640544

All rights reserved

INFORMATION TO ALL USERS

The quality of this reproduction is dependent upon the quality of the copy submitted.

In the unlikely event that the author did not send a complete manuscript and there are missing pages, these will be noted. Also, if material had to be removed, a note will indicate the deletion.



ProQuest 10640544

Published by ProQuest LLC (2018). Copyright of the Dissertation is held by the Author.

All rights reserved.

This work is protected against unauthorized copying under Title 17, United States Code
Microform Edition © ProQuest LLC.

ProQuest LLC.
789 East Eisenhower Parkway
P.O. Box 1346
Ann Arbor, MI 48106 – 1346

Abstract

Precipitation over the central Greenland Ice Sheet (GIS) is arguably not well-understood or constrained. To understand current and future changes in precipitation occurrence and accumulation patterns over the GIS, associated clouds and atmospheric processes must be investigated. Comprehensive multi-instrument, remote-sensing and in-situ ground-based observations can provide insight into local atmospheric processes. These observations can be combined with reanalysis products to gain a regional perspective. This work focuses on identifying, characterizing, and classifying ice hydrometeors primarily using passive microwave radiometer data from Summit Station in central Greenland. The precipitation observed over the GIS partitions into two distinct regimes tied to specific cloud characteristics: deep, fully-glaciated ice clouds (IC) and shallow, mixed-phase clouds with supercooled cloud liquid water (CLW). The occurrence and accumulation statistics of the precipitation regimes are identified and quantified. Cloud characteristics from each precipitation regime are illustrated using additional instrument data from five years of observations from the Integrated Characterization of Energy, Clouds, Atmospheric state, and Precipitation at Summit (ICECAPS) project. Additionally, regional meteorological conditions are examined using reanalysis products and show different large-scale dynamics corresponding to each snow type. Further work suggests that the IC snow events are likely tied to individual storm tracks located in the Baffin Bay or interacting with the southern tip of Greenland. In contrast, the CLW snow events are tied to regional conditions present during the negative phase of the North Atlantic Oscillation, with onshore and upslope winds from the south and southwest of Greenland and large areas of high 500 mb

geopotential heights. These results help illustrate the origin of precipitating clouds and how they reach the central GIS. Additionally, this work lends insight into the primary mechanisms needed for producing precipitation from the coast of Greenland to Summit Station. This work implies that accumulation in the central GIS is tied to both specific storm tracks and climate oscillations, which may show different responses under climate change.

Acknowledgements

I have been fortunate enough to have many supportive people, both in my personal and professional lives, who have helped me throughout this entire process:

Within the Atmospheric and Oceanic Sciences department, I would to thank all the support staff for their continuous help on the administrative end of this process. The office staff have always been accommodating of my many questions and requests and that is appreciated. The faculty in the department each played a role, either through useful scientific discussions or through the enriching graduate level classes of which I was fortunate enough to attend. I have enjoyed all of my time in the classroom in this department and have found the lectures to be rewarding and fulfilling. Finally, I have been privileged to share this experience with a wonderful group of talented graduate students. I especially appreciate the camaraderie and friendship of soon-to-be-Drs. Erin Thomas, Melissa Breeden, and Elin McIlhattan, and former students Dr. Nathaniel Miller, Dr. John Rausch, Dr. Aronne Merrelli, Ms. Elena Wilmot, and Dr. Alex Karambelas.

Within the Space Science Engineering Center, I would like to thank all of my colleagues who have been supportive of my later-in-life career shift. Especially, to my colleagues Dr. Joe Taylor, Dr. Jon Gero, Dr. David Tobin, Mr. Doug Adler, Mr. Nic Ciganovich, Mr. Don Thielman, Dr. Tim Wagner, and Dr. Hank Revercomb. I would like to also mention the unwavering backing by my supervisor, Mr. Fred Best. When I approached Fred about going back to graduate school part-time and reducing my workload, he was fully supportive and encouraging.

Within my Madison and friend community, there are far too many wonderful people to name – but please know that you all kept me sane. Professional friends: former

mentor Dr. Kael Hanson, Mechanical Engineering professor Dr. Heidi Ploeg, Earth Science Women's Network co-director and Geography professor Dr. Erica Marin-Spiotta, Michigan Technological University professor Dr. Mark Kulie, current colleague Dr. Norm Wood, and TAMU professor Dr. Anita Rapp were all unceasing in their support.

Within my co-author groups, I cannot thank you all enough for helping me to curate papers of which I am very proud. I appreciate all the insights on Arctic cloud and precipitation from Dr. Matthew Shupe, as well as his contagious excitement for studying Greenland, cloud radars, and mixed-phase clouds. Dr. Dave Turner has been an invaluable wealth of knowledge for all things MWR and cloud physics, and always made time to give useful and constructive feedback. Dr. Von Walden and Dr. Mark Kulie have been wonderful co-authors with endless positive and complimentary feedback on this work, as well as useful critiques. I appreciate all their efforts.

Within my dissertation committee, I have been fortunate to have interesting and useful conversations with all of my members. Dr. Grant Petty has always taken the time to sit and talk through my research and offer stimulating insights. I have appreciated how quickly and effectively he has aided in any administrative work as well. Grant has always been very willing and accommodating of my various field-work assignments that would occasionally conflict with his classes, as he realizes the importance and benefits of such work. Additionally, Grant took on the advisory role for my Ph.D. when Dr. Ralf Bennartz left the University of Wisconsin – and for this I am very grateful. Dr. Ankur Desai has a contagious love of atmospheric science and has encouraged me to chase interesting proposals and research. When I was considering returning to graduate school I took a class with Ankur and I absolutely loved it, which effectively led to my enrollment the following

year. Dr. Dan Vimont has been an excellent resource for topics outside my wheelhouse and I have had many interesting discussions with him regarding my work (and other radar work). Dan is also instrumental in my return to graduate school as he overheard me in a local coffee shop tell a friend I was considering a career shift and he recommended Ankur's class as a trial run. Dr. Tristan L'Ecuyer and I met at a conference prior to his joining the faculty at University of Wisconsin and I was immediately struck with how positive and excited he was about atmospheric science. I am fortunate that since that conference, Tristan has remained an amazing friend and colleague who always made time to act as a sounding board for my research ideas. I feel very fortunate to have Tristan as a mentor, colleague, and friend and look forward to continuing to have exciting scientific discussions in the future.

I have been lucky to have Dr. Ralf Bennartz as my advisor. Even though Ralf left the University of Wisconsin, we have been able to effectively work together long-distance on some very interesting ICECAPS science. Ralf has seemingly had confidence in my abilities from day one, when early on he asked if I could deploy last-minute to Summit Station in the middle of winter and maybe fix the cloud radar, to which I said "YES!" and "ABSOLUTELY YES!" The resonance of his confidence in my abilities remained with me throughout this process and helped to fuel much of my motivation and research. Ralf has been open to my ideas and thoughts on research direction since I first started graduate school, and for this I am grateful.

Finally, I wanted to say I am very fortunate to have an amazing partner who also happens to work in my same field, albeit in a different wavelength – Dr. Aronne Merrelli. Aronne went through a similar process of career change later in life and understood that it

would be tough to live through it again, albeit vicariously, but stuck it out regardless. Too many things to outline here, so I will just thank Aronne for all he has done.

This work is dedicated to my Grandmother, Ella Williams, and my Grandpa, Frank Pettersen.

Table of Contents

Abstract	i
Acknowledgements	iii
List of Figures	ix
List of Tables	xv
Chapter 1	1
1 Introduction – Arctic response to climate change	1
Chapter 2	4
2 Greenland Ice Sheet mass balance	4
2.1 Historical data and recent trends	4
2.1.1 Extreme events.....	6
2.2 Precipitation over the central GIS	8
2.2.1 Arctic Cloud Phase	9
2.2.2 Precipitation relationship to climate indexes and storm systems.....	11
2.2.3 Remote-sensing of cloud and precipitation processes	14
2.3 Objectives of this work	16
Chapter 3	27
3 Datasets and Methods	27
3.1 ICECAPS project and instrument suite	27
3.1.1 Microwave radiometers	28
3.1.2 Millimeter cloud radar.....	30
3.1.3 Ceilometer	31
3.1.4 Radiosondes.....	31
3.1.5 Precipitation Occurrence Sensor System	32
3.1.6 Ice Particle Imaging Camera	32
3.1.7 Surface Meteorology Data and Observations.....	32
3.2 Radiative Transfer Models	33
3.2.1 Clear Sky Radiative Transfer.....	33
3.2.2 Absorption coefficients for gas and liquid water	33
3.2.3 Successive Order of Interaction radiative transfer model	34
3.3 Reanalysis Data Products	34
3.3.1 ERA-Interim Reanalysis.....	35
3.3.2 HYSPLIT and the NCAR/NCEP 40- year reanalysis project.....	35
3.3.3 Climate Indices	36
Chapter 4	39
4 Microwave signatures of ice hydrometeors above Summit, Greenland	39
4.1 Introduction	39
4.2 Enhanced ice signature	40
4.3 Merged Data	42
4.4 Ice hydrometeor behavior as observed by ICECAPS	42
4.4.1 Characterization of ice precipitation at Summit.....	43
4.4.2 Enhanced brightness temperatures in the high frequency channels.....	46

4.4.3	Depressed brightness temperatures at 31.40 GHz	47
4.5	Liquid water path retrieval influenced by ice	48
4.5.1	Ice signature influence on retrieved liquid water	48
4.5.2	Ice influenced liquid water path correction.....	50
4.6	Observed Brightness temperature differences from ice.....	52
4.6.1	Brightness temperature differences with corrected LWP and PWV	53
4.6.2	Brightness temperature differences at 225 GHz.....	53
4.6.3	Multi-frequency comparison of brightness temperatures differences.....	54
4.6.4	Comparison of ice signatures observed with scattering model results.....	55
4.6.5	Future work on the LWP and PWV estimate in the presence of ice.....	57
4.7	Summary	58
Chapter 5	68
5	Microwave Radiometer Snow Regime Classification Tool	68
5.1	Introduction	68
5.2	Spectral Response from LF and HF “window” channels	70
5.2.1	MWR LF and HF response to clear-sky, CLW, and ice	70
5.3	Application of classification tool to ICECAPS dataset.....	71
5.4	Summary	74
Chapter 6	78
6	Snow regimes inferred from 5 years of ICECAPS observations	78
6.1	Introduction	78
6.2	Characterization of snow types as observed by ICECAPS	79
6.2.1	Occurrence and Accumulation Statistics	79
6.2.2	Relationship of PWV to snowfall types	81
6.2.3	Radar and ice particle observations	82
6.3	Source air mass characteristics and dynamics associated with snow types.....	86
6.3.1	Surface winds at Summit.....	86
6.3.2	Regional meteorological conditions for snow type	88
6.3.3	Back-trajectories for each snow type	92
6.4	Summary	93
Chapter 7	107
7	Precipitation regimes, climate indices, and storm tracks	107
7.1	Introduction	107
7.1.1	Event selection and methods.....	108
7.2	Climate index results.....	109
7.3	Sea level pressure and geopotential height anomaly results	112
7.4	Discussion	114
7.5	Summary	117
Chapter 8	126
8	Conclusions	126
8.1	Future work and applications.....	127
Appendix A: Acronyms	132
Bibliography	134

List of Figures

Figure 2.1 Figure showing the surface height of Greenland was created using measurements taken during the IceBridge campaign (Morlighem et al., 2015). The surface height combines the contributions from both the bedrock and ice sheet topography. Data were collected between January and December 2007. Spatial resolution is 150 by 150 meters.....	19
Figure 2.2 The left panel shows the complex terrain and major ridge features of the GIS, which influence the accumulation (Figure 5, Ohmura and Reeh, 1991). The right panel shows the annual accumulation in mm liquid water equivalent for Greenland (Figure 6, Ohmura and Reeh, 1991).....	20
Figure 2.3 Example of an Arctic mixed phase cloud as observed by the cloud radar throughout the entire day on September 1, 2017 at Summit Station (top panel). Example of a deep ice cloud system as observed by the cloud radar on September 27, 2017 beginning at ~1200UTC at Summit Station (bottom panel). Figures from the Summit Data Browser (https://www.esrl.noaa.gov/psd/arctic/observatories/summit/browser/).....	21
Figure 2.4 A schematic illustrating the primary processes and basic physical structure of Arctic mixed-phase clouds (Fig. 3 in Morrison et al., 2012).....	22
Figure 2.5 SLP maps for examples of NAO positive phase (left) and NAO negative phase (right; Compo et al., 2011; Figure from NOAA ESRL: https://www.esrl.noaa.gov/psd/data/20thC_Rean/timeseries/monthly/NAO/).....	23
Figure 2.6 Map showing the Greenland Blocking Index region (60N to 80N and 80W to 20W; Figure 1 from Hanna et al., 2016).....	24
Figure 2.7 Schematic diagram showing the primary (solid lines) and secondary (dashed lines) cyclone tracks around Greenland. Dots de- note discontinuity influenced by orography. Track B is a major storm track into Baffin Bay and Track C is a southern tip cyclone. Both of these tracks are linked to increased precipitation over the GIS (Figure 8 in Chen et al., 1997).	25
Figure 2.8 Sea level pressure anomaly patterns in the region around Greenland (contour lines, solid positive and dashed negative) and the associated precipitation anomalies (shaded contours, blue positive and red negative). The letters stand for W, weak; LC, Labrador cyclone; BB, Baffin Bay cyclone; ST, Southern Tip cyclone; NA, North Atlantic cyclone; IL, Icelandic Low cyclone (Figure 6 from Schuenemann et al., 2009).....	26
Figure 3.1 The ICECAPS Suite location at Summit Station, Greenland (left) and instrument suite (right). Instruments used in this study are highlighted with yellow outline (modified from Figure 1 in Shupe et al., 2013).	38
Figure 4.1 2DHs of MMCR reflectivity for summer (JJA) at Summit, Greenland from June 2010 through August 2013 with a sample resolution rate every 10 seconds. Panel a) shows JJA reflectivity for all measured LWPs while panel b) is filtered to reflectivities only when LWP is less than 40 g m^{-2} and panel c) is filtered for cases greater than 40 g m^{-2} . Additional 2DHs of MMCR Doppler velocity and spectral width for summer at Summit, Greenland for all LWPs (panels d and g), when LWP is less than 40 g m^{-2} (panels e and h), and when LWP is greater than 40 g m^{-2} (panels f and i), respectively. LWP less than 40 g m^{-2} accounted for ~63% of cases, while	

- greater than 40 g m^{-2} is 22% of cases, and the remaining 15% is clear sky (as determined by the MMCR).60
- Figure 4.2 2DHs of MMCR reflectivity for summer (JJA) at Summit, Greenland from June 2010 through August 2013 with a sample resolution rate every 10 seconds. Panel a shows JJA reflectivity for all measured LWPs while panels b and c show the fraction of the total 2DH counts that occur below and above the 40 g m^{-2} LWP threshold, respectively. The filtered cases are shown in percentage of total counts to highlight the differences in the characteristics of the low and high LWP cases. Panels d, e, and f show the MMCR Doppler velocity 2DH, and the count fractions below and above the LWP threshold. And finally, panels g, h, and i show the MMCR spectral width 2DH and count fractions. LWP less than 40 g m^{-2} accounted for ~63% of cases, while greater than 40 g m^{-2} is 22% of cases, and the remaining 15% is clear sky (as determined by the MMCR).61
- Figure 4.3 Brightness temperature differences between observations minus the modeled gas and liquid contributions in the 23.84, 31.40, 90, and 150 GHz channels as a function of Z_{PATH} for LWP less than 40 g m^{-2} . The count histogram is binned logarithmically in Z_{PATH} and linearly in ΔT_b , shown as percentage of total observation count per bin. The 150 GHz channel shows an enhanced BT difference with respect to Z_{PATH} (panel d), while the 90 GHz has a slight enhanced BT, the 31 GHz exhibits a negative dependence, and the 23.84 GHz is channel neutral.62
- Figure 4.4 Panel a shows the simulated downwelling microwave radiance spectrum with no ice (black) and the simulated spectrum with the biased PWV and LWP obtained by the retrieval (cyan). Panel b shows the simulated data after subtracting the simulated spectrum with no ice. The effect of the biased LWP and PWV on the microwave spectrum are shown independently (blue and green lines, respectively) and combined (cyan line). The “X” marks show the simulated ice influence at 23.84, 31.40, and 90 GHz.63
- Figure 4.5 Histograms of the MMCR Z_{PATH} and the difference between the measured and modeled BT at 23.84 and 31.40 GHz before and after the linear correction are shown above. Contour levels are linearly spaced, showing counts per factor of 100.05 in Z_{PATH} and per 0.05 K in BT difference. The y-axis is truncated to $6 \times 10^4 \text{ mm}^6 \text{ m}^{-2}$ Z_{PATH} to highlight the correction in the low ice optical depth cases. Red signifies 50 and higher counts and blue signifies fewer than 5 counts. Plots are linear in both axes. The uncorrected 31.40 GHz channel (panels c) has a negative bias as a function of the Z_{PATH} . The slope of the uncorrected 31.40 GHz (panel c) histogram yields the value of $\Delta T_b / \Delta Z_{\text{PATH}}$ used in the linear correction. For both low frequency channels, once the correction is applied, no dependence on Z_{PATH} is present (panels b and d). .64
- Figure 4.6 Brightness temperature differences between the HFMWR and the HFMWR-225 observations and the modeled gas and liquid contributions after implementing the LWP correction for ice for the 90, 150, and 225 GHz channels. The count histogram is binned logarithmically in Z_{PATH} and linearly in ΔT_b , shown as percentage of total observation count per bin (same as Figure 4.3). The high frequency channels show a dependence of the difference in brightness temperature and the Z_{PATH} from the MMCR – thus, indicating an increasing brightness temperature in these channels with increasing total ice amount in the column. Additionally, the sensitivity to the ice signature increases as a function of higher frequency. The Z_{PATH} value where the ice

- signature BT enhancement begins is lower in the 150 versus the 90 GHz channel (panels b and c, respectively) and lowest in the 225 GHz (panel c). We note that there is a clear sky bias in all three channels, but the magnitude of this bias is smaller than the radiometric uncertainty of the HFMWR observations. We are unable at this time to determine if this bias is due to calibration uncertainty in the radiometer or the result of forward model error.65
- Figure 4.7 Multi-frequency plots of the BT difference in channels 23.84, 31.40, 150, and 225 GHz as compared to the 90 GHz channel. The binned values of BT difference are colored according to logarithm of the average Z_{PATH} values. In the top two panels, the lower frequency channels are plotted against 90 GHz (a and b) and in the bottom two panels, the 150 and 225 GHz are plotted against the 90 GHz (c and d).66
- Figure 4.8 SOI simulated BT differences plotted on top of the observations for the 150 versus 90 GHz and 225 versus 90 GHz channels (panel a and b, respectively). In both examples, the slopes of the simulations agree well with the observations.67
- Figure 5.1 A representation of modeled extinction optical depth as a function of frequency for the atmospheric components under conditions relevant for Summit: both the liquid water path and ice water path are 40 g m^{-2} , and the WV and dry gas concentrations are from the Standard Subarctic Winter profile starting at 3 km. The red and blue arrows highlight the microwave channel observations used in the study (low and high frequencies, respectively). Note the different spectral slopes of the ice versus the liquid versus the WV contribution.75
- Figure 5.2 A schematic representation of the spectral response of the low (red) and high (blue) frequency microwave radiometers under conditions of clear sky (left), cloud liquid water in the column (middle), and precipitating ice cloud (right). Error bars denoting the MWR channel measurement precision is shown in the top left corner of each plot (0.3 K and 1.0 K for the low and high frequency channels, respectively). ..76
- Figure 5.3 All available MWR data for 2010 – 2015 during precipitation (as determined by the POSS Ppu threshold). These values are delta BT where the clear sky forward model RT run is subtracted from the MWR observations. The arrow annotations show the regions of IC snow (to the left of the dashed line), snow with associated CLW in the column (to the right of the dashed line), and snow of indeterminate type (in the cyan outlined region). The indeterminate region is defined by the sample distribution in clear sky, and captures the residual variance due to uncertainties in the modeling of the gas absorption optical depth.77
- Figure 6.1 These are the MWR observations minus the clear-sky contribution, for all available data during precipitation events from 2010 to 2015. The summer precipitation is show in Panel a (left; summer is defined as May through September), and the winter precipitation is shown in Panel b (right; winter is defined as October through April). The summer MWR observations indicate both IC and CLW snow events occur through the season, though more CLW events. The winter season tends to strongly favor the IC snow events.97
- Figure 6.2 The POSS statistics from 2010 – 2015 for the MWR filtered precipitation events. Panel a (top) shows snow amounts by Occurrence (POSS) for all data: IC – 30.5 %, CLW – 48.5 %, and Indeterminate – 21 %. Panel b (bottom) shows snow amounts by Accumulation (POSS) for all data: IC – 35 %, CLW – 51 %, and Indeterminate – 14 %. The POSS snowfall amounts and snow rates were calculated

- using the Joe and Sheppard (2008) Z to S relationship. (Note: Panel c shows very high values for the CLW snow in May, which is due to an unusually large storm dominating the results).98
- Figure 6.3 Panel a shows the average annual PWV as a function of the month for MWR data from 2010 –2015. The PWV values during snowfall events, regardless of type, are higher than that of the PWV averages during all times (precipitation and non-precipitating). Panel b shows the average PWV associated with each MWR-determined type of snowfall. Panel c shows the ratio of the average snow rate measured by the POSS in LWE mm hr^{-1} to the associated PWV in mm, thus giving a rate of how efficiently the PWV converts to precipitation for each month and snow type.99
- Figure 6.4 Composite two-dimensional histograms of MMCR properties for each MWR-determined snow type are shown. Each histogram uses a linear color scale with a maximum value of 80,000 counts. Panels a (top, left) and b (top, right) show the MMCR reflectivity as a function of height for all the IC and CLW snow cases, respectively. Panels c (bottom, left) and d (bottom, right) show the MMCR Doppler velocities as a function of height. These composites of the IC and CLW precipitation highlight different characteristics between the two snow modes. 100
- Figure 6.5 Values of MMCR calculated snow rate, Z_{PATH} , and cloud thickness are calculated for all the precipitation events and plotted with the associated HF and LF MWR observations. The top Panels (a, b, and c) depict these characteristics for the summer months and the bottom Panels (d, e, and f) for the winter months. Regardless of season, the IC precipitation has a higher instantaneous snow rate than the CLW cases. Additionally, the Z_{PATH} values for the IC snow cases are much higher than the CLW cases. And the IC snow tends to be associated with deeper clouds than the CLW snow. 101
- Figure 6.6 Examples images from the IcePIC camera of ice cloud (IC) originating snow events (left) and for mixed-phase CLW containing snow events (right). 102
- Figure 6.7 Surface winds from the Summit NOAA meteorological data are shown. For reference, Panel a shows all surface winds from 2010 –2015 for all times. Panel b (middle) shows the surface winds for the MWR-determined IC snow cases. These winds tend to come out of the southeast with little variability and are much stronger than the average winds. Panel c (right) shows the surface winds for the MWR-determined CLW containing snow cases. Associated winds tend to be from the west to south with a maximum amount from the southwest direction. Though the CLW snow cases have stronger winds than average, they are not as strong as the winds associated with the IC snow. 103
- Figure 6.8 Panel a (top, left) shows the ERA-Interim derived average SLP and 10 meter winds for 90 IC snow events. Panel b (top, right) shows the same, but for 84 CLW snow events. Both plots are on the same scale. Panels c and d show the anomalies for the SLP and 10 meter winds for the respective cases. The persistent low pressure and strong 10-meter winds are evident for the IC snow cases. In the cases for the CLW snow, there are relatively calm winds and uniform mean SLPs. Both the cyclone and anti-cyclone structure features in the IC snow cases are quite anomalous, whereas the broad high-pressure field in the CLW cases is weakly anomalous. 104

- Figure 6.9 Panel a (top, left) shows the ERA-Interim derived average 500mb geopotential heights and winds for 90 IC snow events. Panel b (top, right) shows the same, but for 84 CLW snow events. Both plots are on the same scale. Panels c and d show the anomalies for the 500mb heights and winds for the respective cases. There is an incredibly strong trough and ridge feature in the IC snow cases. This feature indicates diverging upper-level winds just to the east of the trough, over the SE Greenland coast, which would induce strong vertical motions in the column and the upper level winds up show strong SE flow over the GIS. The CLW cases depict relatively calm and flat features, indicating quiescent flow of air up over the GIS from the S and SW. 105
- Figure 6.10 Panel a (top, left) shows the HYSPLIT calculated, 36 hour backtrajectories for the air at 3 km AGL originating at Summit using GFS for the IC snow cases. The backtrajectory AGL values represent the altitude above ground along each trajectory path. Panel b (top, right) shows the same, but for the CLW cases. The bottom two Panels (c and d), show the mean vertical motions (dark line) and standard deviation (lighter fill) for the IC and CLW cases, respectively. These are consistent with the previous figures: the IC snow cases being vertically lifted and advected over the GIS from the SE. While the CLW cases come from the S and SW along the mean flow. 106
- Figure 7.1 NAO index for all times (1950 – 2017), black solid line, and NAO index for ICECAPS time frame (2010 – 2017), black dashed line. These are shown in fraction of counts. The middle black is a histogram of IC snow events (98) and the bottom blue is a histogram of CLW snow events (82). The mean and standard deviation of the NAO index for the IC events are -0.05 ± 0.77 and for the CLW events are -0.51 ± 0.73 120
- Figure 7.2 Annual cycle of GBI values shown in height versus the day of the year. Each blue point is a value for the days from 1948 – 2015. There is a large dependence on the height as a function of the season. For example, the January mean GBI height is ~5100 meters, while in July it is ~5500 meters. There is the largest variance of values in the northern hemisphere winter months. The IC events are plotted in black stars and the CLW events are plotted in blue circles. 121
- Figure 7.3 The left panels show the GBI heights for all times (1948 – 2015), black solid line, and GBI heights for ICECAPS time frame (2010 – 2015), black dashed line, shown in fraction of counts (top). The left, middle panel in black is a histogram of IC snow events (65) and the left, bottom panel in blue is a histogram of CLW snow events (72). The right top panel in green is the ICECAPS time range GBI anomalies (versus the days from 1948 – 2015). The right, middle panel is the histogram of the GBI anomalies compared to the 1948 – 2015 time period for the IC events (black). The right, bottom panel is the histogram of the GBI anomalies compared to the 1948 – 2015 time period for the CLW events (blue). 122
- Figure 7.4 Scatter plots for the mean snow rate values and the various indices: NAO (top), GBI height (middle), GBI anomaly (bottom). The IC events are depicted with black stars and the CLW events are depicted with blue circles. 123
- Figure 7.5 The SLP and 10 meter wind anomalies for the IC snow cases (top) and the CLW snow cases (bottom). The left panels show the SLP and 10 meter wind anomalies for all IC cases (top) and CLW cases (bottom). The middle panels show

the SLP and 10 meter wind anomalies for the JJA events for each snow type (IC, top; CLW, bottom). The right panels show the SLP and 10 meter wind anomalies for the SON events for each snow type (IC, top; CLW, bottom).	124
Figure 7.6 The 500 mb GPH and wind anomalies for the IC snow cases (top) and the CLW snow cases (bottom). The left panels show the 500 mb GPH and wind anomalies for all IC cases (top) and CLW cases (bottom). The middle panels show the 500 mb GPH and wind anomalies for the JJA events for each snow type (IC, top; CLW, bottom). The right panels show the 500 mb GPH and wind anomalies for the SON events for each snow type (IC, top; CLW, bottom). The yellow dashed lines outline the area used for averaging the 500 mb GPH heights to calculate the single GBI value.	125

List of Tables

Table 3.1 Subset of ICECAPS instruments used in this study (modified from Table 1 in Shupe et al., 2013).....	37
Table 7.1 The IC and CLW snow events as a percentage of occurrence for each season.	119

Chapter 1

1 Introduction – Arctic response to climate change

The recent warming of the Earth's atmosphere is well documented and amplification of this warmth in the high latitudes is causing rapid regional changes (Serreze et al. 2007; IPCC – Fifth Assessment Report, 2013). This warming already directly affects the state of the cryosphere, which in turn further modifies the large-scale dynamics of the atmosphere in the Polar Regions (Francis and Hunter, 2006; Kay et al., 2008; Stroeve et al., 2012). Sea level rise (SLR) resulting from the melting of the Antarctic and Greenland ice sheets has potential for devastating humanitarian and socio-economic impacts (Alley et al., 2005; Rignot et al., 2011; IPCC – Fifth Assessment Report, 2013). Much of the global population lives along coastlines and will experience increased flooding due to storm surges and high tides, as well as damage to infrastructure and land through salt/other contamination from higher sea levels (Nicholls and Cazenave, 2010).

SLR from the melting of the Greenland Ice Sheet (GIS) is of particular concern with warming temperatures and changing climate conditions for several reasons: primarily, model studies have indicated that presently loss of ice from the GIS is accelerating and that the GIS will lose most of its mass under current climate change predictions (van den Broeke et al., 2009; Rignot et al., 2011). The GIS contains 10 % of the world's freshwater and would contribute a destructive ~7.4 m SLR if fully melted (Church, 2001). Secondly, the injection of large amounts of fresh water into the North Atlantic could attenuate the Atlantic meridional overturning circulation, (AMOC) possibly

leading to widespread cooling in the mid-latitudes, especially in Europe (Alley et al., 2005). Finally, the warming atmosphere that is driving much of the change in the Arctic will be further modified by the changes manifesting in the cryosphere (Kay et al., 2008; Stroeve et al., 2012). The resulting feedback mechanism of the interactions between the cryosphere and atmosphere with a changing climate creates greater uncertainty for predicting future possible scenarios (Stroeve et al., 2012).

The mechanisms behind the loss and gain of mass on the GIS are inextricably linked to the atmosphere – specifically thermodynamic processes and cloud properties (Lemke et al., 2007). To understand the current state of and future changes to the GIS, we need precise observations of the clouds, precipitation, and thermodynamic characteristics of the atmosphere, in addition to direct measurements of the cryosphere. Observations of the atmosphere in the Arctic and over the GIS are obtained through networks of ground-based, remotely-sensed and in-situ measurements, satellite instrumentation, and airborne campaigns (for example, Shuman et al., 1996; Rignot et al., 2011; Morlighem et al., 2015; McMillan et al., 2016; Uttal et al., 2016; Van Tricht et al., 2016). These observations aid in enhancing our understanding of the cloud processes and atmospheric drivers, providing constraints that increase the ability of models to more accurately predict future climate conditions (Kay et al., 2016; McIlhatten et al., 2017).

The already difficult task of forecasting the impacts of a warming atmosphere on the GIS is further complicated by the apparent nonlinear response of the snowfall (Alley et al., 1993; Kapsner et al., 1995; Hanna et al., 2008). Studies of ice core records indicate that changes in atmospheric dynamics, not temperature, are the main drivers of mass changes in the central GIS (Kapsner et al., 1995; Appenzeller et al., 1998; Hanna et al.,

2016). Studies of cyclone storm tracks and intensities under climate change scenarios have indicated an increase of precipitation over the GIS (Rogers et al., 2004; Schuenemann and Cassano, 2010; Serreze and Barry, 2014). Schuenemann and Cassano (2010) found that a northern shift of the North Atlantic storm track could increase precipitation over Greenland ~28 % by 2100 with an associated 0.5 mm yr^{-1} decrease in SLR. Currently, mass loss from the GIS due to melting at the coastlines and edges is only slightly outpacing the snow accumulation at the center (Hanna et al., 2006; Hanna et al., 2013), however, models predict that once the average warming reaches $+3^\circ \text{ C}$ over Greenland, the surface melting will eclipse the rate of snowfall gained over the central GIS (Gregory et al., 2004). Improved characterization of precipitation in the Arctic is a fundamental part of forecasting how climate change will impact the hydrological cycle and mass balance of the GIS.

Chapter 2

2 Greenland Ice Sheet mass balance

To understand how the GIS will respond to a changing climate we must have a complete understanding of the factors that influence the mass balance. Examining the patterns of ice sheet mass loss and gain in past climate conditions can aid in forecasting possible future scenarios. Ice cores from the center of ice sheets are excellent proxy data for obtaining information about accumulation of snow and ice patterns during past climates (Alley et al., 1993; Grootes et al., 1997; Alley et al., 1997) and patterns of mass gain and loss information for the central GIS are obtained through analysis and modeling of these ice cores (Kapsner et al., 1995; Appenzeller et al., 1998). Connecting the ice, firn, and snow on the GIS to the atmosphere is crucial to understanding how the precipitation reaches central Greenland. Ground-based, airborne, and spaceborne remote sensing and in-situ measurements of the atmosphere above the GIS can help illuminate the cloud processes and characteristics associated with precipitation (Uttal et al., 2016; Van Tricht et al., 2016). Additionally, reanalysis products can show the regional meteorological conditions and dynamics that force water vapor rich air masses up and over the GIS (Kalnay et al., 1996; Dee et al., 2011).

2.1 Historical data and recent trends

Historical records of temperature are inferred through the oxygen isotope composition of ice (Grootes et al., 1997) and accumulation statistics are obtained through visual measurements of the ice core annual structure produced by summertime insolation

(Alley et al., 1993). Melt events across the GIS can also be tracked with visual inspection of the layer of the ice core (Meese et al., 1994). The Greenland Ice Sheet Project II (GISP-2; Dansgaard et al., 1993; Alley et al., 1997) ice core, completed in 1997, yields relevant information about the relationship between temperature and precipitation during the Holocene (warm) and the Younger Dryas (Last Glacial Maximum) climate regimes (Bromwich et al., 1993; Kapsner et al. 1995).

Clausius-Clapeyron predicts that with every 1 degree C increase in temperature, there is a corresponding increase of about 7 % in the available precipitable water vapor (PWV), however only a 2 % globally averaged increase in precipitation accumulation (Held and Soden, 2006). However, studies of the GISP-2 ice core find that temperature and accumulation correlate weakly or not at all during periods of climate stability (for example, times between ice age transitions). During these relatively stable periods accumulation changes ~1 % change per °C (Reeh, et al., 1978; Kapsner et al., 1995). Ice core analyses of the GIS find that individual storm track locations and intensities are the dominant mechanism for the increases in accumulation over the central GIS and not temperature (Kapsner et al., 1995; Bromwich et al., 1993) and that large changes in accumulations are correlated with shifting climate states (Alley et al., 1993; Taylor et al., 1993).

Though GIS accumulation and temperature are not linearly correlated, there is a strong correlation between increased atmospheric temperature from greenhouse gases and SLR due mainly to substantial losses in ice sheet volume (Huybrechts et al., 1991). Currently, loss of mass is observed throughout Greenland, but is most extreme at the edges of the GIS (Hanna et al., 2013). These rapid changes at the ice margins are mainly due to

surface melt water percolation accelerating the melting at the bottom of the ice flows and ocean warming and erosion of the calving faces of glaciers (Zwally et al., 2002; Hanna et al., 2013). The loss of mass from the GIS to the ocean is highly correlated to increased sea surface temperatures and loss of Arctic sea ice (Gregory et al., 2004; Hanna et al., 2013). In general, modeling studies show that as the climate warms there will be a northward shift in cyclone locations and this is connected to a forecasted increase in precipitation over the GIS (IPCC 4th assessment; Alley et al., 2007; Schuenemann and Cassano, 2010).

While historical data is useful for understanding mass gain and loss over the GIS during past climate regimes and to fine-tune model output, it does not necessarily help models tackle the non-linear climate change scenarios projected by the IPCC (Lemke et al., 2007). This unpredictability is due in part to the occurrence of climatologically extreme events, such as unusual warmth, and their yet unknown consequences on the GIS. Such events can have large impacts on the gain and loss of mass over the GIS and are complicated to model and predict (Abdalati and Steffen, 1997; Hanna et al., 2008; Ngheim et al., 2012; Bennartz et al., 2013).

2.1.1 Extreme events

Recent studies of extreme events have helped to inform models and our understanding of the long-term mass balance of the GIS. Hanna et al. (2006), found that individual, strong storms lead to disproportionate accumulations on the central GIS, nearly doubling the average annual amount for some regions of the GIS. The 1991 eruption of Pinatubo resulted in a -2 C surface temperature anomaly observed by ground-based instrumentation on the GIS (Shuman et al., 1996) and resulted in a temporary reversal of the satellite observed trend in the mean melt extent of the GIS (Abdalati and Steffen,

1997). Warmer springtime temperatures in the Arctic have caused earlier melt in surface snow and ice and leading to exposed areas of bare ice on the margins of the GIS, which has a lower albedo and therefore leads to accelerated regional melt during the summer (Tedesco et al., 2011). Current airborne and satellite observations overwhelmingly show that the GIS is losing mass at a unprecedented rate, $269 \pm 51 \text{ Gt yr}^{-1}$ between January 2011 and December 2014 (McMillan et al., 2016), with increasing melt trends throughout Greenland in recent years when compared to historical averages (Mote, 2007; Kintisch, 2017).

On July 12, 2012 the GIS experienced a melt event over almost the entire surface for the first time since 1889 (Nghiem et al., 2012). This extreme event was an excellent opportunity to better understand both the dynamical mechanisms of the atmosphere as well as the role clouds play in promoting melt extent over the ice sheet. An anomalous ridge of warm air was advected up over the GIS where it remained for several days and satellite observations measured the extent and duration of the surface melt (Nghiem et al., 2012). In addition to the warm air advection, water vapor and supercooled cloud liquid water were present over much of the central GIS (Neff et al., 2014). Optically thin supercooled liquid water clouds augmented the surface warmth enough to raise temperatures above freezing in high-altitude locations that would otherwise not have experienced surface melt under clear-sky conditions (Bennartz et al., 2013).

Extreme events in the Arctic highlight two things: first, these events are non-linear in their response to rising global temperatures and therefore it is difficult to predict their effect on the GIS from models. And second, observations from satellites and ground-based instruments aid in illustrating the regional cloud and atmospheric processes contributing to

these anomalous events. Using the ice core proxy data is helpful in informing parameters for models, but limited in ability as current changes may lead to climate states that do not resemble the historical record. Ground-based remote sensed and in-situ instrumentation can elucidate in detail how changes in climate are manifesting at discrete points on the GIS. These observations, when incorporated into reanalysis products can provide a regional perspective and when incorporated into global models may improve our understanding of how climate change will affect the GIS.

2.2 Precipitation over the central GIS

Snowfall on the interior of the GIS is a small net positive mass balance, but it is not well constrained (Thomas et al., 2000). Summit Station is located in the central GIS and was the site of the Greenland Ice Sheet Project 2 ice core project (GISP2; Dansgaard et al., 1993) and continues to operate as a year-round research facility focused on atmospheric processes and the cryosphere. Where precipitating clouds originate and the mechanisms that result in precipitation over Summit Station are largely unknown (Shupe et al., 2013). Improved characterization of precipitation and associated atmospheric processes in the Arctic is fundamental to enhance our understanding of present and future manifestations of the hydrological cycle and mass balance of the GIS. Accurate atmospheric measurements and remote sensing precipitation retrievals from multiple instruments are essential to resolving and refining precipitation estimates over the GIS.

As seen in Fig. 2.1, the topography of Greenland itself is a hindrance in precipitation occurrence and accumulation atop the high plateau of the GIS: much of the central GIS is higher than 2000 meters above sea level, with a summit of 3,216 meters, far from the ocean and water vapor (WV) sources (400 km from the east and west coastlines; 1000 km

from the southern coasts; IceBridge data; Morlighem et al., 2015). The Greenland topography with highlighted major ridge features are illustrated in Fig. 2.2, left panel, and the accumulation patterns are shown in panel b (Ohmura and Reeh, 1991). Due to the complex nature of the terrain, understanding the large-scale regional dynamics that advect relatively warm, WV-rich air masses atop the GIS is key to predicting how precipitation is deposited. Measuring attributes of the clouds and thermodynamic profiles specifically associated with snow events over the GIS is similarly important.

2.2.1 Arctic Cloud Phase

Much of this study examines Arctic clouds divided into two classifications: fully-glaciated clouds, which contain only ice hydrometeors, and mixed phase clouds, which contain both ice and supercooled liquid water hydrometeors. Both of these cloud types have been extensively studied in the Arctic as the phase partitioning of the cloud and precipitation has implications for both the mass and energy balance at the surface of the GIS: through surface processes and feedbacks and their impact on down and upwelling radiative fluxes (Miller et al., 2015; Van Tricht et al., 2016; McIlhatten et al., 2017).

Arctic mixed phase (AMP) clouds are comprised of both ice crystals and cloud liquid water (CLW) and have been studied through numerous ground and airborne instrument field campaigns (Curry et al., 2000; Intrieri et al., 2002; Verlinde et al., 2007; Shupe et al., 2008; Shupe et al., 2013). Figure 2.3, top panel, shows ground-based cloud radar observations of a typical AMP cloud at Summit Station. Characteristically, AMP clouds are $\sim 1 - 3$ km thick and have a layer of supercooled CLW droplets at the top of the cloud with ice crystals falling through the cloud below the CLW layer (see Fig. 2.4; Hobbs and Rangno, 1998; Curry et al., 2000; Shupe et al., 2005; Shupe et al., 2008; Morrison et

al., 2012). The supercooled CLW droplets radiatively cool to space, which has been shown to induce small-scale turbulent motions that maintain the CLW layer characteristic of AMP clouds (Rauber and Tokay, 1991; Shupe et al., 2011), in turn, this motion entrains water vapor from above the cloud and sustains the CLW layer while water leaves the cloud system in the form of ice falling below (illustrated in Fig. 2.4; Curry et al., 2000; Solomon et al., 2011; Morrison et al., 2012). Observations have shown that AMP clouds are particularly long-lived, persisting up to days (Curry et al., 2000; Shupe et al., 2006; Morrison et al., 2012; Shupe et al., 2013) and occur commonly in high latitude regions (deBoer et al., 2009; Shupe et al., 2011). Additionally, AMP clouds can persist under weakly forced conditions and do not require synoptic forcing from frontal systems to occur or propagate (Morrison et al., 2012). AMP clouds have been shown to create light to moderate precipitation over the ice sheet (Verlinde et al., 2007; Shupe et al., 2008). Though the precipitation associated with AMP clouds is generally light, they are abundant and long-lived in the Arctic, and can therefore contribute substantial amount of the accumulation over the central GIS (Shupe et al., 2008).

Similar to AMP clouds, fully-glaciated ice clouds have been extensively studied in the Arctic through ground-based and airborne in-situ and remote-sensed instrumentation (Intrieri and Shupe, 2004; Curry et al., 2000; Lawson et al., 2001; Lawson et al., 2006; Schiller et al., 2008; Shupe et al., 2013). Ice clouds can produce virga, where the ice hydrometeor evaporates before reaching the ground, or diamond dust, a cloudless ice crystal precipitation (Intrieri and Shupe, 2004). Additionally, ice clouds above an AMP cloud, can act as a source of moisture for the supercooled layers below (Curry et al., 2000). Ice clouds can remain single phase throughout the column and precipitate ice crystals from

cloud top all the way to the ground (Shupe et al., 2013). Figure 2.3, bottom panel, shows cloud radar observations of a deep ice phase cloud at Summit Station. Arctic ice clouds tend to be much deeper than AMP clouds, extending up to 4 – 7 km above ground level (Curry et al., 2000; Lawson et al., 2006; Shupe et al., 2013). Cloud radar studies of ice clouds find they have a characteristic uneven structure at the top of the cloud with fall streak features extending from the top of the cloud to ground (Matrosov et al., 2001; Shupe et al., 2013). The cloud radar studies also show narrow reflectivity spectra throughout the column and increasing Doppler velocities closer to the ground, indicating that there is little turbulence within the cloud and that the ice hydrometers are growing as they descend (Curry et al., 2000; Shupe et al., 2013). Several in-situ studies of Arctic ice clouds have yielded information about ice habits, in particular, that they are made up of a combination of pristine and irregular ice crystals (Korolev et al., 1999; Lawson et al., 2001; Lawson et al., 2006). These deep ice clouds are associated with the passage of frontal systems at Arctic observing locations (Curry et al., 2000; Verlinde et al., 2013; Oue et al., 2015).

2.2.2 Precipitation relationship to climate indexes and storm systems

Studies have illustrated relationships between precipitation over the central GIS and various climate indexes as well as certain storm tracks (Kapsner et al., 1995). The impacts on precipitation over Greenland from phases of the North Atlantic Oscillation (NAO), the Greenland Blocking Index (GBI), and, to a lesser extent, the Arctic Oscillation (AO) have been examined (Appenzeller et al., 1998; Bromwich et al., 1999; Hutterli et al., 2005; Hanna et al., 2016). Studies of the locations and strengths of individual storm tracks around Greenland have also shown connections to positive precipitation anomalies over

the GIS (Chen et al., 1997; Schuenemann and Cassano, 2009; Schuenemann et al., 2009; Schuenemann and Cassano, 2010).

The NAO index is defined by the atmospheric sea level pressure (SLP) difference and positions of the Azores High and the Icelandic Low (Fig. 2.5; Compo et al., 2011). Early findings show that NAO positive (negative) phase is connected to drying (precipitation) over the GIS (Hurrell, 1995). Appenzeller et al. (1998), used ice core proxy data to show that precipitation accumulation in Western Greenland is historically been correlated to the negative phase of the NAO. Bromwich et al. (1999), examined years of reanalysis products to study the precipitation patterns over Greenland and found that accumulation was higher in during months with weakening of the Icelandic low (negative NAO phase). Hutterli et al. (2005) and Mosely-Thompson et al. (2005) found evidence that the accumulation variability in western part of the GIS is influenced by a negative NAO-like pattern. More recent studies indicate that the correlation of the NAO negative phase and precipitation over Greenland are weak and only for the western part of the GIS (Rogers et al., 2004; Schuenemann et al., 2009). Additionally, Mosely-Thompson et al. (2005), found that correlation between accumulation and NAO at Summit Station is very low and state that central Greenland ice cores should not be used in NAO reconstructions.

The GBI is defined as the average value of the 500 mb geopotential heights over the whole of Greenland (see Fig 2.6 for defined region; Fang, 2004; Hanna et al., 2016). High values of 500 mb geopotential heights over Greenland create a blocking feature (ridge), which affects the location of the upper-level winds and jet stream and modifies the precipitation and weather in the region and in the Northern Hemisphere (Hanna et al., 2013; Hanna et al., 2016). Hanna et al. (2016) found that precipitation anomalies over

most of Greenland are positive under high GBI values. During high GBI conditions, weak and WV-rich winds are advected from the south onto the GIS and have associated high precipitation accumulation anomalies (Hanna et al., 2016). However, this is contradictory to some of the studies that show precipitation in parts of Greenland corresponding to specific storm tracks and intensities (Schuenemann and Cassano, 2009; Schuenemann et al., 2009).

Direct connections between precipitation over the GIS and the AO have not been investigated, however the AO and NAO indices are highly correlated (Hurrell, 1995). There are studies of the AO and loss or gain of Arctic sea ice (Rigor et al., 2002) as well as connections between Arctic sea surface temperatures and AO (Thompson and Wallace, 1998). The AO can therefore influence the precipitation over the GIS indirectly through the loss of sea ice resulting in more open ocean surface (Rigor et al., 2002). Reduced sea ice cover and thickness enhances the warming in the Arctic and leads to an increase in available PWV near Greenland (Wang and Key, 2003; Francis and Hunter, 2006; Screen and Simmons, 2010).

Studies of low-pressure storms from the North Atlantic show that certain locations, storm tracks, and strengths create positive anomalies of precipitation over the GIS (Rogers et al., 2004; Schuenemann et al., 2009). In particular, Baffin Bay low-pressure systems and Greenland lee cyclogenesis are important for precipitation accumulation across the entire GIS (Chen et al., 1997; Bromwich et al., 1998; Rogers et al., 2004; Schuenemann et al., 2009). Additionally, lee cyclogenesis from the topographic ridge along the tip of Greenland is a common storm track and could act as a positive feedback mechanism, as more accumulation atop the southern GIS will further intensify these storms and resulting

in increased precipitation accumulation (Chen et al., 1997; Rogers et al., 2004; Schuenemann et al., 2009). It is important to distinguish the Greenland lee cyclones from those cyclones that move through the Icelandic Low, as the latter is less important to precipitation processes above the GIS and may actually reduce accumulation amounts (Chen et al., 1997; Rogers et al., 2004; Serreze and Barry, 2014). Schuenemann and Cassano (2009) and Schuenemann et al. (2009), used reanalysis products for 1961 – 1999 and demonstrated that the blocking, splitting, and intensifying of low-pressure systems by Greenland topography is key in increased precipitation over the GIS, which reinforces similar findings by Hutterli et al. (2005). Figure 2.7 illustrates the most common cyclone tracks around Greenland (Chen et al., 1997). Chen et al. (1997), found that storm tracks B and C in Fig. 2.7 lead to positive precipitation anomalies over the GIS; whereas storm track A is connected to the Icelandic Low and results in reduced precipitation over the GIS. Schuenemann et al. (2009), showed similar storm tracks result in positive precipitation anomalies in Greenland (see Fig. 2.8). Additionally, Schuenemann and Cassano (2010), used climate models to forecast that accumulation over the GIS would increase ~28 % by 2100 due to a northward shift of the North Atlantic storm tracks and increased available PWV.

2.2.3 Remote-sensing of cloud and precipitation processes

As mentioned previously, Summit Station was the site of the GISP2 ice core project in 1992, and has been expanded to a continuously operational science facility dedicated to studying the atmosphere and ice sheet properties of the GIS (Dansgaard et al., 1993). Summit Station is home to many atmospheric and snow science instruments, including Integrated Characterization of Energy, Clouds, Atmospheric State, and

Precipitation at Summit project (ICECAPS; Shupe et al., 2013). The ICECAPS project aims to facilitate a better understanding of the cloud and atmosphere properties over the GIS and their interaction with the cryosphere. Since 2010, the ICECAPS suite of instruments has been monitoring a variety of atmospheric parameters to further our knowledge of atmospheric processes above the GIS (Shupe et al., 2013). The ICECAPS project will remain at Summit until at least 2018. Additionally, ICECAPS is expanding the network of past and existing high-latitude atmospheric suites (i.e., Eureka, Canada and Barrow, Alaska, Ny-Alesund) already helping to characterize Arctic atmospheric and cloud processes (Shupe et al., 2011; Uttal et al., 2016).

Included in the ICECAPS instrument suite are microwave radiometers (MWRs), which are remote sensing instruments that make passive measurements of radiance at specific frequencies. Typically, MWR measurements are used to retrieve atmospheric and/or cloud properties, specifically temperature profiles, cloud liquid water path, and precipitable water vapor. A frequently implemented technique for characterizing ice hydrometers from satellites and aircraft is to use high-frequency microwave channels (89 GHz and greater) and look for depressed brightness temperatures (BT; Spencer et al., 1989). The depression in BT is due to the scattering of the upwelling radiation by the ice to and is often used to calculate an ice water path (Deter and Evans, 2000; Bennartz and Bauer, 2003; Hong et al., 2005; Kulie and Bennartz, 2009). While liquid and gas in the atmospheric column absorb and emit microwave radiation, ice hydrometeors scatter surface radiation away from the satellite sensor and depress the observed BT. The same technique can be used from the ground looking up with the opposite effect, as ice scatters the upwelling radiation back towards the MWR sensor (Kneifel et al., 2010). Observations

from the MWR are used to detect ice hydrometeors in the atmosphere and classify clouds and precipitation through the detection of the presence or absence of CLW.

MWR detection and classification of CLW and ice hydrometeors in clouds above Summit Station can be combined with measurements from other ICECAPS instrumentation. For example, utilizing measurements of reflectivity, mean Doppler velocity, and Doppler spectral width from co-located 35 GHz cloud radar for inferring cloud and precipitation information. Ceilometer data can be used for information on the cloud base height measurements. In-situ measurements of temperature, relative humidity, and pressure are obtained from balloon-borne radiosondes. Complementary precipitation detection and characteristics can be acquired from a surface-based X-band radar. A scientific technician records information about ice crystal habits during select snowfall events using a photographic method. Surface meteorological data (2 and 10 meter temperature, relative humidity, and winds) and trained observer information are obtained through the National Oceanic and Atmospheric Administration (NOAA) local observatory. These co-located instrument observations are used in concert with the MWR data to lend insight into the cloud characteristics and the associated atmospheric conditions coincident with precipitation events.

2.3 Objectives of this work

This work focuses on detection and analysis of precipitation at Summit Station primarily utilizing instrumentation from the ICECAPS project with adjunct analysis from models and reanalysis products. Throughout this work the following questions are addressed:

- How can ice hydrometeors best be identified, characterized, and classified using ICECAPS observations?
- What are the physical properties and characteristics of clouds associated with precipitation; are they deep or shallow; calm or turbulent?
- Does precipitation partition into discrete regimes that are tied to specific cloud characteristics and dynamics?
- What is the seasonality of the precipitation in both occurrence and accumulation?
- Where do precipitating clouds come from? It is difficult to advect WV-rich air masses over the GIS, so where do air masses that result in precipitation over the central GIS originate?
- What are the primary mechanisms for forcing precipitation observed at Summit Station; is precipitation tied to major climate oscillations, specific storm tracks, or both?

To address the above points, we present the following: Chapter 3 details the ICECAPS and NOAA instruments used in this study, merged datasets, reanalysis products, models, and methods used in this work. Chapter 4 focuses on the ice hydrometeor signature from several high frequency MWR channels for the 2010 – 2013 Summer seasons. Interpretation of the ice hydrometeor signature results, cloud characteristics, and affects on retrieval products are discussed in Chapter 4. Chapter 5 introduces a unique way of partitioning clouds and snowfall using the relationship between low and high frequency MWR window channels. This precipitation partitioning method yields distinct modes of snow regimes observed at Summit Station. Chapter 6 utilizes the novel MWR snow regime classification method to examine characteristics of the associated cloud

processes, using ICECAPS instrumentation and air mass source and dynamics, and surface meteorological measurements and reanalysis products. Chapter 7 uses specific snow regime events as a function of season to interoperate the major forcings – climate oscillations or specific storm tracks. Chapter 8 alludes to future applications of this work – highlighting the newly published MWR classification method of snow regimes as an excellent resource to combine with models, reanalysis products, and satellite observations.

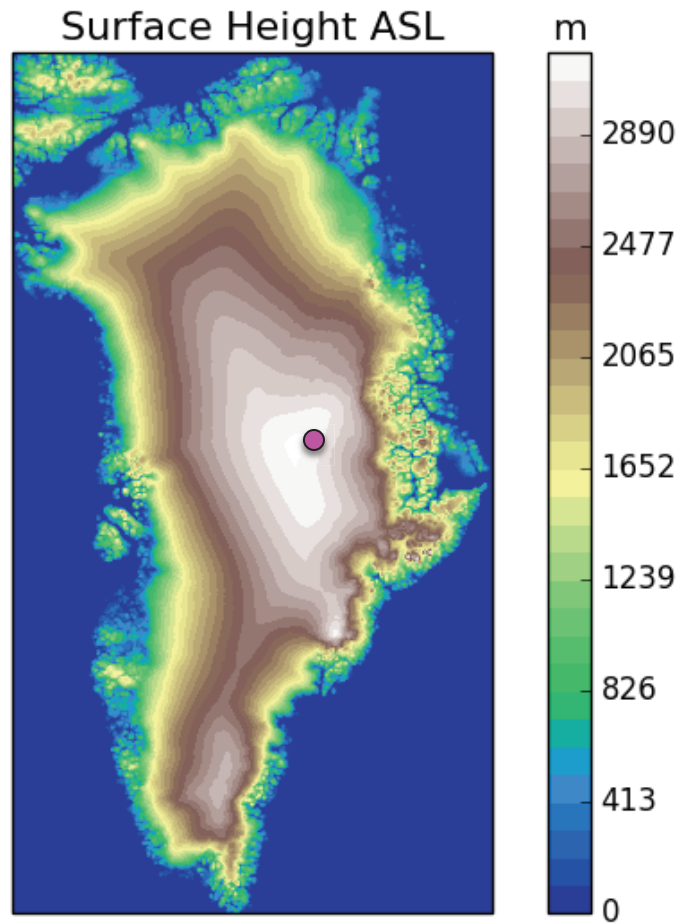


Figure 2.1 Figure showing the surface height of Greenland was created using measurements taken during the IceBridge campaign (Morlighem et al., 2015). The surface height combines the contributions from both the bedrock and ice sheet topography. Data were collected between January and December 2007. Spatial resolution is 150 by 150 meters.

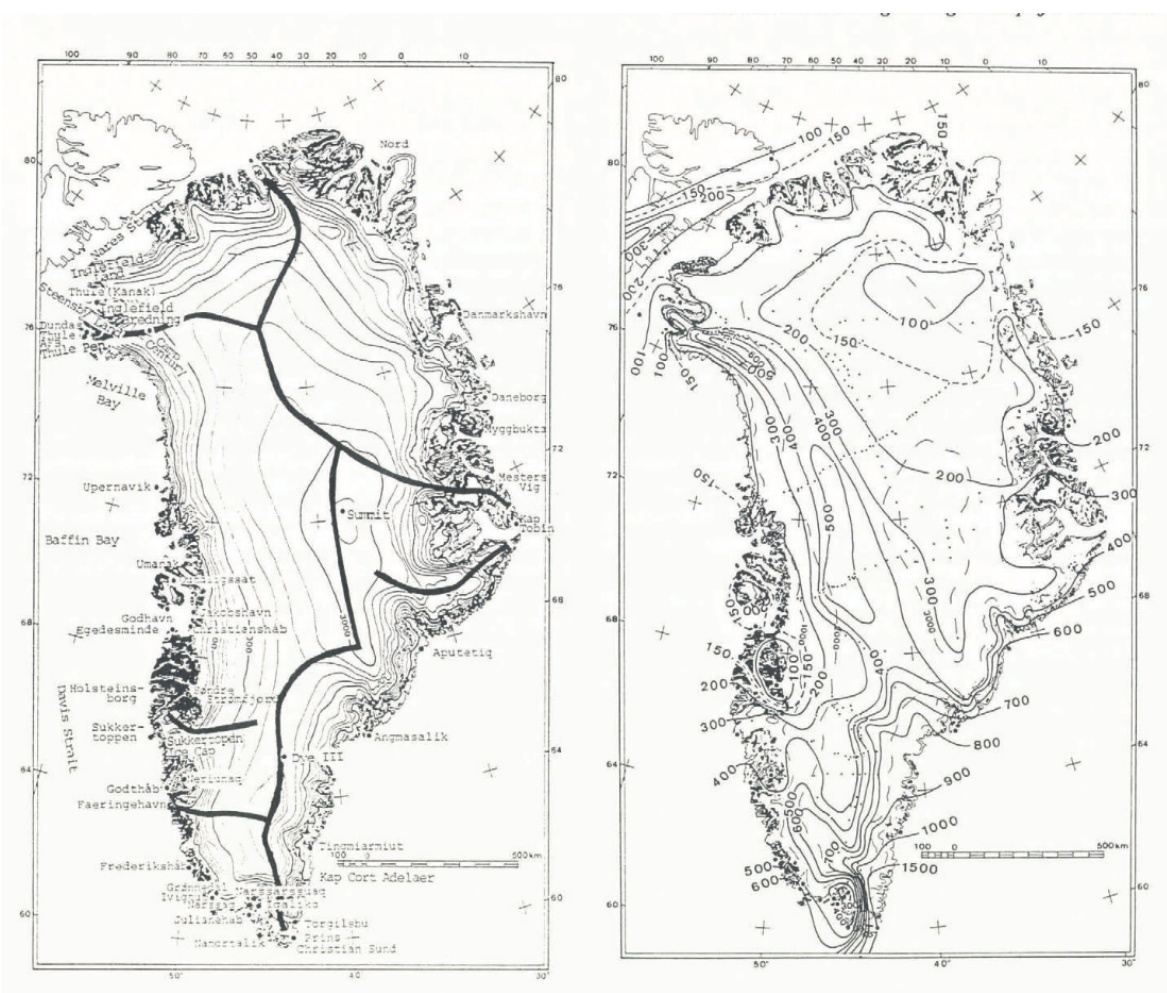


Figure 2.2 The left panel shows the complex terrain and major ridge features of the GIS, which influence the accumulation (Figure 5, Ohmura and Reeh, 1991). The right panel shows the annual accumulation in mm liquid water equivalent for Greenland (Figure 6, Ohmura and Reeh, 1991).

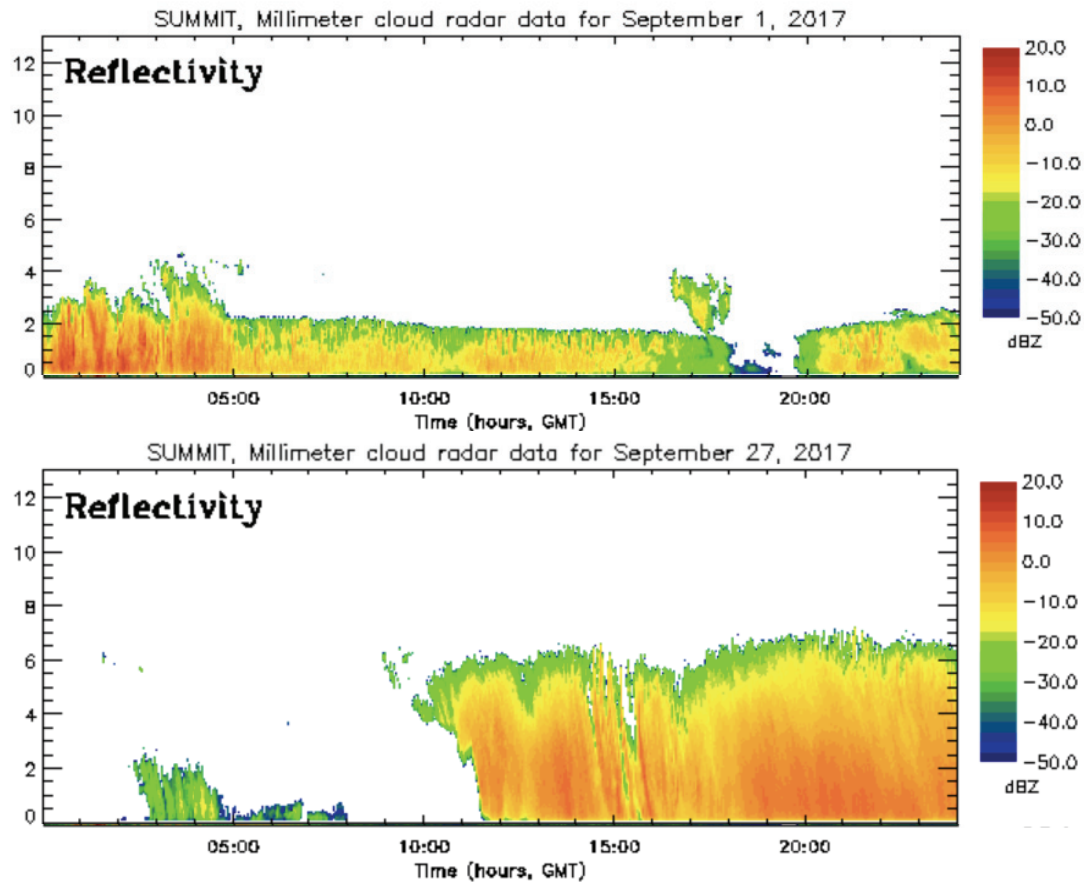


Figure 2.3 Example of an Arctic mixed phase cloud as observed by the cloud radar throughout the entire day on September 1, 2017 at Summit Station (top panel). Example of a deep ice cloud system as observed by the cloud radar on September 27, 2017 beginning at ~1200UTC at Summit Station (bottom panel). Figures from the Summit Data Browser (<https://www.esrl.noaa.gov/psd/arctic/observatories/summit/browser/>).

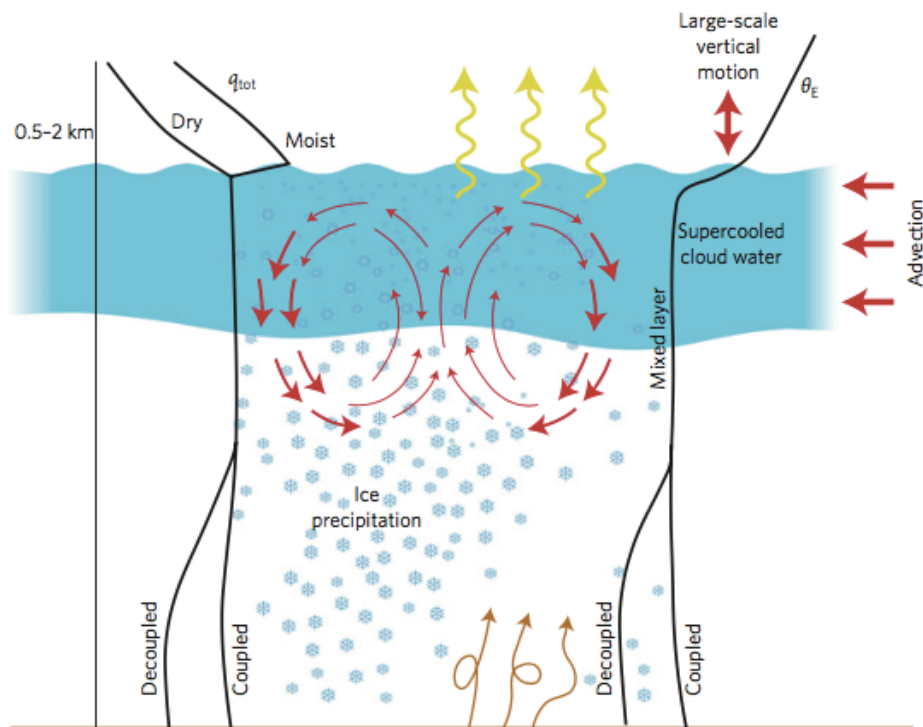


Figure 2.4 A schematic illustrating the primary processes and basic physical structure of Arctic mixed-phase clouds (Fig. 3 in Morrison et al., 2012).

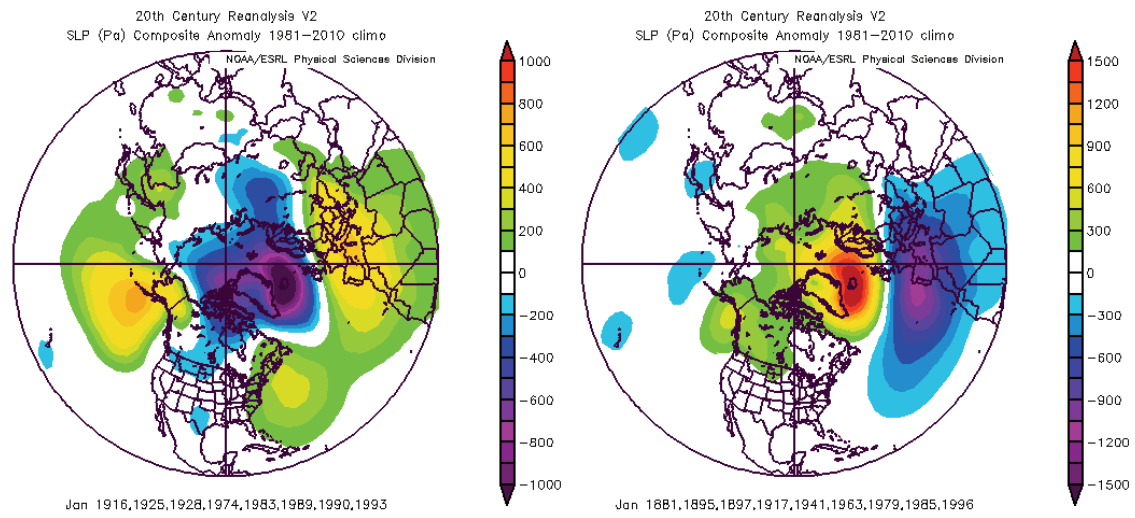


Figure 2.5 SLP maps for examples of NAO positive phase (left) and NAO negative phase (right; Compo et al., 2011; Figure from NOAA ESRL: https://www.esrl.noaa.gov/psd/data/20thC_Rean/timeseries/monthly/NAO/)

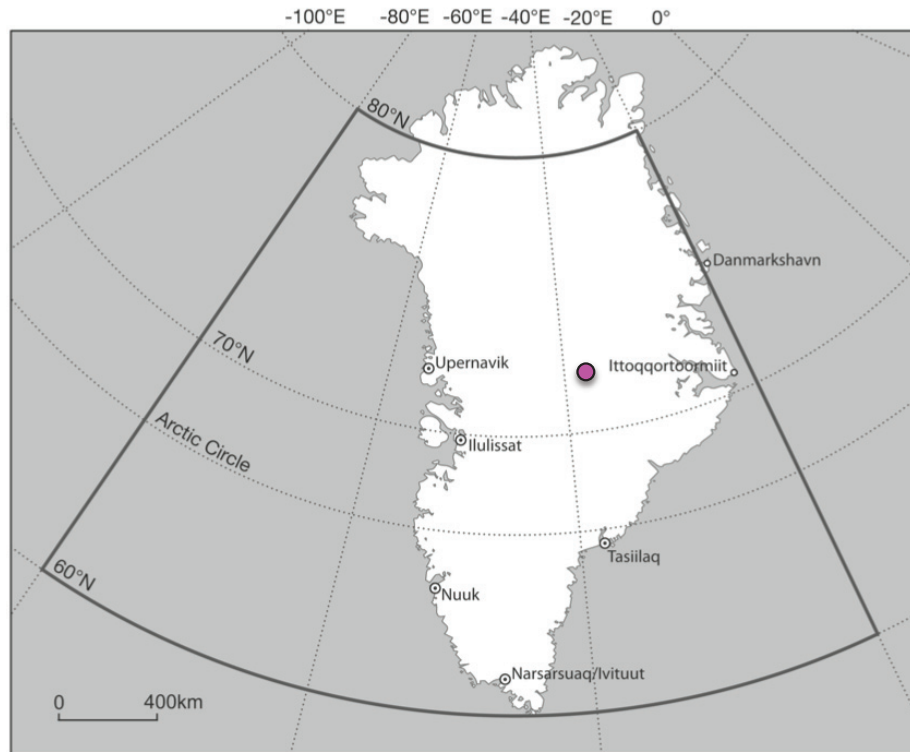


Figure 2.6 Map showing the Greenland Blocking Index region (60N to 80N and 80W to 20W; Figure 1 from Hanna et al., 2016).

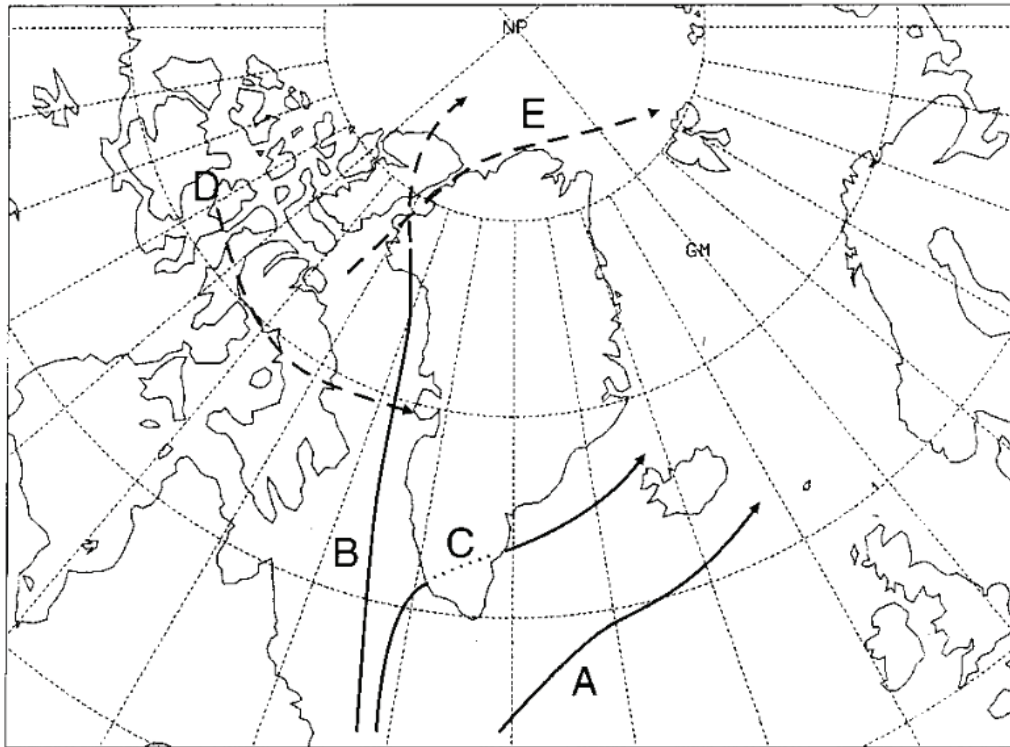


Figure 2.7 Schematic diagram showing the primary (solid lines) and secondary (dashed lines) cyclone tracks around Greenland. Dots denote discontinuity influenced by orography. Track B is a major storm track into Baffin Bay and Track C is a southern tip cyclone. Both of these tracks are linked to increased precipitation over the GIS (Figure 8 in Chen et al., 1997).

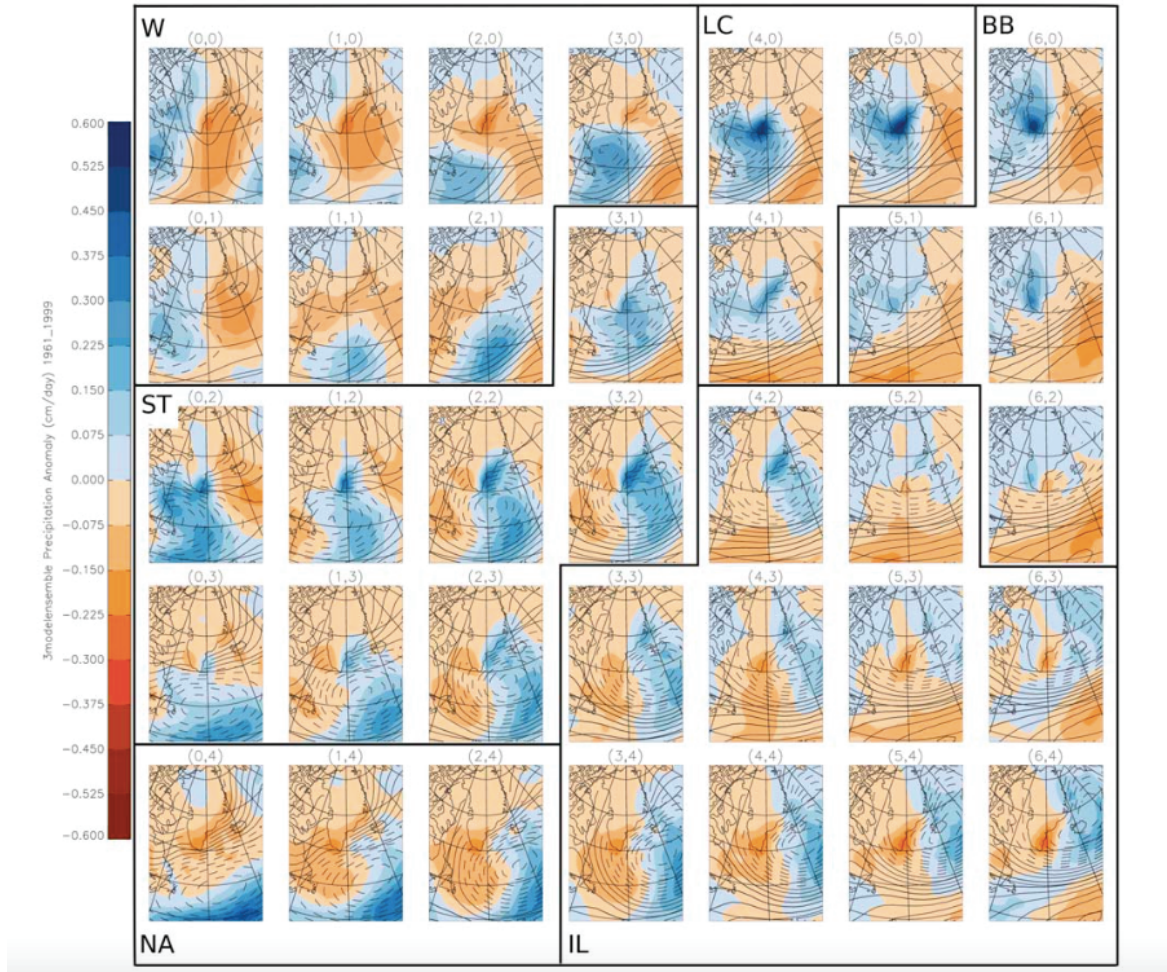


Figure 2.8 Sea level pressure anomaly patterns in the region around Greenland (contour lines, solid positive and dashed negative) and the associated precipitation anomalies (shaded contours, blue positive and red negative). The letters stand for W, weak; LC, Labrador cyclone; BB, Baffin Bay cyclone; ST, Southern Tip cyclone; NA, North Atlantic cyclone; IL, Icelandic Low cyclone (Figure 6 from Schuenemann et al., 2009).

Chapter 3

3 Datasets and Methods¹

Studying the characteristics of the precipitation and clouds above the GIS is made possible with observations from the ICECAPS instrument suite. Located at Summit Station, Greenland, the ICECAPS project has been in operation since 2010. Observations from specific instruments in the ICECAPS suite can be combined with reanalysis products and models to aid in better understanding of the atmospheric processes above the central GIS. The following sections describe the specific instruments and measurements used in these studies. Additionally, the radiative transfer and scattering models are outlined. The reanalysis products used to examine the regional meteorology are also summarized.

3.1 ICECAPS project and instrument suite

ICECAPS is modeled after other successful Arctic observatories and is similar in scope to facilities run by the Department of Energy's Atmospheric Radiation Measurement (ARM) Program (Ackerman and Stokes, 2003; Shupe et al., 2013). The ICECAPS instrument suite is supported by year-round technicians and support staff at Summit Station and is updated with new instruments, upgrades, and repairs by researchers every summer. Table 3.1 illustrates a brief overview of the ICECAPS instruments used in this study, including key specifications, measurements, and retrieved parameters. Figure 3.1 shows the location of Summit Station atop the GIS and the ICECAPS instrumentation setup. We employed data from a subgroup of the ICECAPS suite and a co-located 225

¹ Portions of this chapter are published in Pettersen et al. (2016) and in review Pettersen et al. (2017) and are copyright of the European Geophysical Union.

GHz MWR. The available measurements and retrieved values are further described in the following sections.

3.1.1 Microwave radiometers

ICECAPS gathers observations from three different passive MWRs all built by Radiometer Physics GmbH. The Humidity and Temperature Profiler (HATPRO) has seven channels from 22-32 GHz (near 22.24 GHz water vapor absorption line) and seven channels from 51-58 GHz (near oxygen absorption line; Rose et al., 2005). The high-frequency microwave MWR (MWRHF) has two high-frequency channels: 90 and 150 GHz. The two radiometers are run in a master-slave configuration and make coincident measurements every four seconds. Data from the third co-located MWR, which is sponsored by the Academia Sinica Institute of Astronomy and Astrophysics (ASIAA) group, observes downwelling radiation at 225 GHz and takes measurements every 4 seconds (Matsushita et al., 2013). Although all of the MWRs measure the downwelling atmospheric radiance at several elevation angles, in this work we only use data from zenith pointing.

Passive microwave radiometry is commonly used to derive liquid water path (LWP; Crewell et al., 2009) and precipitable water vapor (PWV) in the column. By combining the BTs observed from specific channels, PWV and LWP are derived. Historically, LWP and PWV at ARM sites are derived using the 23.84 and 31.40 GHz channels using a version of the MWR Retrieval (MWRRET) algorithm (Turner et al., 2007a). The physical retrieval method employs the Monochromatic Radiative Transfer Model (MonoRTM; Clough, et al. 2005) and the Liebe91 liquid water model (Liebe, 1991). It was found that the addition of high frequency channels to the retrieval algorithm

improves LWP accuracy, particularly for low LWP amounts. By adding the 90 GHz channel, the uncertainty is reduced from 20 – 30 g m⁻² to better than 12 g m⁻² (Crewell et al., 2003; Löhnert et al., 2003). The four channel MWRRETv2, which includes the addition of the 90 and 150 GHz channels, calculates an uncertainty of 4-5 g m⁻² for typical retrievals at Summit (MWRRETv2).

The reduced uncertainty at low LWPs is important as the cloud liquid water path on average at Summit (and the Arctic as a whole) is small as 80% of liquid-bearing clouds in the Arctic have less than 100 g m⁻² LWP (Turner et al., 2007b). However, the prior studies (Kneifel et al., 2010; Pettersen et al., 2016) show that high-frequency channels have enhanced brightness temperatures when ice is present in the column. Additionally, recent studies have indicated that many liquid water absorption models do a poor job adequately accounting for supercooled cloud liquid water (Turner et al., 2015; hereafter TKC15). We compared results from four channel MWRRETv2 retrievals using both the Liebe91 and TKC15 models. We found that the MWRRET retrieval had improved convergence when using TKC15 versus the Liebe91 cloud liquid water model, especially in the difficult to resolve ice affected cases. To further mitigate the effect of the enhanced BTs in the high frequency channel, we opted to use MWRRETv2 with the TKC15 model and only three channels to compute LWP and PWV: 23.84, 31.40, and 90 GHz. Due to computational expense, the MWRRET retrieval is run on the MWR data every 100 seconds.

Work in ice hydrometeor study outlined in Chapter 3 incorporates retrieved values of LWP into radiative transfer models. However the precipitation categorization method described in Chapter 4 purposely does not include any retrievals of LWP and relies purely

on BTs measured by the MWR. Chapters 5 and 6 focus on precipitation events using the methodology defined by Chapter 4 and does not use LWP.

3.1.2 Millimeter cloud radar

The Millimeter wavelength Cloud Radar (MMCR) is a zenith pointing, 35 GHz (Ka band) radar with processed measurements provided every ten seconds at a height resolution of 45 meters (Moran et al., 1998). The MMCR measures the profile of reflectivity, Doppler velocity, and Doppler spectral width in the column above. For the MMCR, hydrometeors with geometric diameters less than approximately 3 mm are in the Rayleigh scattering region (Kneifel et al., 2011). However, for ice hydrometeors larger than ~3 mm diameter the Rayleigh approximation breaks down (at this size, the MMCR starts to see Mie resonance effects) and the backscatter cross-section depends on ice habit (Kneifel et al., 2011; Petty and Huang, 2010).

The Doppler velocity measures the fall speed of particles toward the radar – this is dependent on the mass and projected area of the ice hydrometer population, thus some microphysical insight is gained from these fall speed values. However, the particles are embedded with a vertical wind field that will affect the measured fall speed.

Finally, the variance of the velocity in a given pulse volume, the Doppler spectral width, aids in determining turbulence and contains indicators of hydrometeor phase. Strong turbulence or multiple phases/habits in a cloud layer leads to large Doppler spectral width. On the other hand, uniform particle populations, such as for those precipitating out of a cloud, exhibit relatively low Doppler spectral width. By combining these measured quantities from the MMCR, we can infer many properties of the hydrometeors observed at Summit.

Retrieved values of snow rate (mm hr^{-1}) liquid water equivalent (LWE) were calculated using an empirically derived relationship from Matrosov, 2007 defined as:

$$Z_e = 56 S^{1.2} \quad (1)$$

Where Z_e is the maximum reflectivity value found between 200 and 800 meters above the MMCR and S is the snowfall rate in mm hr^{-1} LWE. Though there are differences in the ice habits and distributions for the observed events, this relationship holds well for cases with pristine crystals with negligible amounts of liquid water and riming. Such conditions are often observed at Summit (Matrosov, 2007; Shupe et al., 2013).

3.1.3 Ceilometer

The MWRRET retrieval gives the integrated cloud liquid water amount but no information about cloud altitude. Cloud base height (CBH) is estimated from a Vaisala Ceilometer (VCEIL). The VCEIL is a vertically pointing 905 nm pulsed laser system with 15 meter height resolution and takes a measurement every 15 seconds. Cloud base heights (up to three layers) are determined based on the backscattered signal received by the instrument. We use the first cloud base height retrieved from the VCEIL to define the base of the cloud liquid water layer in this study.

3.1.4 Radiosondes

This study also uses data from twice daily balloon-borne radiosondes (manufactured by Vaisala, models RS-92K and RS-92SGP) launched at Summit Station. The launches occur at approximately 1200 and 2400 Coordinated Universal Time (UTC), and gather in-situ measurements of temperature, pressure, relative humidity, and, in some cases, horizontal wind speed and direction. These thermodynamic profiles provide critical input for the radiative transfer modeling (see Sect. 3.2).

3.1.5 Precipitation Occurrence Sensor System

The precipitation occurrence sensor system (POSS) is a compact and deployable, continuous wave, X-band Doppler radar (Sheppard and Joe, 2008). The POSS samples approximately one cubic meter of air directly above the transmitter and receiver and is used for surface observations of precipitation type, amount, and frequency. The POSS measures the Doppler velocities and spectrum as well as reflectivities of hydrometers. We utilize two products from the processed POSS data: the POSS power units (Ppu) and the retrieved liquid equivalent snow rate. The Ppu is simply a value assigned to the zeroth moment of the Doppler spectrum analogous to integrated reflectivity, and can be used as a binary indicator of precipitation. The LWE snow rate retrieved by the POSS is based on a precipitation estimation algorithm and associated catch ratio outlined in Sheppard and Joe (2008).

3.1.6 Ice Particle Imaging Camera

The Ice Particle Imaging Camera (IcePIC) is similar to the snowflake photographing apparatus developed by Libbrecht (2007). During a snowfall event, a scientific technician captures falling ice onto a cold microscope slide (to limit snowflake melt) and then photographs the slide with a Nikon D50 DSLR camera mounted on a ~5.6X magnifying microscope body, which is stored in an outdoor shelter. Though these observations are not quantitative, they are helpful in providing some qualitative evidence as to what ice habits are falling during specific events.

3.1.7 Surface Meteorology Data and Observations

Surface meteorological data is acquired from the NOAA Temporary Atmospheric Watch Observatory (TAWO), which is operated by the Earth System Research Laboratory,

Global Monitoring Division. The observatory takes continuous measurements of temperature, water vapor, and winds at 2 and 10 meters above the surface at Summit Station. This work uses the 10 meter wind speed and direction data from the NOAA TAWO tower. General weather observations from the on-site NOAA science technicians are also used in this work.

3.2 Radiative Transfer Models

3.2.1 Clear Sky Radiative Transfer

Microwave emission and absorption of the dry gases and the water vapor (WV) are modeled using the radiosonde in-situ measurements of pressure, temperature, and relative humidity. The twice-daily radiosondes are linearly interpolated to the MWR observation times. We then employ MonoRTMv5.0 (Clough, et al. 2005) using inputs of layer temperature, pressure, and relative humidity from the interpolated dataset to compute the clear sky radiance at the MWR observed frequencies.

3.2.2 Absorption coefficients for gas and liquid water

The emission and absorption of the gases and liquid water in the atmospheric column are modeled using in situ observations of temperature and pressure and remotely sensed values of integrated water vapor, liquid water content, and cloud base height from the ICECAPS instruments. To compute the volume absorption coefficients of dry air and water vapor in the atmospheric column, we employ the method described in Sect. 3.2.1.

The liquid water absorption and emission is modeled using the TKC15 Model (Turner et. al., 2015) with inputs of liquid water content (LWC) at a defined cloud height and temperature. For altitudes above the radiosonde profile, a subarctic standard

atmosphere profile is assumed. The simulated emission is not sensitive to the details of the upper atmosphere profile, but systematic biases would be present if the atmosphere was artificially truncated at too low an altitude.

3.2.3 Successive Order of Interaction radiative transfer model

In ice cloud free atmospheres, the RT model need only consider the absorption and emission of atmospheric gases and liquid water. When ice is introduced into the column, multiple scattering can occur and we then must employ a radiative transfer model that accounts for scattering. The Successive Order of Interaction (SOI) RT model accurately simulates scattering for the infrared and microwave spectral region (Heidinger et al., 2006; O'Dell et al., 2006). The SOI model combines the layer-averaged optical properties and temperature in order to compute downwelling radiance at selected frequencies. The layer-averaged optical properties are calculated from the gas and liquid water absorption models (described above) and ice optical properties (further discussed in Chapter 4, Sect. 4.6.4).

The SOI modeled BTs can then be compared to MWR observations. For all cases used in this study we employed the SOI radiative transfer model, even when modeling non-scattering atmospheres that only include gases and cloud liquid water absorption. As is further discussed in the subsequent section, comparing the measured and modeled BTs at specific frequencies lends insight into the hydrometers present in the atmospheric column.

3.3 Reanalysis Data Products

Chapters 5 and 6 tie the observations of snowfall events at ICECAPS to associated dynamics over the GIS. Understanding the how the precipitation is advected over the GIS is important in illuminating what processes affect the mass balance. Since ICECAPS is a

point source, we can use observations in concert with reanalysis data to illustrate what is occurring over the GIS regionally. We examine surface and upper level patterns, as well as back-trajectory calculations of the air masses through use of reanalysis products.

3.3.1 ERA-Interim Reanalysis

The ERA-Interim is a global reanalysis product provided by the European Centre for Medium-Range Weather Forecasts (ECMWF; Dee et al., 2011). The ERA-Interim spans the past 38 years and has surface and pressure level profile data four times daily (0, 6, 12, and 18 UTC) with spatial resolution of 0.75° latitude and longitude. In Chapters 6 and 7, we use mean surface winds and sea level pressures for specific cases as well as calculate anomalies based on the 38-year history. We also use the ERA-Interim to examine upper-level mean winds and geopotential heights and their respective anomalies. We use a sub-grid of reanalysis data from latitude 34.5 to 84.0 degrees north and longitude 115 degrees west to 52.5 degrees east.

3.3.2 HYSPLIT and the NCAR/NCEP 40- year reanalysis project

Back-trajectories were calculated for air masses during snowfall events at Summit. Calculations were obtained using the NOAA Air Research Laboratory's Hybrid Single-Particle Lagrangian Integrated Trajectory (HYSPLIT) model, which computes simple air parcel back-trajectories to determine the origin of an air mass for a specified time range and location (Stein et al., 2015). HYSPLIT enables the visualization of the air as it moves towards Summit Station as well as the vertical motions. We created HYSPLIT back-trajectories with gridded meteorological output from the National Centers for Environmental Prediction (NCEP)/National Center for Atmospheric Research (NCAR) Reanalysis Project (Kalnay et al., 1996). The NCEP/NCAR reanalysis project incorporates

data from 1948 through present, with a frequency output of every 6 hours, global coverage at a spatial resolution of 2.5° , and 17 pressure levels.

3.3.3 Climate Indices

This work uses values for two climate indices: the North Atlantic Oscillation (NAO) and the Greenland Blocking Index (GBI). The NAO index is calculated as the difference between the mean sea level pressures of the Icelandic Low and the Azores high (Barnston and Livezey, 1987). This work uses daily calculations from January 1950 through present of the NAO index from the NOAA Climate Prediction Center (CPC). The GBI is a measure of the amount of blocking calculated by averaging the NCEP/NCAR Reanalysis (Kalnay et al., 1996) 500 mb geopotential heights over the region encompassing Greenland (60 to 80 degrees north and 20 to 80 degrees west; Fang, 2004; Hanna et al., 2016). GBI used in this work are daily calculations from January 1948 through June 2015 and are from the NOAA ESRL data repository.

Table 3.1 Subset of ICECAPS instruments used in this study (modified from Table 1 in Shupe et al., 2013).

Instrument Name	Specifications	Measurements	Derived Parameters
HATPRO	Frequencies: 22-32 GHz (7 channels) 51-58 GHz (7 channels) 2 to 4-second resolution	Downwelling Brightness Temperature	Precipitable water vapor, cloud liquid water path
MWRHF	Frequencies: 90 and 150 GHz. 2 to 4-second resolution	Downwelling Brightness Temperature	Precipitable water vapor, cloud liquid water path
MWRHF-225	Frequency: 225 GHz. 4-second resolution	Downwelling Brightness Temperature	Atmospheric opacity
MMCR	35 GHz (Ka band), 8-mm wavelength. 45-meter vertical bin size. 2-second resolution	Reflectivity, Doppler velocity, Doppler spectral width	Cloud micro and macro-physics, cloud dynamics, precipitation rate, ice water path
Ceilometer	905nm wavelength, 15-meter vertical resolution. 15-second resolution	Backscatter	Cloud-base height
POSS	10.5 GHz (X band), single bin, near surface, 1-minute resolution	Reflectivity, Doppler spectra	Precipitation occurrence and rate
RS-92K or RS-92SGP Radiosondes	Twice daily (00 and 12Z), 1-second resolution.	Temperature, relative humidity, pressure, winds	Cloud temperature, tropospheric thermodynamic structure
IcePIC	Canon D50 DSLR, 1.5 μm resolution, 6.1 megapixels	Digital photographs	Ice crystal habit, Qualitative assessment of riming, aggregation

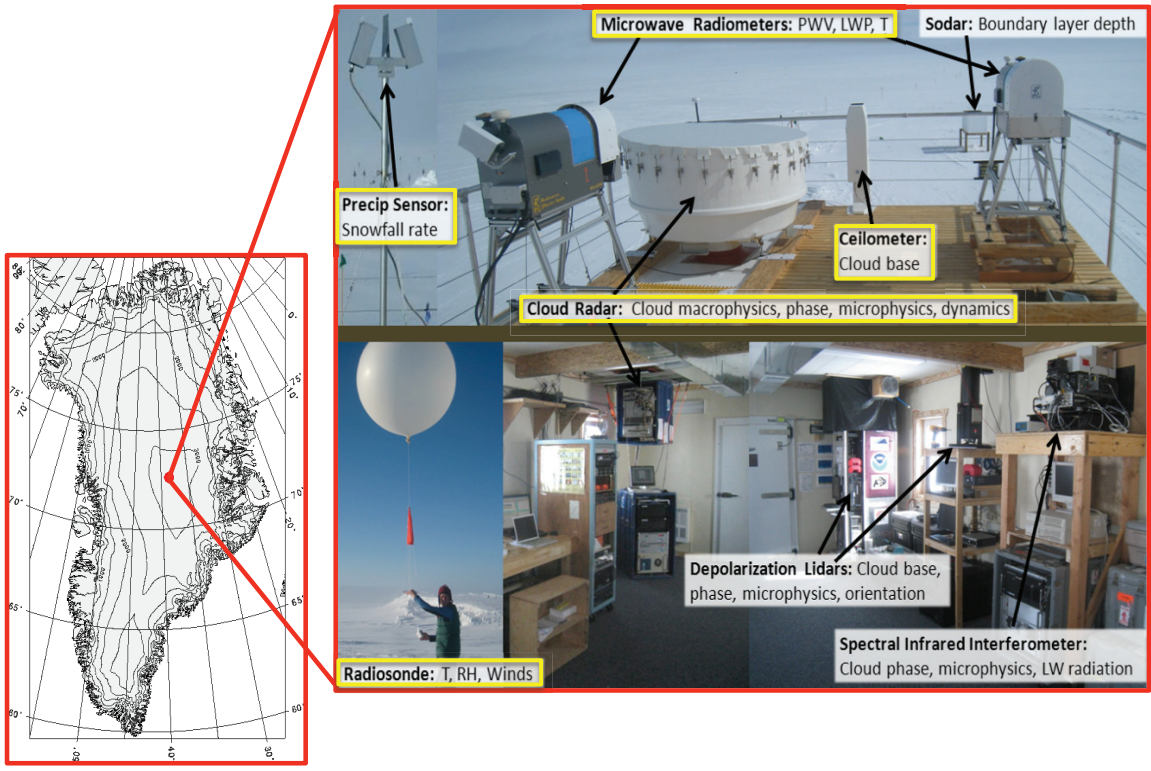


Figure 3.1 The ICECAPS Suite location at Summit Station, Greenland (left) and instrument suite (right). Instruments used in this study are highlighted with yellow outline (modified from Figure 1 in Shupe et al., 2013).

Chapter 4

4 Microwave signatures of ice hydrometeors above Summit, Greenland²

4.1 Introduction

Multi-instrument, ground-based measurements provide unique and comprehensive datasets of the atmosphere for a specific location over long periods of time and resulting data compliments past and existing global satellite observations. This study explores the effect of ice hydrometeors on ground-based, high frequency passive microwave measurements and attempts to isolate an ice signature for summer seasons at Summit, Greenland from 2010 – 2013. Data from a combination of passive microwave, cloud radar, radiosonde, and ceilometer were examined to isolate the ice signature at microwave wavelengths.

By limiting the study to a cloud liquid water path of 40 g m^{-2} or less, the cloud radar can identify cases where the precipitation was dominated by ice. These cases were examined using liquid water and gas microwave absorption models, and brightness temperatures were calculated for the high frequency microwave channels: 90, 150, and 225 GHz. By comparing the measured brightness temperatures from the microwave radiometers and the calculated brightness temperature using only gas and cloud liquid water contributions, any residual brightness temperature difference is due to emission and scattering of microwave radiation from the ice hydrometeors in the column.

² Portions of this chapter are published in Pettersen et al. (2016) and are copyright of the European Geophysical Union.

The ice signature in the 90, 150, and 225 GHz channels for the Summit Station summer months was isolated. This measured ice signature was then compared to an equivalent brightness temperature difference calculated with a radiative transfer model including microwave single scattering properties for several ice habits. Initial model results compare well against the four years of summer season isolated ice signature in the high-frequency microwave channels.

4.2 Enhanced ice signature

MWRs are common remote sensing instruments, which make passive measurements of radiance at specific frequencies (described in detail in Chapters 1 and 2). Kneifel et al. (2010; hereafter K10) demonstrated the presence of an enhanced BT signature from ice hydrometeors in downwelling microwave radiance observations for a case study of snowfall in the Alps using ground-based MWRs. The high-frequency channels (90 and 150 GHz) are considered “window channels”, since these frequencies are free of strong gas absorption lines. At these frequencies the clear sky downwelling radiance is very small, so when ice or liquid water is present these channels see a warmer BT, as seen by the K10 study.

If there are ice hydrometeors present in the atmosphere column, they will have two effects on the observed downwelling radiance at the surface: emission of radiation and scattering of the surface-emitted radiation back to the instrument. In general, ice hydrometeors have fairly high single scatter albedo (SSA) at high microwave frequencies, regardless of habit and size distribution. Typically the SSA will be in the range 0.8-0.9 (Liu, 2008), which implies that scattered radiation is likely the larger effect, but there may still be significant emitted radiation from the ice hydrometeors. Since some of the ice

signature is scattered surface radiation, the magnitude of the effect is related to both the surface temperature and emissivity. The surface emissivity of different types of snow seen at Summit varies in the range of 0.60 to 0.91 for the higher frequency passive microwave channels used in this study (Yan et al., 2008). This makes the ice signature challenging to model because it depends on both properties of the ice hydrometeors (habit, size distribution, amount, etc.) and the surface (temperature, roughness, emissivity).

We propose that the enhanced BT from the ice hydrometeors can be isolated and quantified by combining the observed data from instruments in the Integrated Characterization of Energy, Clouds, Atmospheric State, and Precipitation at Summit project (ICECAPS; Shupe et al., 2013) with radiative transfer models of the gas and liquid in the atmosphere. By doing this we are enhancing the K10 study by expanding it to multiple years of data in an Arctic environment with very low amounts of liquid water and precipitable water vapor, which present unique challenges. Additionally, since the temperatures at Summit Station are below freezing, we are implementing a newly developed cloud liquid water model for more accurate retrievals in the presence of supercooled water (Kneifel et al., 2014; Turner et al., 2015). Because the ice signature is also dependent on ice crystal habit and size distribution, relying on a small number of precipitation events to derive the ice signature may bias the result toward specific precipitation situations. The large dataset from the ICECAPS Project allows for the average ice signature to be computed over many precipitation events, thus reducing this potential sampling bias.

4.3 Merged Data

For this work, we employed the ICECAPS instrumentation outlined in Chapter 3, Sect. 3.1, to measure and isolate an enhanced signal from the HF MWR channels. Observations from the MWR, MMCR, ceilometer, and radiosondes were merged together to a common sampling time, defined by the MWRRET retrieval (every 100 seconds). The slower datastream (twice daily radiosonde) is linearly interpolated to the common sampling time, and the faster datastreams are simply subsampled at the MWRRET retrieval times. We interpolate all the data to the fixed height grid defined by the MMCR.

For an example day, we use data from the prior day's radiosonde launch (day -1, 2400 UTC) along with the two radiosondes launched for the given day (1200 and 2400 UTC) and linearly interpolate the temperature, pressure, and relative humidity of each layer in the column throughout the day to the MWRRET temporal grid. The vertical layering uses the MMCR vertical grid up to 7.5 km altitude above ground level (AGL). Above this altitude, the layering becomes gradually coarser and extends to up 30 km AGL. Next, the MWR retrieved PWV is used to scale the interpolated relative humidity from the radiosonde – this is because the PWV retrieved value is higher temporal resolution and more accurate than the radiosonde data (Turner et al., 2003). Finally, a single layer cloud is inserted into the vertical grid at the first cloud base height (CBH1) detected by the VCEIL, with the MWR retrieved LWP value.

4.4 Ice hydrometeor behavior as observed by ICECAPS

Similar to K10, we compared the BTs in the high frequency channels of the MWRs to the output from the radiative transfer model calculation. The K10 study employed a radiative transfer model that included absorption/emission and scattering to simulate the behavior of

the ice signature based on the habit, surface emissivity, etc. Different from K10, we do not initially include an ice scattering model for the purpose of identifying the ice signature.

We instead attempt to isolate the ice radiative signature in the observations by accounting for any other potential emission or absorption sources within the column. If we compare the calculated BT using only gas and liquid water to the observed BTs from the MWRHF, any difference should be due to the ice signature. Consequently, the average ice hydrometeor radiative signature can be computed over many precipitation events by extending the analysis to the full available ICECAPS dataset.

4.4.1 Characterization of ice precipitation at Summit

We can acquire statistics of different precipitation regimes at Summit by merging all available MMCR data and plotting all data as a two-dimensional occurrence histogram, with the vertical axis representing the height dimension and the horizontal axis representing a radar measurement (for example, reflectivity). Figure 4.1a is a two-dimensional histogram (2DH) of all the reflectivity values measured by the MMCR for any given time within the summer months – June, July, August, (JJA) – 2010 through 2013. We can highlight the types of hydrometeors observed during specific atmospheric conditions by filtering the MMCR reflectivity 2DH, illustrated in Fig. 4.1a, as a function of other ICECAPS instrument measurements or derived parameters.

Filtering the MMCR 2DHs by the corresponding MWR-derived LWP for the same time period can identify regimes in which ice hydrometeors are likely present. We partition the data with a threshold LWP value in order to select cases that have low LWP. The exact threshold value is arbitrary, as the resulting 2DHs are not sensitive to the particular threshold value. We tried values of 5, 10, and 40 g m^{-2} and observed qualitatively similar

2DHs. We selected a 40 g m^{-2} LWP threshold for the remaining analysis, since this yielded a larger number of cases for the study (as opposed to the lower LWP threshold values).

As depicted in Fig. 4.1b and c, the MMCR reflectivity 2DH for JJA has been filtered by cases when LWP was less than and greater than 40 g m^{-2} , respectively. The resulting 2DHs have different characteristics from each other and lend insight to the behaviors of the hydrometeors in each case. For the case of LWP less than 40 g m^{-2} , the 2DH illustrates common ice hydrometeor behaviors: a fall-streak like pattern of increasing reflectivity with decreasing height and peak near-surface reflectivities above 0 dBZ (see Fig. 4.1b). In contrast, the reflectivity 2DH for the cases where LWP is greater than 40 g m^{-2} has a concentration of counts at a broader range of smaller reflectivities located at lower altitude, likely indicating dominance of shallow mixed ice and supercooled water cloud (though there is also a faint signal indication of some fall-streak behavior; see Fig. 4.1c). The reflectivities shown in Fig. 4.1b for less than 40 g m^{-2} LWP cases have characteristics of deep, precipitating ice cloud, while the greater than 40 g m^{-2} LWP cases show features similar to the shallow mixed-phase stratocumulus (Fig. 4.1c). Additionally, Fig. 4.1 panels d through i, depict the Doppler velocities and spectral width measurements from the MMCR as 2DHs for all LWPs, less than 40 g m^{-2} , and greater than 40 g m^{-2} . The features seen in the Doppler velocity and spectral width 2DHs for the cases less than 40 g m^{-2} are consistent with the characteristics of deep, precipitating ice cloud (high fall speeds and low spectral widths throughout the column, relative to greater than 40 g m^{-2} LWP cases).

Additionally, we illustrate the MMCR products depicted in Fig. 4.1 as a fraction of counts when LWP was less than and greater than 40 g/m^2 , respectively (see Fig. 4.2, b and

c, e and f, h and i). The resulting partitioning of the 2DHs between the low and high LWP conditions shows the different characteristics in the two regimes and lends insight to the occurrences of the hydrometeor characteristics in each case. The broad pattern showing increasing reflectivity with decreasing height, and peak reflectivities above 0 dBZ, is primarily observed in less than 40 g/m^2 LWP conditions with 75 – 90 % of the occurrences. The greater than 40 g/m^2 LWP conditions show higher relative occurrence of 35 – 50 % at smaller reflectivities located at lower altitude. Additionally, Fig. 4.2 panels e and h, depict the Doppler velocities and spectral width measurements as 2DHs as the percentage of occurrence for the less than 40 g/m^2 LWP conditions, and panels f and i show the occurrence for the greater than 40 g/m^2 LWP conditions.

The frequency of cases in JJA where the LWP is greater than 40 g m^{-2} is ~22%, while the cases where LWP is less than 40 g m^{-2} is ~63% of the time, and clear sky is the remaining 15% of cases (i.e., where the MMCR reflectivity is less than -60 dBZ). To maximize the likelihood of observing ice dominated cases, we limit our work to focus on cases in JJA with LWP of less than 40 g m^{-2} . As stated above, the cases with LWP greater than 40 g m^{-2} show features consistent with the shallow mixed-phase stratocumulus and by filtering out some of these events, we can better focus the study on the deeper, precipitating ice clouds. Since cases with LWP of less than 40 g m^{-2} represent the majority at Summit during the summer months, we can use this filter to get an accurate characterization of ice hydrometeor behavior while limiting interference from higher liquid water path.

We argue that the large radar reflectivity values are directly correlated to ice backscatter and cannot be from liquid precipitation, as Summit is never above freezing and

thus large liquid hydrometeors (greater than 80 μm diameter) are highly unlikely to occur (Pruppacher and Klett, 2000). Since we do not expect to see liquid hydrometeors larger than cloud droplets at Summit Station, MMCR observed reflectivities greater than -15dBZ should be indicative of ice (Frisch et al., 1995).

4.4.2 Enhanced brightness temperatures in the high frequency channels

As postulated from previous case studies in K10, the higher frequency channels in the ground-based zenith-pointing MWRs will see an enhanced BT in the presence of ice in the column. Thus, we examine the difference between the measured BTs from the 90 and 150 GHz channels and the SOI model outputs (with no ice included, gas and liquid water contributions only) at that same frequency. As illustrated in the contour plot of the JJA comparison in Fig. 4.3c and d, there is an increase in the difference of the observed minus modeled BTs as a function of the MMCR reflectivity converted to what we refer to as “ Z_{PATH} ”, though very small in the 90 GHz channel.

The Z_{PATH} is simply the column-integrated reflectivities with units of $\text{mm}^6 \text{m}^{-2}$. This MMCR Z_{PATH} measurement is related to the total amount of hydrometeor backscatter in the atmospheric column. The use of Z_{PATH} is advantageous because it acts as a proxy for ice water path (IWP) yet does not rely on conversions that are sensitive to ice habit (Kulie et al., 2010). Z_{PATH} is defined as:

$$Z_{\text{PATH}} = \int 10^{0.1 * R(z)} dz. \quad (1)$$

Where $R(z)$ is the observed radar reflectivity profile in units of dBZ.

The observed minus modeled BT differences at 90 and 150 GHz have a clear positive dependence on Z_{PATH} . As stated in the previous section, we do not expect to see any liquid hydrometeors at reflectivities greater than -15dBZ at Summit since there is no

“warm rain” process, which means that large Z_{PATH} values are indicative of ice. Therefore, the relationship between the BT differences at 90 and 150 GHz and the MMCR Z_{PATH} suggest that the enhanced BT signature is caused by ice hydrometeors.

4.4.3 Depressed brightness temperatures at 31.40 GHz

The lower frequency channels (23.84 and 31.40 GHz) should exhibit little to no effect from the presence of ice hydrometeors in the atmospheric column, as the microwave radiation at these frequencies is comparatively insensitive to ice hydrometeors (Johnson et al., 2012). Thus we expect the histogram contours to be nearly vertical at the 23.84 and 31.40 GHz for the relationship between the BT differences and the integrated reflectivity (Z_{PATH}). However, as seen in Fig. 4.3b, the 31.40 GHz channel shows a clear negative dependence on Z_{PATH} at the highest values. There is no physical mechanism by which ice hydrometeors could decrease the observed downwelling radiance. This result implies an issue with the input values implemented in the radiative transfer model, as it is unlikely for the low frequency channels at 23.84 and 31.40 GHz to see much contribution from ice in the column.

Two of the inputs for the radiative transfer model are retrieved values based on BTs from the MWRs: the PWV and LWP. As explained in Chapter 3, Sect. 3.1.1, the retrieval for the PWV and LWP employ a three-channel algorithm, which includes the 90 GHz channel. Though we tried to mitigate the effect of the ice by using the three-channel algorithm, the enhanced BT in the 90 GHz still has a significant impact on the retrieved LWP and PWV. More precisely, the retrieval will tend to adjust the LWP and PWV in order to account for the enhanced BT from the ice hydrometeors, leading to an overestimate of LWP and underestimate of PWV.

4.5 Liquid water path retrieval influenced by ice

As postulated in the previous section, we believe that the MWR retrieved LWP (PWV) values are biased high (low) when a significant ice signature is present in the column due to the retrieval incorporating the 90 GHz MWR channel. However, if we use only a retrieval based on the lower frequencies of 23.84 and 31.40 GHz, the random error in LWP increases dramatically to 20 – 30 g m⁻², which is a large fractional error (>50%). Thus, a relationship for the LWP and PWV biases in the three-channel retrieval as a function of the MMCR derived Z_{PATH} must be determined to accurately distinguish the ice signature. We developed a first-order correction of the estimated MWRRET retrieval biases, where the intention of this correction is to recover the ice signature, not to produce a formal correction to the ice-influenced LWP and PWV retrievals.

4.5.1 Ice signature influence on retrieved liquid water

As illustrated in Fig. 4.3, the difference between measured and modeled BTs as a function of Z_{PATH} , analogous to the amount of ice in the column, decreases in the 31.40 GHz. This effect is an artifact in the simulated BTs caused by the following chain of events:

1. The presence of ice increases the observed BTs at 90 GHz but has little effect on the lower frequencies.
2. Since the retrieval does not include effects from ice, the retrieval accounts for this enhanced signal in the 90 GHz channel by increasing (decreasing) the retrieved LWP (PWV) thus producing a positively (negatively) biased LWP (PWV) estimate.

3. Since the spectral absorption for the three water states (vapor, liquid, ice) have different shapes, the retrieval cannot reduce the modeled-measured BT bias to zero for all channels.

To better illustrate this idea it is useful to look at Fig. 2 from K10, where the optical thickness as a function of frequency is plotted for several absorption models – for example, water vapor, liquid water, ice by habit, etc. The liquid water and ice total optical depths (τ) are less than 0.2 for these frequencies. Since the total τ is low, we can make two simplifying approximations: first, the transmission to any atmospheric layer in the column is nearly 1; and second, the change in transmission through a layer is approximately the change in τ for that layer. This implies the BTs are a linear combination of τ for each atmospheric component.

The bias in the simulated BT, shown in Fig. 4.3, suggests that the MWRRET retrieved PWV and LWP may be influenced by the presence of ice hydrometeor signature in the 90 GHz channel used in the retrieval. Since the MWRRET does not include ice hydrometeors in the radiative transfer calculation, it can only fit retrieval channel observations by adjusting the PWV and LWP. The higher optical depth for liquid water at 90 GHz suggests that MWRRET adds extra LWP to account for the observed microwave ice signature. This will increase the forward modeled BT for the 23.84 and 31.40 GHz channels as well. Since there will be effectively zero ice signature at the low frequency MWR observations, the extra LWP will cause the low frequency BTs to be biased high. The retrieval partially compensates for the high BT bias at low frequencies by decreasing the PWV, which will reduce the simulated BT primarily at the 23.84 GHz channel, which is near the water vapor absorption line. Figure 4.4 shows these biases in a schematic

fashion. Because the liquid absorption model uses the MWR retrieved LWP and PWV as inputs to the SOI, a correction for the retrieved LWP and PWV in the presence of ice is necessary to accurately quantify the ice impact on passive microwave BTs.

4.5.2 Ice influenced liquid water path correction

The lower frequency channels are comparably insensitive to ice (Johnson et al. 2012), so we focus on the 23.84 and 31.40 GHz channels to derive a first-order estimate for the MWRRET LWP and PWV biases from the ice signature. In order to correct for the apparently biased PWV and LWP, we make an ad-hoc linear correction to the retrieved values. We assume the PWV and LWP bias are linearly related to the Z_{PATH} . As described in the previous section, the channels used in the retrieval, the RT is in the linear regime. Thus, the PWV and LWP biases are linearly related to biases in the forward modeled BT, with their relationships described by the forward model Jacobian (K). Formally, we if write the coefficients relating the Z_{PATH} and the retrieval bias as e_{LWP} and e_{PWV} , then the forward model perturbation can be expressed as:

$$\begin{bmatrix} \delta\text{TB}_{23.84\text{GHz}} \\ \delta\text{TB}_{31.4\text{GHz}} \end{bmatrix} = \begin{bmatrix} K_{23.84\text{GHz, PWV}} & K_{23.84\text{GHz, LWP}} \\ K_{31.4\text{GHz, PWV}} & K_{31.4\text{GHz, LWP}} \end{bmatrix} \begin{bmatrix} e_{\text{LWP}}Z_{\text{PATH}} \\ e_{\text{PWV}}Z_{\text{PATH}} \end{bmatrix} \quad (2)$$

or:

$$\delta\text{TB} = \mathbf{K}eZ_{\text{PATH}} \quad (3)$$

Inverting Eq. 3 to solve for the e coefficients yields:

$$e = \mathbf{K}^{-1}\delta\text{TB} \frac{1}{Z_{\text{PATH}}} \quad (4)$$

The linear relationship between δTB and Z_{PATH} can then be estimated from Fig. 4.5a and c, by measuring the slope of the point distribution. For the 23.84 GHz result, the slope is

zero, which is due to compensating errors in LWP and PWV. For 31.40 GHz, the slope is approximately -3.3×10^{-4} K per $(\text{mm}^6 \text{m}^{-2})$. Inserting these values into equation 4 yields a value of -1.3×10^{-4} g m^{-2} per $(\text{mm}^6 \text{m}^{-2})$ for eLWP and 4.4×10^{-6} cm per $(\text{mm}^6 \text{m}^{-2})$ for e_{PWV} .

To utilize these corrections in our modeling framework, the Z_{PATH} from the MMCR is multiplied by the scaling factor, and the PWV and LWP are adjusted accordingly (for example, for a Z_{PATH} of $10^4 \text{mm}^6 \text{m}^{-2}$, the correction would reduce the LWP by 1.3g m^{-2} and increase the PWV by 0.044 cm):

$$LWP_{\text{corrected}} = LWP_{\text{retrieved}} + e_{\text{LWP}} \times Z_{\text{PATH}} \quad (5)$$

$$PWV_{\text{corrected}} = PWV_{\text{retrieved}} + e_{\text{PWV}} \times Z_{\text{PATH}} \quad (6)$$

The corrected PWV and LWP are then used in the forward RT simulation with the SOI framework.

Returning to Fig. 4.4, we show the effect of these corrections for a standard profile at Summit with 0.1 cm PWV and 20g m^{-2} LWP. The top panel (a) shows the simulated downwelling microwave radiance spectrum with no ice included in the simulation, and the simulated spectrum with the biased PWV and LWP obtained by the retrieval. The second panel (b) shows the same simulated data after subtracting the simulated spectrum with no ice. The effect of the biased LWP and PWV on the microwave spectrum are shown independently (blue and green lines, respectively) and combined (cyan line). The residuals that are minimized by the retrieval (observed radiance minus forward model radiance) are the differences between the cyan line and the black “X”s. We see the compensating biases at 23.84 GHz, which minimizes the magnitude of the residuals at 23.84 GHz, as well as the opposite signs for the residuals at 31 GHz (negative) and 90 GHz (positive). The cyan line

represents the retrieval's solution to minimizing the residuals when it cannot correctly account for the ice signature, which impacts the observations from high frequency microwave channel (90 GHz).

Comparison of the MWR observed data with the radiative transfer model – using the LWP and PWV corrections for ice – for the JJA season from 2010 through 2013 for LWP of less than 40 g m^{-2} in the 23.84 and 31.40 GHz channels are insensitive with respect to the integrated reflectivity (as seen in Fig. 4.5b and d). This correction is successful in removing the high (low) LWP (PWV) incorporated from the ice signal, as the 31.40 GHz channel comparison shows no dependence on moderate values of Z_{PATH} . With this successful evaluation of the ice influenced LWP and PWV, we can rerun the model on the other channels and characterize the signature from the ice hydrometeors because ϵ_{LWP} and ϵ_{PWV} are frequency independent.

4.6 Observed Brightness temperature differences from ice

We present the LWP and PWV corrected results for the 23.84, 31.40, 90, and 150 GHz channels. The lower frequency MWR channels exhibit insensitivity to the ice (Fig. 4.5b and d), while the higher frequency MWR channels exhibit enhanced BTs when ice is present (Fig. 4.6). Additionally, we present data from a co-located 225 GHz MWR, which exhibits even larger BT differences with respect to the ice. Finally, we recast the results from these five MWR channels and compare them to each other. We also show preliminary results from a simple radiative transfer simulation as a first-order comparison of modeled results against the MWR observed ice signature enhanced BTs in the 90, 150, and 225 GHz channels.

4.6.1 Brightness temperature differences with corrected LWP and PWV

All data presented are events in JJA with LWP of less than 40 g m^{-2} . The measured MWR observations are compared to the radiative transfer model including the LWP and PWV corrections for ice. The results for the lower frequency channels, shown in Fig. 4.5b and d, no longer depend on the Z_{PATH} – they should be insensitive to ice for most Z_{PATH} . In the high frequency channels, 90 and 150 GHz, there is clear relationship between BT difference and Z_{PATH} indicative of ice enhanced BTs (Fig. 4.6a and b). At the highest observed Z_{PATH} values (about $10^5 \text{ mm}^6 \text{ m}^{-2}$), BTs are enhanced anywhere from 3 – 7 K in the 90 GHz channel and 10 – 30 K in the 150 GHz channel.

4.6.2 Brightness temperature differences at 225 GHz

Co-located with the ICECAPS measurements is the ASIAA a very high frequency MWRHF-225, which allows us to extend this study to include a 225 GHz channel. As the effect of ice on this frequency from ground observations has not yet been explored, the observed ice effect in the 225 GHz channel is a new application of this instrument. As expected, the 225 GHz exhibits a large BT enhancement due to ice (Fig. 4.6c). The MWRHF-225 was deployed in mid 2011, so the dataset is somewhat smaller than the ICECAPS dataset already described. In addition, the MWRHF-225 does have slightly different time coverage (e.g., the instrument downtime and QC flags are disjoint from the HATPRO and MWRHF). The dataset with all 5 MWR channels covers only the union where all instruments collected good data. At the highest Z_{PATH} values within the combined datasets in JJA from 2011 to 2013, the 225 GHz has enhanced BTs of up to 50 K at the highest Z_{PATH} . The 225 GHz results continue the trend seen in the other high frequency channels (150 and 90 GHz): the Z_{PATH} value above which the BT enhancement

occurs appears to decrease as the MWR frequency increases, implying increased sensitivity to the ice (Fig. 4.6).

4.6.3 Multi-frequency comparison of brightness temperatures differences

By plotting the difference in the observed minus calculated BTs in the MWR channels as a function of each other, one may gain insight about the spectral character of the ice signature in the microwave. Figure 4.7 depicts the BT difference of four of the MWR channels with respect to that of the 90 GHz: 23.84, 31.40, 150, and 225 GHz. Additionally, the binned values of the BT differences are colored by logarithm of the average Z_{PATH} within the bin, thus, providing a visual reference for the relative ice amount.

In the top of Fig. 4.7 (panels a and b), the 23.84 and 31.40 GHz BT differences are plotted and binned on the y-axis versus the values for the 90 GHz. Though the Z_{PATH} values increase as a function of the difference in BT in the 90 GHz, both the 23.84 and 31.40 GHz have the same Z_{PATH} values throughout most cases (i.e., the Z_{PATH} is neutral in the y-axis for all but the highest Z_{PATH}), which is expected as the lower frequency channels are comparatively insensitive to the ice. However, in panel c of Fig. 4.7, the observed enhanced BT at 150 GHz is plotted versus the 90 GHz and there is an approximately linear relationship between the ice effects at the two frequencies – with a slope of about 4 K BT difference in 150 GHz for every 1 K in 90 GHz. For both the 90 and 150 GHz, as the difference in the BT increases the Z_{PATH} values do as well (though the 150 GHz is more sensitive to the Z_{PATH} than the 90 GHz and therefore the effect of the BT enhancement occurs at a lower Z_{PATH} value). In the last plot in Fig. 4.7 (panel d), we compare the enhanced BT values in the 225 GHz channel to those in 90 GHz and again have a linear relationship between the ice effects in the two channels. Additionally, the slope of the 225

versus the 90 GHz BT differences is steeper than the 150 versus 90 GHz – for every 1 K in 90 GHz, there is a corresponding 10 K difference in the 225 GHz. As with the 90 and 150 GHz case, the 90 and 225 GHz multi-frequency plot shows increasing Z_{PATH} values as a function of larger BT differences in both channels.

4.6.4 Comparison of ice signatures observed with scattering model results

Now that we have an estimate of the passive microwave ice signature, we can compare to modeled results with our SOI framework, described in Chapter 3, Sect. 3.2.3. We can find the difference in modeled BTs in the presence of ice using SOI by running the model twice: once including ice with contributions from the atmospheric gases and once with only the gases. The difference between these two runs produce differences in BTs that allow for direct comparison with our multi-frequency results (Fig. 4.7), and an assessment of the ice microwave optical property models for the ice hydrometeors at Summit, Greenland.

For a first-order ice habit study, we used the temperature-dependent ice particle size distribution parameterization from Field et al. 2007 (hereafter F07) for the particle size distribution (PSD), which is developed from airborne stratiform ice cloud in-situ measurements in the midlatitudes. Additionally, we used information from the Liu database of microwave single-scattering properties for three-bullet rosettes (LR3), sectored snowflakes (LSS), and dendrites (LDS) for ice habit characteristics (Liu, 2008; note that these are the same ice habits used in the K10 study). The PSD, ice habit, and radar backscatter cross-section information are used to convert the MMCR reflectivity measurements to ice water content (IWC). This IWC is then recombined with the PSD and ice habit information and the microwave optical properties at the specific MWR

frequencies, yielding the layer optical properties needed to simulate the passive MWR measurements (see Kulie et al., 2010 for further details). The SOI model uses these layer optical properties to calculate BTs at MWR frequencies. Finally, the emissivity of the snow surface is assumed to be 0.6, consistent with Yan et al. (2008) based on common snow surface conditions at Summit Station.

For an initial test of the model, we generate a synthetic 1 km thick ice cloud with a range in MMCR Z_{PATH} ($10^3 - 10^5 \text{ mm}^6 \text{ m}^{-2}$), inserted at 1-2 km above Summit in a temperature and water vapor profile typical for summer months at the site. We make no distinction between precipitating ice and cloud ice in these simulations. The MMCR derived Z_{PATH} is evenly distributed throughout the 1 km synthetic cloud. No liquid water cloud was included. The SOI modeled ice results with respect to the multi-frequency observations are shown in Fig. 4.8. The modeled LDS, LSS, and LR3 ice habits are over-plotted on the observations and show a similar slope for both the 150 versus 90 GHz and the 225 versus 90 GHz cases (panels a and b, respectively). Though the slope is similar, the equivalent Z_{PATH} values for the simulations show slightly larger BT differences than those seen in the measurements.

The small differences between the SOI model results and the observations with regard to equivalent Z_{PATH} may stem from the ice habit assumptions and/or the PSD used for these initial results. First of all, we can run SOI for only a single habit at a time and the model runs for these habits should bound the observations if assumptions made for the PSD are correct. The F07 parameterization may not adequately represent PSDs at Summit as this parameterization is derived from midlatitude flight campaign measurements of ice stratiform clouds and may very well be not at all applicable to the Arctic (Field et al.,

2005; 2007). Additionally, the F07, parameterization assumes a particle mass-size relationship appropriate for aggregated ice particles, while non-aggregated, pristine ice crystals are commonly observed at Summit (Shupe et al., 2013). Furthermore, the temperatures observed in the F07 parameterization are much higher than those at Summit and therefore the growth mechanisms of the ice hydrometeors in this PSD may be different than those in the Arctic. Future work will explore other PSDs and particle size relationships, which will aid our understanding of the ice habits at Summit. A recent installation of a Multi-Angle Snowflake Camera (MASC; Garrett et al., 2012) to ICECAPS will gather more information on ice habits.

4.6.5 Future work on the LWP and PWV estimate in the presence of ice

The above results are based on our first-order assessment of the ice-influenced LWP and PWV biases. Our current correction is defined in terms of the three-channel MWRRET retrieved LWP. As noted in Chapter 3, Sect. 3.1.1, this retrieval is used for this study as it is more sensitive to and has better precision for low LWPs. One possible BT correction can be estimated by examining specific “dry snow” cases (i.e., extremely low LWP and high Z_{PATH}), and by using the results from the present analysis. Additionally, we can compare these “dry snow” cases with independent LWP measurements using the mixed-phase cloud property retrieval algorithm (MIXCRA; Turner, 2007c). By using the TKC15 liquid water absorption model in MWRRET, which is more spectrally accurate at cloud liquid water temperatures below 0°C, we were able to recover many high Z_{PATH} cases that we found were previously discarded using the Liebe91 model. We believe that using TKC15 over the Liebe91 model reduced some of the small bias errors in our method and is a more appropriate choice for modeling cloud liquid water at Summit. Ultimately,

the goal would be to create a coincident, multi-instrument retrieval of the LWP, PWV, and IWP under all atmospheric conditions.

4.7 Summary

This study first examined cloud and precipitation statistics derived from the MMCR and partitioned the data with a specified LWP derived from the MWR. By limiting our study to low LWP (less than 40 g m^{-2}), we identify likely precipitating cases and then compared MWR BT observations against modeled BT contributions from gas and liquid components. This comparison enabled us to isolate a signature from the precipitating ice in the high-frequency MWR channels. The enhanced BT at the 90, 150, and 225 GHz is the ice signature for the majority of precipitating cases at Summit Station for the summer seasons of 2010 – 2013.

We identified a bias in the current MWRRET retrieved LWP and PWV caused by the ice signature and utilization of 23.84, 31.40, and 90 GHz channels as part of this study, and developed and applied a first-order correction (described in Sect. 4.5). The bias correction to the three-channel retrieval is not the focus of this study, but had to be addressed to quantify the ice signature in at microwave frequencies. Overall, the LWP and PWV bias due to ice occurs in a small fraction of the total data, and is relatively small in magnitude. For example, the high $Z_{\text{PATH}} (>10^4 \text{ mm}^6 \text{ m}^{-2})$ cases accounts for fewer than 2% of all available Summit MMCR data (4% if limited to JJA), and the LWP and PWV adjustments are -1.3 g m^{-2} and 0.044 cm , respectively, for Z_{PATH} of $10^4 \text{ mm}^6 \text{ m}^{-2}$. Thus the impact of the LWP bias on seasonal statistics will be minimal. However an accurate LWP retrieval in the presence of ice is important for precipitation specific cases. In addition, the

small number of high Z_{PATH} cases represents the heaviest snowfalls and thus are important for capturing the annual snowfall (Castellani et al., 2015).

The multi-frequency relationships in the high frequency MWR channels, illustrated in our results in Sect. 4.6.3, show a linear relationship between the 90 GHz channel versus both the 150 and 225 GHz channels and increasing Z_{PATH} values as a function of larger BT differences in each case. The initial SOI model runs for a synthetic ice cloud agree well with the observations, in both the relative slope and in Z_{PATH} magnitude. These results can also act as a starting point to a more rigorous LWP and PWV correction as described in Sect. 4.6.5. In future work, it may be possible to combine the MWRRET algorithm with data from the MMCR to create a robust joint retrieval of the LWP and the microwave ice signature. This will recover data at the large Z_{PATH} values and should lead to unbiased retrievals of LWP and PWV directly. Ultimately, a joint retrieval of LWP, PWV, and Ice Water Path (IWP) is desired.

To accurately retrieve IWP from the measured ice signature, we need accurate descriptions of the ice habit, surface temperature and emissivity, and ice PSDs more representative of conditions at Summit. For future work, we hope to employ a PSD with a better fit to the Summit conditions and eventually have ICECAPS instrumentation capable of measuring a PSD in-situ. The measured ice signature technique outlined in this work is a novel approach to better understand ice hydrometeors and could prove to be a powerful tool in future ground and remote sensing applications.

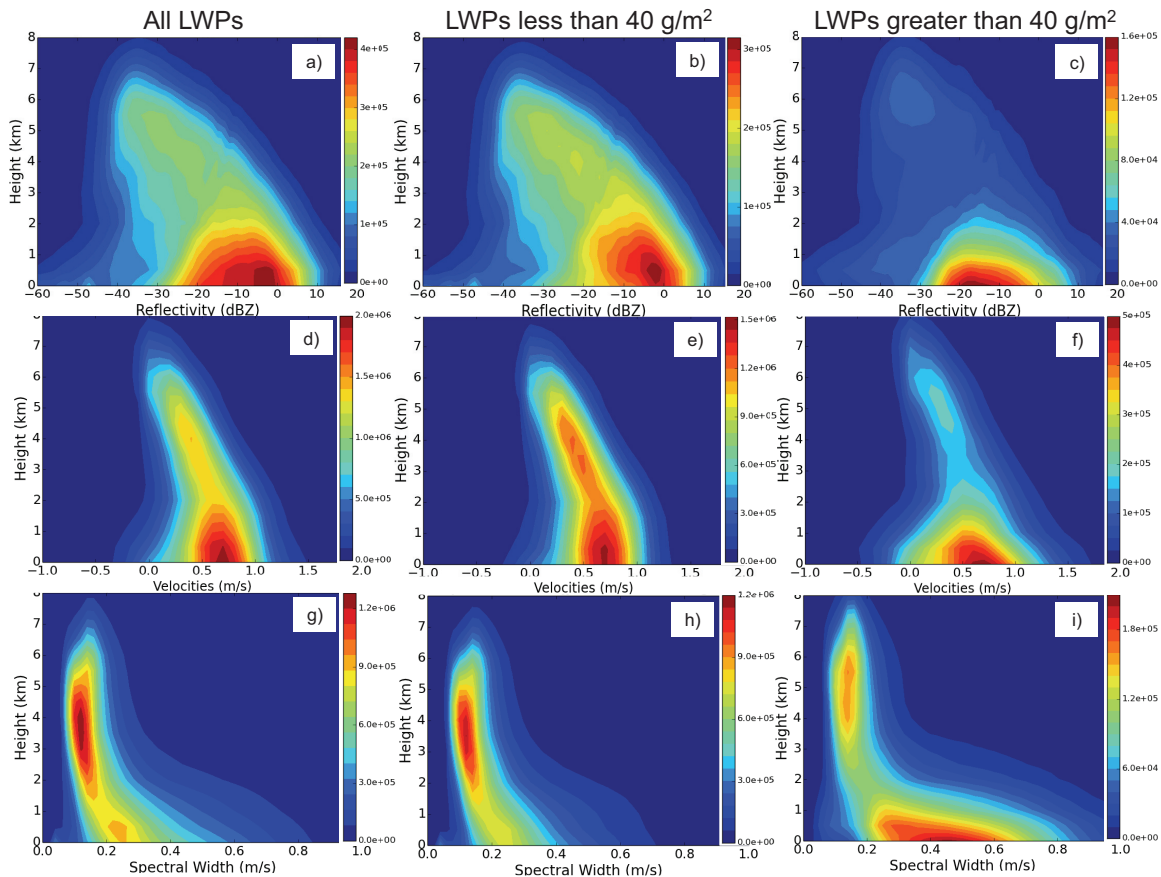


Figure 4.1 2DHs of MMCR reflectivity for summer (JJA) at Summit, Greenland from June 2010 through August 2013 with a sample resolution rate every 10 seconds. Panel a) shows JJA reflectivity for all measured LWPs while panel b) is filtered to reflectivities only when LWP is less than 40 g m^{-2} and panel c) is filtered for cases greater than 40 g m^{-2} . Additional 2DHs of MMCR Doppler velocity and spectral width for summer at Summit, Greenland for all LWPs (panels d and g), when LWP is less than 40 g m^{-2} (panels e and h), and when LWP is greater than 40 g m^{-2} (panels f and i), respectively. LWP less than 40 g m^{-2} accounted for $\sim 63\%$ of cases, while greater than 40 g m^{-2} is 22% of cases, and the remaining 15% is clear sky (as determined by the MMCR).

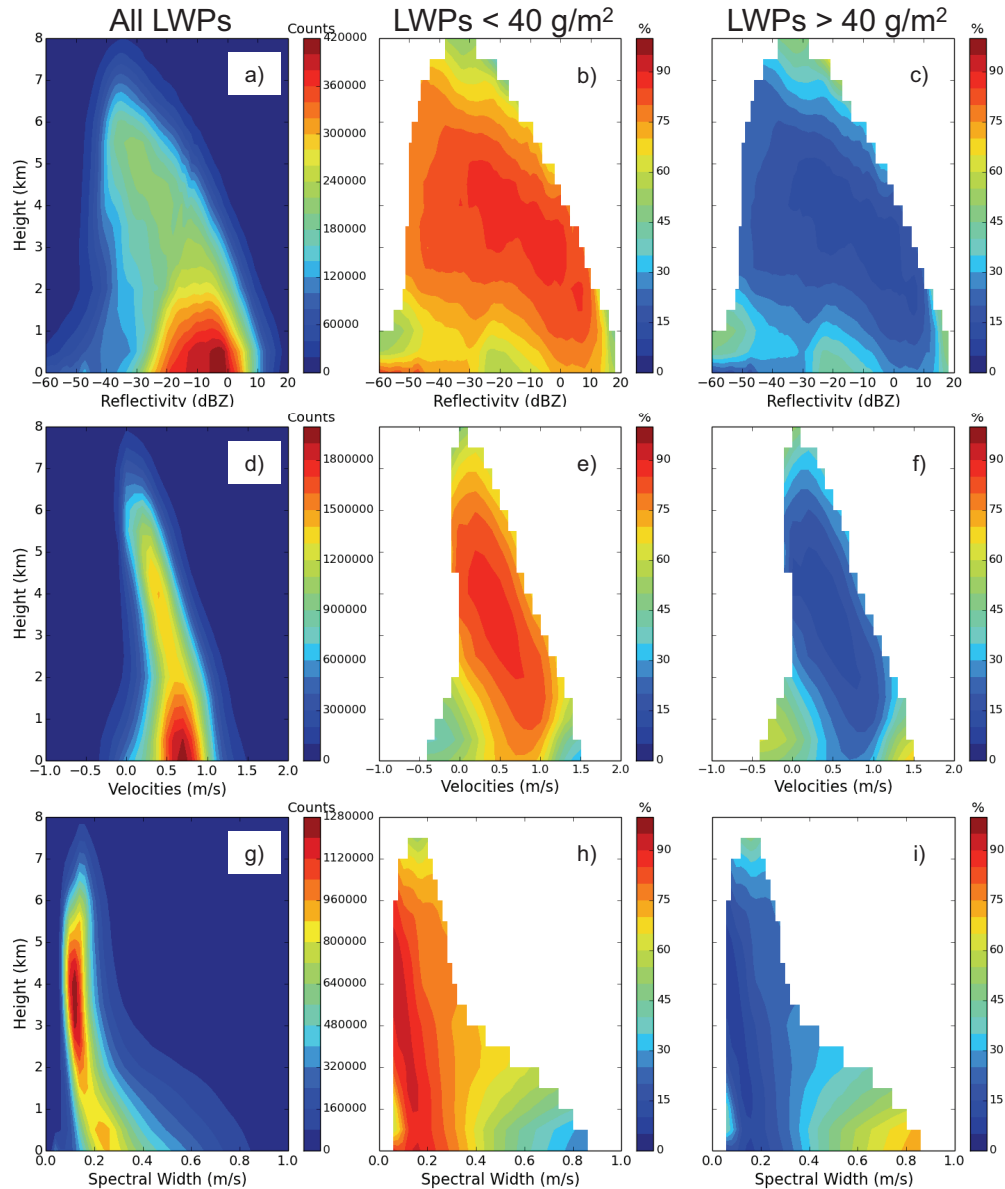


Figure 4.2 2DHs of MMCR reflectivity for summer (JJA) at Summit, Greenland from June 2010 through August 2013 with a sample resolution rate every 10 seconds. Panel a shows JJA reflectivity for all measured LWPs while panels b and c show the fraction of the total 2DH counts that occur below and above the 40 g m^{-2} LWP threshold, respectively. The filtered cases are shown in percentage of total counts to highlight the differences in the characteristics of the low and high LWP cases. Panels d, e, and f show the MMCR Doppler velocity 2DH, and the count fractions below and above the LWP threshold. And finally, panels g, h, and i show the MMCR spectral width 2DH and count fractions. LWP less than 40 g m^{-2} accounted for $\sim 63\%$ of cases, while greater than 40 g m^{-2} is 22% of cases, and the remaining 15% is clear sky (as determined by the MMCR).

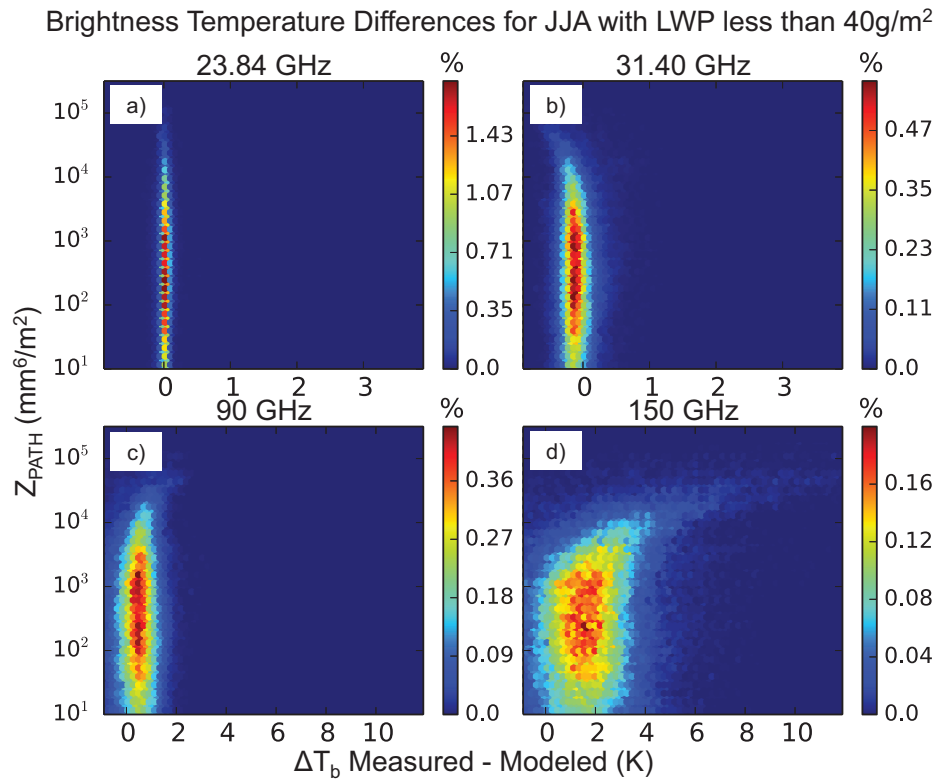


Figure 4.3 Brightness temperature differences between observations minus the modeled gas and liquid contributions in the 23.84, 31.40, 90, and 150 GHz channels as a function of Z_{PATH} for LWP less than 40g m^{-2} . The count histogram is binned logarithmically in Z_{PATH} and linearly in ΔT_b , shown as percentage of total observation count per bin. The 150 GHz channel shows an enhanced BT difference with respect to Z_{PATH} (panel d), while the 90 GHz has a slight enhanced BT, the 31 GHz exhibits a negative dependence, and the 23.84 GHz is channel neutral.

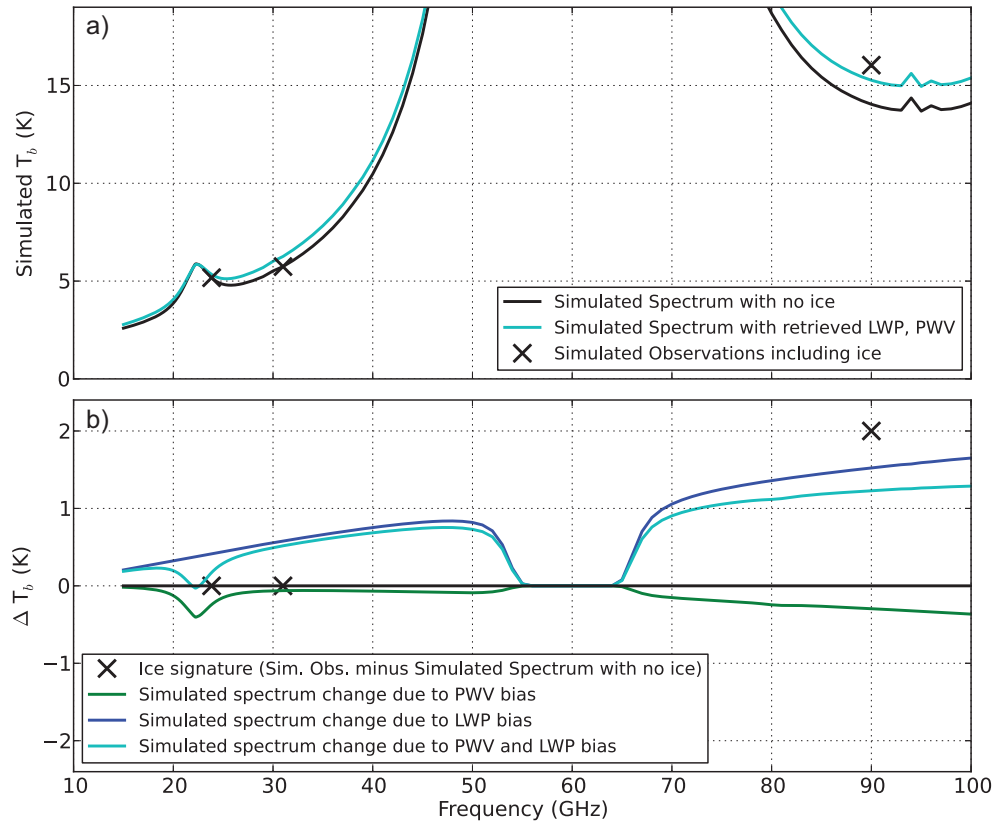


Figure 4.4 Panel a shows the simulated downwelling microwave radiance spectrum with no ice (black) and the simulated spectrum with the biased PWV and LWP obtained by the retrieval (cyan). Panel b shows the simulated data after subtracting the simulated spectrum with no ice. The effect of the biased LWP and PWV on the microwave spectrum are shown independently (blue and green lines, respectively) and combined (cyan line). The “X” marks show the simulated ice influence at 23.84, 31.40, and 90 GHz.

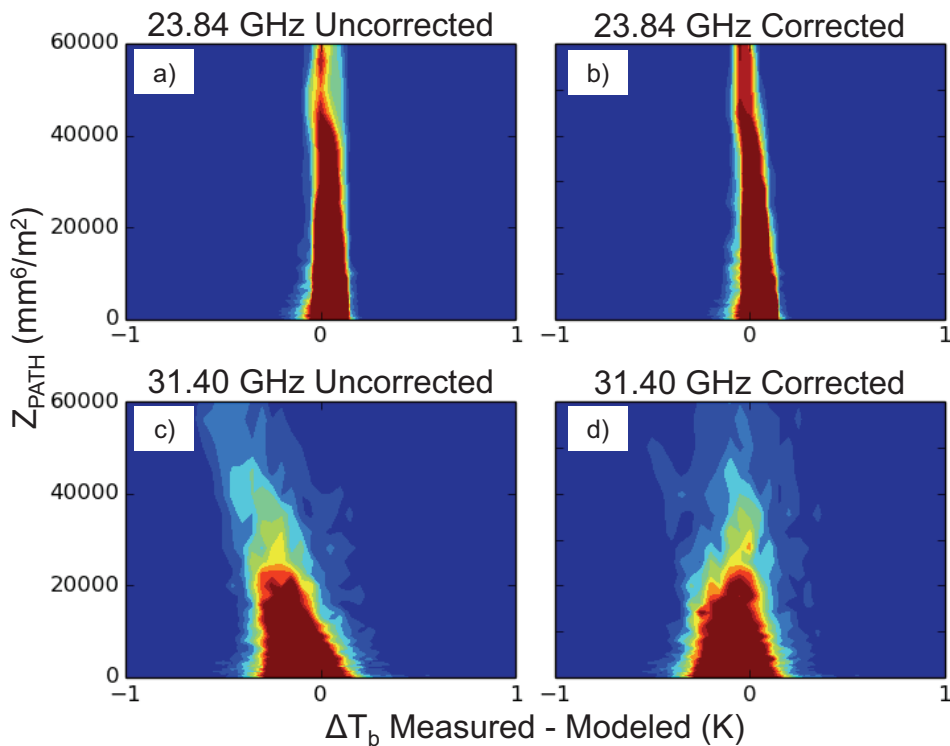


Figure 4.5 Histograms of the MMR Z_{PATH} and the difference between the measured and modeled BT at 23.84 and 31.40 GHz before and after the linear correction are shown above. Contour levels are linearly spaced, showing counts per factor of 100.05 in Z_{PATH} and per 0.05 K in BT difference. The y-axis is truncated to $6 \times 10^4 \text{ mm}^6 \text{ m}^{-2}$ Z_{PATH} to highlight the correction in the low ice optical depth cases. Red signifies 50 and higher counts and blue signifies fewer than 5 counts. Plots are linear in both axes. The uncorrected 31.40 GHz channel (panels c) has a negative bias as a function of the Z_{PATH} . The slope of the uncorrected 31.40 GHz (panel c) histogram yields the value of $\Delta T_b / \Delta Z_{\text{PATH}}$ used in the linear correction. For both low frequency channels, once the correction is applied, no dependence on Z_{PATH} is present (panels b and d).

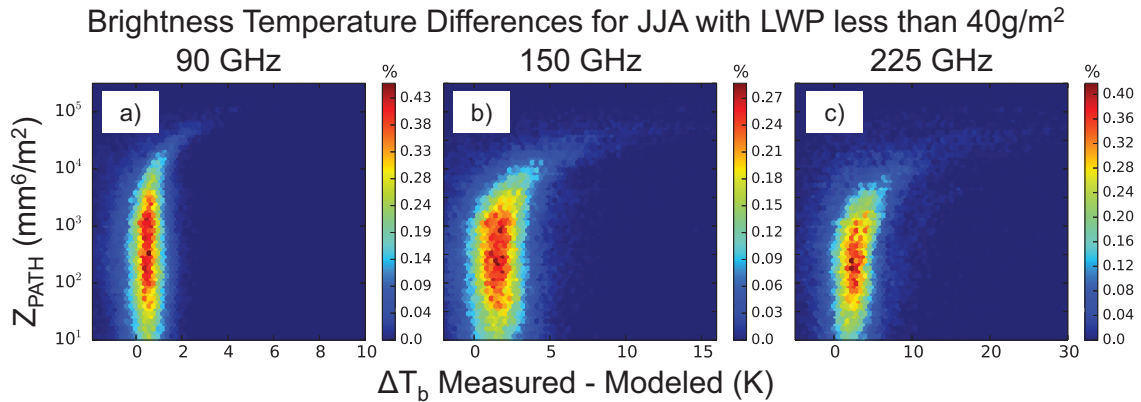


Figure 4.6 Brightness temperature differences between the HFMWR and the HFMWR-225 observations and the modeled gas and liquid contributions after implementing the LWP correction for ice for the 90, 150, and 225 GHz channels. The count histogram is binned logarithmically in Z_{PATH} and linearly in ΔT_b , shown as percentage of total observation count per bin (same as Figure 4.3). The high frequency channels show a dependence of the difference in brightness temperature and the Z_{PATH} from the MMCR – thus, indicating an increasing brightness temperature in these channels with increasing total ice amount in the column. Additionally, the sensitivity to the ice signature increases as a function of higher frequency. The Z_{PATH} value where the ice signature BT enhancement begins is lower in the 150 versus the 90 GHz channel (panels b and c, respectively) and lowest in the 225 GHz (panel c). We note that there is a clear sky bias in all three channels, but the magnitude of this bias is smaller than the radiometric uncertainty of the HFMWR observations. We are unable at this time to determine if this bias is due to calibration uncertainty in the radiometer or the result of forward model error.

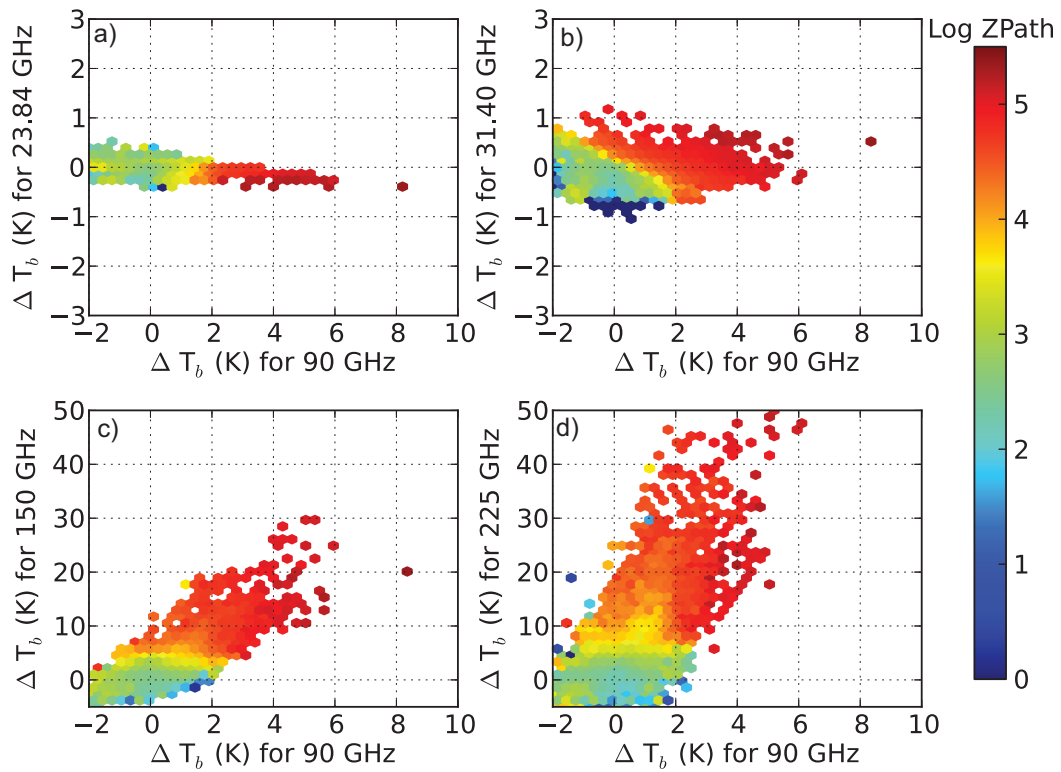
Multi-frequency Comparisons – JJA with LWP less than 40 g/m²

Figure 4.7 Multi-frequency plots of the BT difference in channels 23.84, 31.40, 150, and 225 GHz as compared to the 90 GHz channel. The binned values of BT difference are colored according to logarithm of the average Z_{PATH} values. In the top two panels, the lower frequency channels are plotted against 90 GHz (a and b) and in the bottom two panels, the 150 and 225 GHz are plotted against the 90 GHz (c and d).

Multi-frequency Comparisons with SOI Simulations –
JJA with LWP less than 40 g/m²

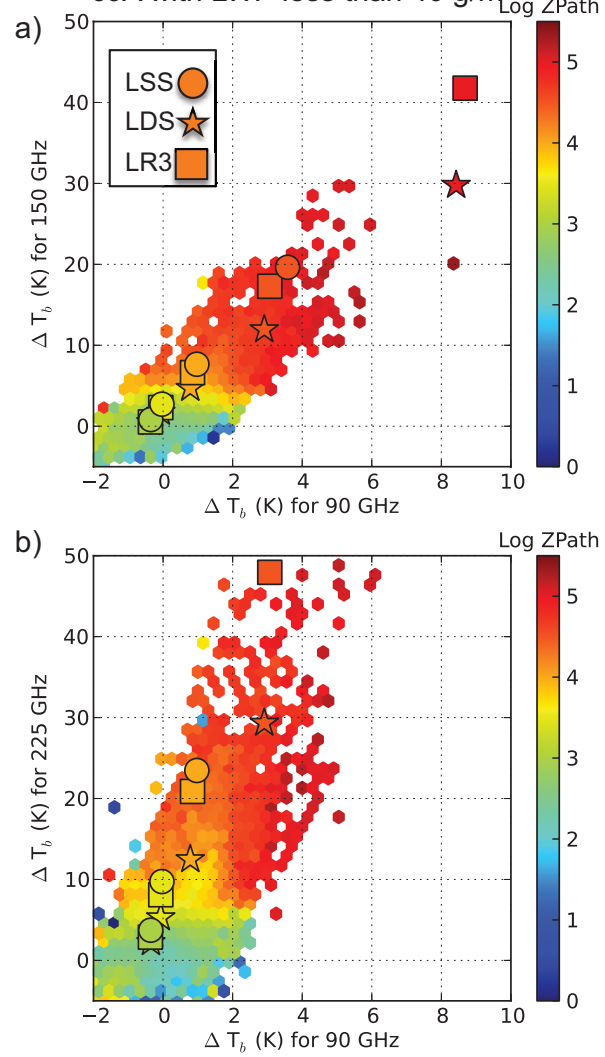


Figure 4.8 SOI simulated BT differences plotted on top of the observations for the 150 versus 90 GHz and 225 versus 90 GHz channels (panel a and b, respectively). In both examples, the slopes of the simulations agree well with the observations.

Chapter 5

5 Microwave Radiometer Snow Regime Classification Tool³

5.1 Introduction

A novel method for classifying Arctic precipitation using ground-based remote sensors is presented. Using differences in the spectral variation of microwave absorption and scattering properties of cloud liquid water and ice, this method can distinguish between different types of snowfall events depending on the presence or absence of condensed liquid water in the clouds that generate the precipitation. Microwave radiances have differing sensitivity as a function of frequency to different atmospheric components. For ground-based MWRs, the observed signals at all frequencies include contributions from gases like water vapor and oxygen as well as from clouds (when clouds exist in the field of view of the radiometer).

The emission from the gases is in the form of absorption lines, such as individual water vapor lines at 22.2 GHz and 183.3 GHz, or as a cluster of many absorption lines, such as for oxygen between 51.0 and 60.0 GHz. The spectral regions between these gaseous absorption features are referred to as “windows”, where the contribution from the gases is relatively small. Thus, radiometer channels in these spectral windows will have a larger radiance contribution from clouds than channels situated on gaseous absorption features. For example, in Fig. 5.1, simulations of the optical depth (OD) of the atmospheric components are shown as a function of microwave frequency. The 23.84

³ Portions of this chapter are in review in Pettersen et al. (2017) and are copyright of the European Geophysical Union.

GHz channel is in a WV absorption line and thus measures a higher OD from the WV contribution than the neighboring 31.40 GHz channel. The 31.40 GHz channel is not in an absorption band for either the WV (cyan line) or the dry gases (grey line) and is therefore considered a window channel. The 150 GHz MWR channel is also considered a window channel, as it is free of absorption/emission bands from gases, similar to the 31.40 GHz channel (see Fig. 5.1). Throughout this work, we designate the 150 GHz window channel as “HF” and the 31.40 GHz window channel as “LF”.

In contrast to gas absorption, condensed cloud liquid water (CLW) exhibits continuum absorption with much smaller spectral variation. When CLW is present in the column, all channels observe emission from the condensed water, increasing the observed BT. Figure 5.1, illustrates that the OD of the CLW grows larger as a function of higher MWR frequency and therefore the 150 GHz channel is more sensitive and measures about 10 times the OD from CLW as compared to the 31.40 GHz channel. When ice hydrometeors are present in the atmosphere, they will affect the observed downwelling radiance at the surface in two ways: emission of radiation from the ice hydrometeors themselves and scattering of the surface radiation back to the MWR. In the HF (150 GHz) MWR channel, the ice hydrometeors have a high single scatter albedo of about 0.9 (e.g. Liu, 2008), which suggests that scattered radiation the dominant effect. The extinction OD from frozen water, in the form of ice hydrometers, also has a broad continuum shape. We introduce a novel use of the ground-based MWRs to isolate IC snowfall from CLW containing snowfall by employing the ratios of the spectral response from the HF and LF window channels.

5.2 Spectral Response from LF and HF “window” channels

In earlier work by Kneifel et al., 2010 and Pettersen et al., 2016, it was observed that ice falling in the column scatters the upwelling radiation from the ground back to the MWRs and results in enhanced BTs in the HF MWR channels. Thus, while the LF (31.40 GHz) MWR is insensitive to the ice hydrometeors in the column (Johnson et al., 2012), the HF MWR channels observe an enhanced BT signature from ice. The enhanced BT is due to the differences in the size parameter, which is the ratio of the hydrometeor size with respect to the observed wavelength. We use ratios of the observed BTs from the HF and the LF window channel to classify the snowfall by events that are coincident with clouds containing CLW and those that are ice only. Kneifel et al. (2010) and Pettersen et al. (2016) used the MWR retrieved PWV and LWP values in a radiative transfer model to simulate the BT contributions of the gases and CLW. These contributions were subtracted from the measured BT to isolate the enhanced ice signal in the HF MWR channels. Pettersen et al. (2016) found that the MWR LWP retrievals often did not converge during snowfall events at Summit, or were biased high due to ice-enhanced BT in the HF MWR channels. Therefore, we do not use any retrievals or modeling of the CLW in this work. Figure 5.2, illustrates this ratio approach with three scenarios and the accompanying response from the MWR LF and HF channels.

5.2.1 MWR LF and HF response to clear-sky, CLW, and ice

In clear sky situations (Fig. 5.2, left), both the LF and HF MWR channels measure small and quickly varying BTs. The fast variations are due to measurement noise, which is uncorrelated in the two channels. Both radiometers are primarily measuring the cosmic microwave background radiation from space with small contributions from dry gases and

WV in the column. In the second example, there is a mixed-phase cloud with supercooled CLW overhead, and both the LF and HF MWR channels measure a higher BT signature and show similar patterns of amplitude as a function of time. This signature is due to the emission of the CLW as a function of frequency, depicted in Fig. 5.1. In the final scenario, we present observations from a fully-glaciated ice cloud and there is a markedly different response in the HF channel as compared to the LF: The LF MWR channel shows a similar pattern to that of clear sky as it is insensitive to the ice in the column. The HF channel, however, observes a large BT signature during the time that the ice cloud and precipitation is occurring. By using the differences in the ratios of the HF to LF MWR observations of each scenario, we can, with a high degree of confidence, classify the snow into categories: precipitation originating from a fully-glaciated ice cloud, i.e., “ice cloud (IC)” snow, precipitation originating from a mixed-phase cloud – snow that has some CLW layers present, i.e., “CLW containing” snow, and precipitation that we cannot distinguish accurately the cloud type, i.e., “Indeterminate snow.”

5.3 Application of classification tool to ICECAPS dataset

We apply the classification method to the entire 5-year dataset for the ICECAPS MWRs. We first identify the times of precipitation using the POSS power units (Ppu), as the POSS is the best indicator that ice hydrometeors reached the surface without evaporating (the POSS is located within a few meters of the surface and within 10 m of the MWRs; Shupe et al., 2013). However, the POSS data is susceptible to contamination from blowing snow events. We evaluated cases of blowing snow, confirmed by observer reports, wind speeds, and the MMCR spectral width, and determined that a threshold of 2 Ppu is appropriate to identify precipitation events while excluding false positives from blowing

snow. For all times when precipitation was identified, we use the available observations for the 31.40 and 150 GHz MWR channels from July 2010 through the end of 2015.

Since this study compares snowfall events that occur over a span of 5+ years, there is variance in the MWR BTs that depends on background temperature and WV profiles and the seasonal variation. To facilitate comparison of events occurring at different times of the year and with dissimilar atmospheric profiles, we use MonoRTM calculations (see Chapter 3, Sect. 3.2.1) to account for this variation. We use pressure, temperature, and relative humidity from the interpolated radiosonde data and the resulting MonoRTM calculations to obtain clear-sky BT values at the HATPRO and HFMWR frequencies. For altitudes above available radiosonde measurements, the U.S. Standard Atmosphere (McClatchy et al., 1972) is used up to 30 km above ground level. We then subtract the calculated clear-sky BTs from observations from the MWR. The resulting ΔBT values are the CLW and/or ice contributions as a function of frequency. Due to the high and dry location of Summit Station, the optical depths of the atmospheric components at the microwave window channels are very low. Thus, the different contributions to the microwave radiance are approximately additive, and we can employ this method with decent accuracy across the time range of the ICECAPS dataset. The ΔBT s are composited for all of the precipitation events and the results are shown in Fig. 5.3.

The ratios of the composited ΔBT s in the HF and LF channels determine if the snow event is a product of a fully-glaciated ice cloud, i.e., IC snow, or if there is one or more layers of supercooled CLW in the column, i.e., CLW snow. Figure 5.3 is annotated to illustrate the regions of the different snow types as determined by the MWR classification method. The IC snow cases are the group of points in the left lobe, where

there is a strong response in the HF and minimal signal in the LF channel. These IC snowfall events are depicted with the black arrow and are to the left of the purple, dashed line. This line is empirically determined by the HF to LF ratio response of the ice versus the CLW in the column and is used to separate the two regimes. For the cases where the snowfall is coincident with CLW in the atmosphere, the HF and LF MWR channels both measure a BT response and the slope is lower, resulting in the right lobe of points in Fig. 5.3. The CLW snowfall events are denoted with a blue arrow.

There are snowfall events, which are of indeterminate type, as shown in Fig. 5.3 in the outlined cyan box. The indeterminate region was calculated using multiple clear-sky days from a range of seasons and temperatures to look at the variance from computing the Δ BTs. The variation of this method may arise from environmental changes that occur between the 12-hourly radiosonde profiles. By using events categorized as clear sky from MMCR observations, we composited the HF and LF Δ BTs by season. Under clear-sky conditions, the Δ BTs maximum range for the MWR window channels was 0.5 K (0.5 K) and 2.5 K (4 K) for the LF and for the HF for September through May months (during June, July, and August; JJA). Snowfall events that have associated BTs that are less than 2.5 K (4 K for JJA) in the HF and 0.5 K in the LF MWR channels cannot be unambiguously assigned to either IC or CLW snow and these events are therefore classified as indeterminate. This occurs when the conditions do not produce a total column amount of ice or liquid that is large enough to produce a measureable signal over the clear-sky modeled “background”.

5.4 Summary

We introduced an MWR-based method for classifying the precipitation at Summit to discriminate snow events originating from fully-glaciated ice clouds (IC) from those associated with mixed-phase clouds (CLW). We are able to isolate IC snowfall from CLW snowfall by employing the ratios of the spectral response from the HF and LF MWR window channels. Key to this method is the HF (150 GHz) MWR channel, which is shown to be an important tool for ground-based classification of precipitation regimes over central GIS. We can now apply the MWR snow classification tool to concurrent observations from various instruments in the ICECAPS suite as well as available surface meteorological data and reanalysis products. This allows for better understanding of the different snow types through: characterizing the general cloud and precipitation properties, obtaining thermodynamic surface and profile information, and illustrating the large-scale surface and upper-level dynamic processes. Chapter 6 examines the coincident measurements and retrievals available at Summit Station, and explores the large-scale dynamics and implications for regional impacts over the central GIS.

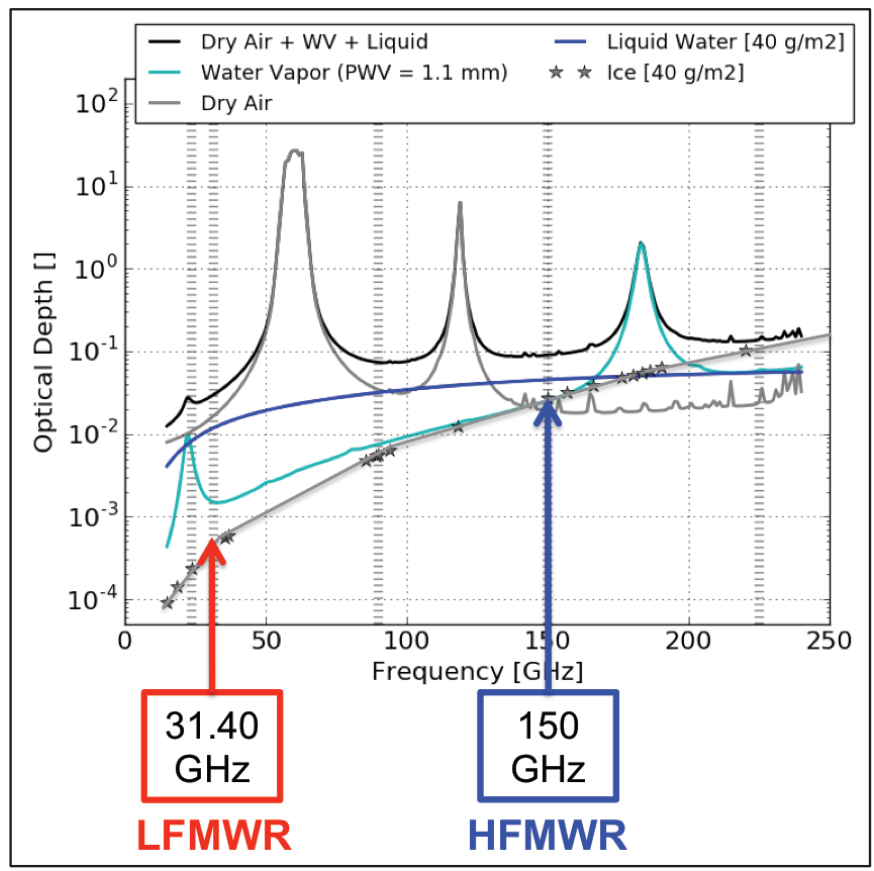


Figure 5.1 A representation of modeled extinction optical depth as a function of frequency for the atmospheric components under conditions relevant for Summit: both the liquid water path and ice water path are 40 g m^{-2} , and the WV and dry gas concentrations are from the Standard Subarctic Winter profile starting at 3 km. The red and blue arrows highlight the microwave channel observations used in the study (low and high frequencies, respectively). Note the different spectral slopes of the ice versus the liquid versus the WV contribution.

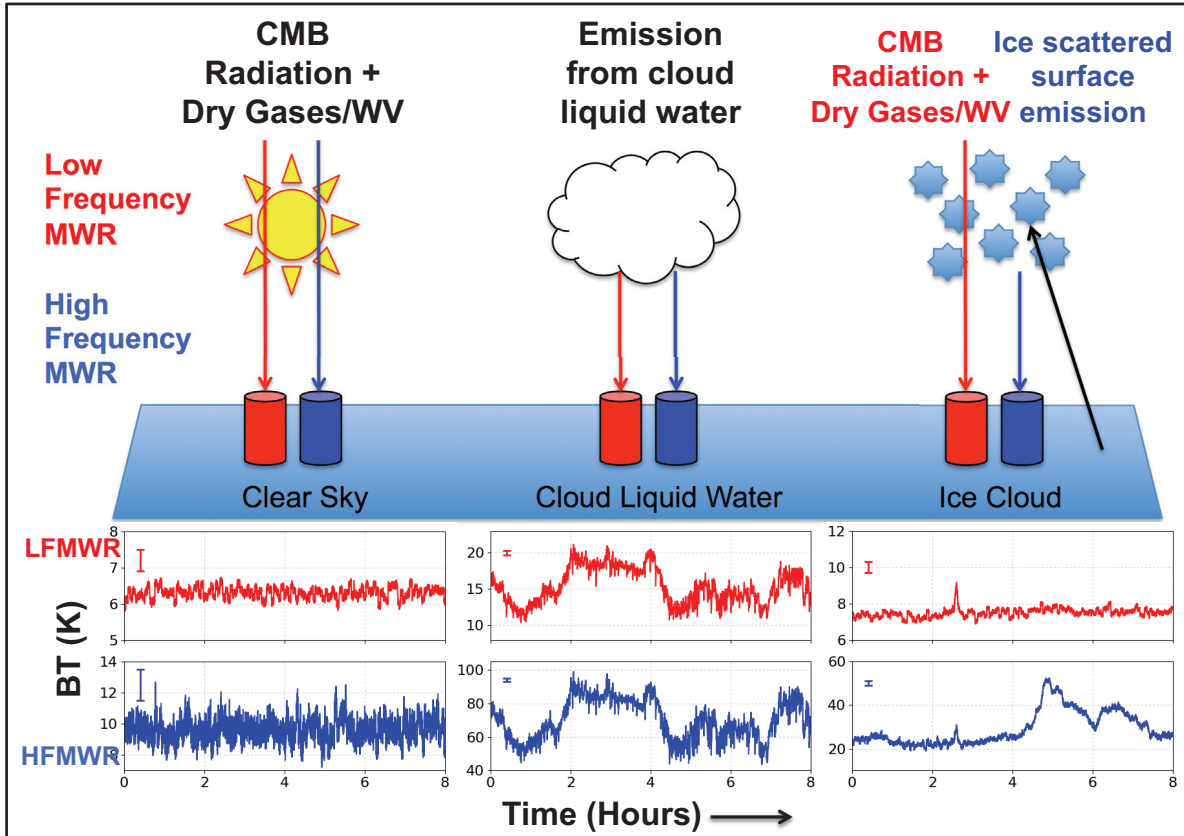


Figure 5.2 A schematic representation of the spectral response of the low (red) and high (blue) frequency microwave radiometers under conditions of clear sky (left), cloud liquid water in the column (middle), and precipitating ice cloud (right). Error bars denoting the MWR channel measurement precision is shown in the top left corner of each plot (0.3 K and 1.0 K for the low and high frequency channels, respectively).

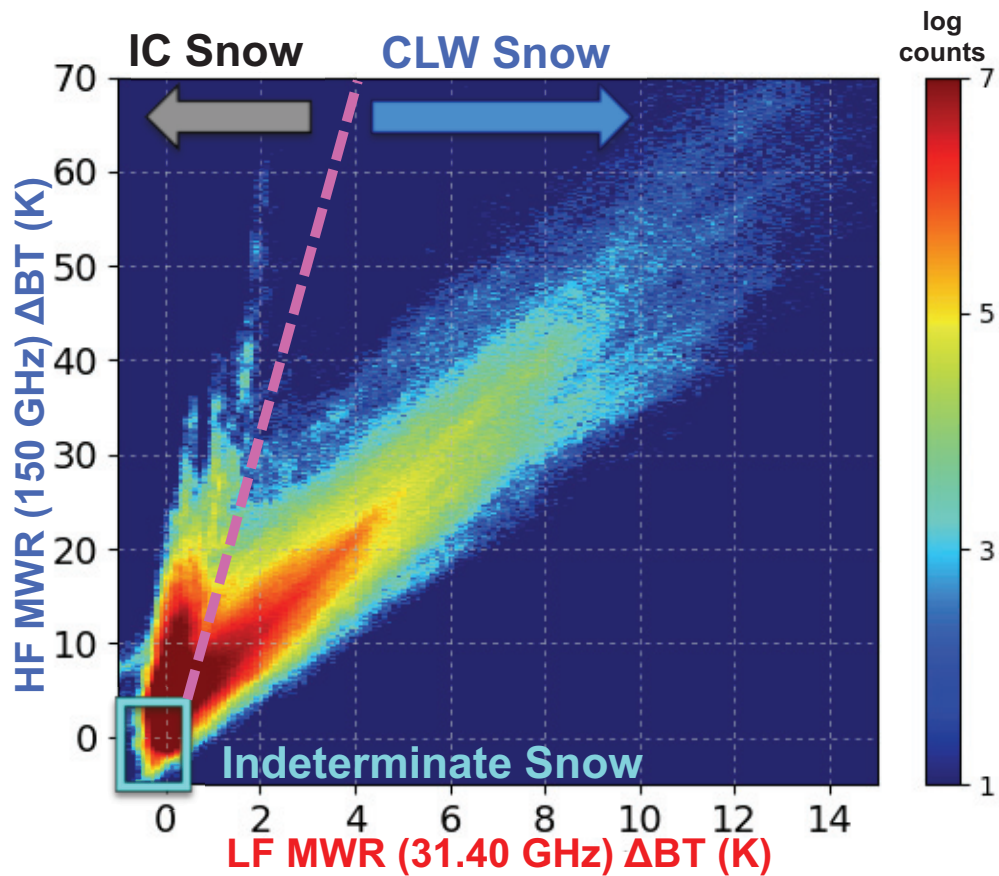


Figure 5.3 All available MWR data for 2010 – 2015 during precipitation (as determined by the POSS Ppu threshold). These values are delta BT where the clear sky forward model RT run is subtracted from the MWR observations. The arrow annotations show the regions of IC snow (to the left of the dashed line), snow with associated CLW in the column (to the right of the dashed line), and snow of indeterminate type (in the cyan outlined region). The indeterminate region is defined by the sample distribution in clear sky, and captures the residual variance due to uncertainties in the modeling of the gas absorption optical depth.

Chapter 6

6 Snow regimes inferred from 5 years of ICECAPS observations⁴

6.1 Introduction

Using the method for classifying Arctic precipitation presented in Chapter 5, we can distinguish between different types of snowfall events depending on the presence or absence of condensed liquid water in the clouds that generate the precipitation. The classification reveals two distinct, primary regimes of precipitation over the Greenland Ice Sheet (GIS): one originating from fully-glaciated ice clouds and the other from mixed-phase clouds. Five years of co-located, multi-instrument data from the Integrated Characterization of Energy, Clouds, Atmospheric state, and Precipitation at Summit (ICECAPS) are used to examine cloud and meteorological properties and patterns associated with each precipitation regime. The occurrence and accumulation of the precipitation regimes are identified and quantified. Cloud and precipitation observations from additional ICECAPS instruments illustrate distinct characteristics for each regime.

Additionally, reanalysis products and back-trajectory analysis show different synoptic-scale forcings associated with each regime. Precipitation over the central GIS exhibits unique microphysical characteristics due to the high surface elevations as well as connections to specific large-scale flow patterns. Snowfall originating from the ice clouds is coupled to deep, frontal cloud systems advecting up and over the southeast Greenland

⁴ Portions of this chapter are in review in Pettersen et al. (2017) and are copyright of the European Geophysical Union.

coast to the central GIS. These events appear to be associated with individual storm systems generated by low pressure over Baffin Bay and Greenland lee cyclogenesis. Snowfall originating from mixed-phase clouds is shallower and has characteristics typical of supercooled cloud liquid water layers, and slowly propagates from the south and southwest Greenland along a quiescent flow above the GIS.

6.2 Characterization of snow types as observed by ICECAPS

Figure 6.1 is similar to the data illustrated in Fig. 5.3 as it shows a two-dimensional histogram of the HF and LF MWR Δ BTs for all precipitation events from July 2010 through 2015, however divided into summer (MJJAS; Panel a) and winter (ONDJFMA; Panel b). Again, it is worth noting that the precipitation partitions into two lobes – the steep HF to LF ratio indicating the IC process snow, and the lower slope mixed-phase process CLW associated snow. The summers have many events in both snow types, while the IC snow dominates the winters. This section will use concurrent observations and retrieved properties from the POSS, MMCR, and IcePIC instruments to quantify and characterize events within each of the snow classifications.

6.2.1 Occurrence and Accumulation Statistics

Figure 6.2 depicts the POSS-determined occurrence (Panel a) and accumulation (Panel b) statistics throughout the year. Occurrence was estimated using the POSS power threshold detection of precipitation outlined in Chapter 5, Sect 5.1, and the associated accumulation was calculated using the Shephard and Joe (2008) algorithm for snow LWE in millimeters. All of the data are shown in percentages for all available coincident POSS and MWR observations from July 2010 through the end of 2015 (and accounting for any instrument down time in a given month). Overall, the trend of precipitation occurrence

and accumulation are similar, with slightly higher IC accumulation per event and lower indeterminate accumulation per event. By occurrence, the IC snow is 31.5 %, CLW is 48.5 %, and indeterminate is 20 % of the time, and by accumulation the IC snow contributes 35 %, CLW associated snow is about 51 %, and the indeterminate snow is 14 %. The indeterminate snow is a small fraction of the accumulation at Summit and we will therefore focus the remaining work on the IC and CLW snowfall events.

Similar to previous studies of precipitation at Summit (Castellani et al., 2015), we find that both the occurrence and accumulation of snow is higher in mid-summer through early autumn. The largest accumulated snowfall period is during July, August, and September comprising over 50 % of the cumulative snowfall annually, with each month contributing 15 % or more to the annual total. The peak month for snowfall accumulation is August, with ~22 %. CLW snowfall tends to increase starting in May and peaks in July for occurrence and accumulation, and falls off rapidly after September. The IC snowfall increases throughout the summer, peaks in September, and continues to have significant mass contributions in the late fall with ~8 % of total annual accumulation during October and November. Small accumulations of IC snowfall are seen throughout the winter and spring in larger amounts than the CLW snow, and account for the majority of the accumulation deposited at Summit Station outside the summer season. Figure 6.2, Panel c, shows the POSS LWE snow rate (mm hr^{-1}) as a function of snow classification by month in a box and whisker plot: means (horizontal line), 25th to 75th percentiles (box), and 5th to 95th percentiles (vertical line). In general, the 25th to 75th percentile precipitation rates for the IC and CLW snow overlap, however, for every month except June and May, the IC snow has a higher average and maximum values of POSS snow rates. The indeterminate

snow cases are largely associated with weaker precipitation rates, especially in the higher snowfall months of June through November. Overall, the majority of the accumulation deposited at Summit is from light precipitation events, with 75 % of the precipitation occurring from rates less than 0.2 mm hr^{-1} .

6.2.2 Relationship of PWV to snowfall types

Figure 6.3 illustrates the MWR retrieved values of PWV as a function of month in box and whisker plots for all available data. Periods with snowfall at Summit have higher coincident values of PWV as compared to the distribution for all times at Summit (see Fig. 6.3, Panel a). This indicates that the PWV is generally larger than the background state when there is precipitation at Summit, regardless of snow category. The PWV values peak in July/August for both all times and precipitating times and follow a general trend correlated to the surface temperatures.

In Panel b of Fig. 6.3, the monthly annual averages of the PWV are shown for each snow category as designated by the MWR snow classification tool. For the majority of the months, the IC and CLW containing snow have similar PWV values, while the indeterminate snow has a slightly lower associated PWV. However, for most months the 95th percentile of the PWVs for the CLW snowfall is larger, indicating that there are more extreme PWV values coincident with these events. Figure 6.3, Panel c, shows the snow rate determined by the POSS (mm hr^{-1}) scaled by the corresponding retrieved PWV (in mm), which yields an approximation of the conversion rate of PWV into precipitation. Again, the CLW and IC snow have similar values for a given month, which suggests that the CLW associated snow processes are not more or less efficient than the IC snow processes. Thus, the differences in accumulation observed for a given snowfall type, are

largely due to differences in the fractional occurrence frequency of the regime, not because of significant differences in the PWV. However, for all snowfall types, October through April is more efficient at turning available PWV into precipitation. From May through September, there is much more PWV in general – coinciding with the warmer temperatures – but less snow is deposited when scaled to the PWV. This annual pattern indicates that when PWV is available during the colder and drier months, it is capable of producing relatively more snowfall when compared to the warmer summer months.

6.2.3 Radar and ice particle observations

We use the MMCR reflectivity and mean Doppler velocity observations to derive features of the vertical structure of the cloud and precipitation for the IC and CLW snow categories. We also look at retrieved properties from the MMCR of LWE snow rate, Z_{PATH} (analogous to ice water path), and cloud geometric thickness (Z depth) and superimpose these on their associated ratios of the HF and LF MWR channel observations. Finally, we add some qualitative information from IcePIC photographs gathered by scientific personnel during distinct IC and CLW snow events. All of this remotely-sensed and in-situ information aids in building a more complete picture of each of the snow types and their defining characteristics.

Figure 6.4 illustrates vertical profile characteristics of the IC and CLW snow through MMCR reflectivities and mean Doppler velocities. All of the identified IC and CLW events are composited and corresponding MMCR properties are shown as two-dimensional histograms of the measurement as a function of height. The profiles of reflectivity for the IC precipitation cases are very deep, often 5 km or more, and have a narrow range of reflectivities for a given height, with peak reflectivity of ~ 15 dBZ. Panel c

shows the Doppler velocities for the IC snow and again has a narrow profile, which indicates that there is ice falling and growing throughout the column as the velocities get larger closer to the ground. The reflectivity and Doppler velocity profiles for the IC snow events illustrate classic indicators of ice hydrometeor growth from the top of a cloud to the ground (Pruppacher and Klett, 2012).

Figure 6.4, Panel b and d show the respective two-dimensional histograms for CLW snow events. The CLW snow is associated with shallower clouds, often below 3 km, and a broader range of reflectivities, especially in the upper region of the clouds (between 1.5 to 3 km), with a similar reflectivity maximum of ~ 15 dBZ. The broader distribution of reflectivity may be due to the pulsed nature of the mixed-phase clouds, as ice growth co-varies with in-cloud dynamics driven by the radiative cooling from the CLW droplets at the top of the cloud. Additionally, the CLW cases coincide with broader and weaker Doppler velocities in the lowest 2 km as compared to the IC cases. This feature could be caused by CLW indirectly as efficient cloud top cooling from the CLW droplets drives turbulent vertical motions throughout the cloud. The weaker mean Doppler velocities may also be due to the ice habit associated with the CLW snow, i.e., particles with larger surface area such as dendrites have slower fall speeds. These characteristics observed by the MMCR for the CLW cases are consistent with features seen with shallow mixed-phase stratocumulus (Shupe et al., 2008; Verlinde et al., 2007).

We calculated three retrieved parameters from the MMCR to better understand the physical properties of the IC and CLW snow events. We use the MMCR Ze to snow rate calculations outlined in Chapter 3, Sect. 3.1.2 to get a LWE mass value (these values differ from the POSS snow rate, as we use a different Ze to snow rate relationship appropriate for

the wavelength of the MMCR; Matrosov, 2007). The Z_{PATH} is a useful alternative for ice water path (IWP) but does not use conversions that are sensitive to particle size distribution and ice habit (Pettersen et al., 2016; Kulie et al., 2010). Finally, we calculate the depth of the cloud profile as a geometric thickness (ΔZ), from the MMCR. All of the retrievals are used to differentiate characteristics of the IC from the CLW snow.

Figure 6.5 shows the HF and LF MWR ΔBT s as two-dimensional histograms as a function of season (summer and winter), similar to Fig. 6.1. However, instead of binning the histogram by counts, the color scales are the mean values of the MMCR properties associated with the ΔBT ratios. Panels a, b, and c, depict the retrieved values for the summer season: LWE snow rate (mm hr^{-1}), Z_{PATH} ($\text{mm}^6 \text{ m}^{-2}$), and geometric cloud thickness (km), respectively; while Panels d, e, and f are the corresponding winter values. The MMCR snow rate for both the summer and winter is noticeably higher during the IC snow events, which is consistent with the monthly POSS-derived LWE snow rates (see Fig. 6.2, Panel c). The Z_{PATH} , which is log-binned, is consistently an order of magnitude higher during the IC snowfall versus the CLW in both the summer and winter. The clouds tend to be geometrically thicker during the IC events while the CLW cases are geometrically thinner.

In general, the retrieved properties obtained from the MMCR yield consistent conclusions as the MMCR reflectivity and Doppler velocity observations: The IC snow events are associated with deep systems with ice falling from the very top of the cloud and growing throughout the column. Although they are less common, the strongest IC snow events have higher potential mass deposition as evidenced by the correlated high snow rate and Z_{PATH} values. The CLW cases tend to be shallower with evidence of supercooled

CLW at the top of the cloud, have lower Z_{PATH} , and slightly less deposition per event, though they occur more frequently.

We looked at IcePIC photos during identified IC and CLW snowfall cases. Local scientific personnel gathered ice hydrometeors sporadically to provide qualitative evidence of differences in ice habit. Some example IcePIC photos for specific events from each category of snowfall are highlighted in Fig. 6.6. For all the cases that were unambiguously correlated with an IC snow event, the ice habits observed are mostly bullets, bullet rosettes (of many number branches), and some columns and small plates (Fig. 6.6, left). This provides additional evidence that the IC snow events have ice originating at the top of the cloud growing throughout the column, as these habits are indicative of very cold and pristine conditions devoid of CLW (Korolev et al., 1999). The IcePIC photos taken during CLW snow events yielded mostly dendrites and sectorized plates with occasional small amount of riming, which is consistent with ice falling through CLW layers and warmer temperatures (Fig. 6.6, right). It is worth noting that variability in the ice habit and the particle size distribution (PSD) of the snowfall does impact radar reflectivity to snowfall relationships. Studies show that different PSD and ice habit can impact the calculated snow rate from reflectivity for both the POSS and MMCR frequencies (Liu, 2008; Dolan and Rutledge, 2009; Kulie and Bennartz, 2009). Though we do have some evidence of differing ice habits for the IC and CLW precipitation, we do not have any PSD information and cannot adjust the radar to snow rate based on the snow category. Therefore we are using a generalized, average relationship for all snow categories to acquire snow rate and accumulation information from both the POSS and MMCR.

6.3 Source air mass characteristics and dynamics associated with snow types

In this section we explore the origins of the air masses and their associated dynamics for both IC and CLW snow events. First, the dynamics can help explain why half the precipitation events are associated with mixed-phase clouds with layer(s) of supercooled CLW, while another 35 % are coupled to deep, fully-glaciated ice clouds. We find that there are distinct differences in the air mass behaviors for either type: The IC snow events propagate quickly over the southeast region of the ice sheet, have very deep layers of WV, and are likely advected over the GIS through large-scale vertical motion associated with the regional meteorology and topography, but may have less small-scale vertical motion (turbulence). The CLW events advect slowly across the southwest and southern portions of the GIS, tend to be shallow, and follow a quiescent flow to Summit. The CLW cases have calmer large-scale motion of the air mass, but much more small-scale turbulence driven by the CLW itself, which is consistent with characteristics of persistent Arctic mixed-phase clouds (Shupe et al., 2008; Morrison et al., 2012). Secondly, by understanding how the precipitation gets to Summit through the large-scale dynamics, we explain what is occurring regionally and, therefore gain broader knowledge of how the point observations at Summit Station apply to the central GIS.

6.3.1 Surface winds at Summit

The location of Summit Station is nearly at the top of the GIS (indicated with purple circle) and is both far from the ocean (400 km from the east and west coastlines and over 1000 km from the southwest and southeast). Therefore, understanding from where the air masses originate helps in illuminating how the precipitation arrives at Summit. We first look at the 10-meter surface winds (NOAA Global Monitoring Division) coinciding

with the IC and CLW snow events. Figure 6.7, Panel a, shows the wind speeds and directions for all dates and times from mid 2010 through 2015 for Summit. In general, precipitation occurs at Summit when the surface winds originate from south (though north winds do occur, they rarely bring precipitation) and these winds are often stronger than the mean winds (Fig. 6.7, Panels b and c).

By examining the coincident IC snowfall surface wind speeds and wind directions (Fig. 6.7, Panel b), we see that there is a preference of these events to originate from the southeast direction, however there is a distributed mode to the south and southwest as well. The IC snow event winds are much stronger than the mean state winds for all times at Summit, with most cases having winds stronger than 9 m s^{-1} . This is interesting as the majority of snow accumulation in Greenland is along the southeast coastal mountain range, and the ocean to the immediate southeast is a region with one of the highest occurrence snowfall locations in the Northern Hemisphere (Hanna et al., 2006; Kulie et al., 2016). However, much of this snowfall does not make it up and over the steep orography along the southeast coast of Greenland to the central GIS (Hanna et al., 2006). The direction and strength of the surface winds associated with the IC snowfall indicate that strong dynamics may be able to advect WV and precipitation-rich air masses from the southeast coastal region atop the central GIS.

When considering the mixed-phase CLW containing snowfall cases, the winds are predominately coming from the west-southwest to south-southwest directions (Fig. 6.7, Panel c). Recent studies of long-lived mixed-phase clouds at Summit show that they originate equivalently from the west, south, and east (Edwards-Opperman et al., submitted), however many of these clouds are either not precipitating or are precipitating

below the POSS detection threshold (outlined in Chapter 5, Sect. 5.1), and therefore only a subset are included in this work. Though there is a broader range of surface winds coincident with the CLW snowfall cases, the majority are coming from a different direction when compared to the IC snow, with 70 % originating from the west to the south of Summit Station (though there is a small amount originating from the southeast). These winds are not as strong as the wind speeds seen with the IC snow cases, but they are faster than the average winds seen for all times at Summit. This is consistent with previous studies, which showed that most clouds (of which the majority are mixed-phase and contain layer(s) of CLW) and precipitation occur under winds with southern and south-westerly flow (Shupe et al., 2013; Castellani et al., 2015). The surface winds indicate that these air masses are traveling slowly up the comparatively gentle slope southwest of Summit.

6.3.2 Regional meteorological conditions for snow type

In addition to the local meteorological conditions at Summit, we examined the regional surface patterns and large-scale dynamics associated with each snowfall regime using the ERA Interim Reanalysis. In general, it has been shown that precipitation over the central GIS is associated with moisture coming from the south via onshore and upslope flow (Bromwich et al., 1998; Hanna et al., 2006; Schuenemann and Cassano, 2009). We use the mean and climatological anomalies of sea level pressures and surface (10 meter) winds, as well as the 500 mb geopotential heights and upper-level winds to infer how the precipitating air masses get to Summit and what processes may glaciate the clouds as opposed to sustain layer(s) of CLW. Previous sections of this study included all identified IC and CLW snowfall events, regardless of their duration. However, since the ERA

Interim Reanalysis product has a four times daily resolution (at 00, 06, 12, and 18 UTC) we wanted to include only those events long enough to say with confidence that they occurred for most of an hour and at a time near the reanalysis product. We filtered the snow cases and used events that were duration of minimum of 45 minutes of an hour and within 2 hours of an ERA Reanalysis time step. We did not allow for more than one value in the same day unless 12 hours or longer apart to avoid one storm biasing the results. This method was purposefully conservative and yielded 90 IC and 84 CLW snowfall cases. The majority of the IC snow cases are from August through November, and all of the CLW snow cases are in May through September. To calculate the anomalies we used the 38-year dataset of surface and pressure level values and averaged these into monthly means for each longitude and latitude used in our study. Anomalies were then calculated by subtracting these historical monthly means from specific cases of identified IC or CLW snowfall.

We first look at the mean sea level pressure (SLP) patterns in the region around Greenland for the composited IC snow events. Figure 6.8, Panel a, shows an extremely deep low-pressure feature (SLP < 1000 hPa) wrapping around the horn of southern Greenland. This cyclonic feature has accompanying strong winds that originate from northern Canada and circulate counter clockwise, eventually towards the southeast coast of Greenland, with surface winds at Summit from the southeast. The SLP and wind anomalies for the IC snow cases are shown in Fig. 6.8, Panel c. There is a negative SLP anomaly coincident with the location of the center of the cyclone, and an anomalously high SLP anti-cyclonic feature to the east of Greenland. Previous work on synoptic forcing of precipitation over the GIS by Schuenemann et al. (2009) showed a similar pattern of

coupled low/high SLP anomalies generated precipitation both over Greenland and over the central GIS. The cyclone feature near the horn of Greenland is potentially a product of lee cyclogenesis, as it forms in the lee of the topographic ridge along the southern tip of Greenland (Rogers, 2004; Schuenemann and Cassano, 2009). Greenland lee cyclogenesis is also found to correlate with precipitation over the GIS, though most strongly in the southern region (Bromwich et al., 1998; Schuenemann and Cassano, 2009; Schuenemann et al., 2009).

In addition to the surface products, we examine the 500 mb geopotential height and wind patterns, both the means and the anomalies (see Fig. 6.9). For the IC snow events, the mean geopotential heights show a strong trough and ridge feature centered along the long axis of Greenland. The upper-level mean winds follow this height structure and show advection from the southeast coast to Summit Station. Just to the east of the trough is an area of upper-level divergence that creates strong vertical ascent throughout the column (Holton, 2004). This is located over a region of the North Atlantic Ocean with very high occurrence of snowfall and accumulation along the Greenland coast (Bromwich et al., 1998; Hanna et al., 2006; Kulie et al., 2016). Together, these features indicate that large-scale lifting likely pulls precipitation and WV from low in the troposphere up into the column and the upper-level winds then push this deep precipitation over the steep topography and onto the central GIS. Figure 6.9, Panel c, show the 500 mb geopotential height and wind anomalies for the IC snow events. Similar to the anomalies in the SLP analysis, the IC snow events have a dipole structure centered over Greenland, with lower than average heights to the west and a much higher than average ridge feature to the east. The upper-level wind anomalies are originating from the southeast and are strong

compared to the mean state winds. The dynamics implied by the 500 mb mean geopotential heights and anomalies support the deep, characteristic ice clouds observed by the MMCR at Summit. Additionally, according to the reanalysis temperature and relative humidity profile, the column is saturated with respect to ice up to 300 mb where the temperatures are below -40 C for the entire area over the central GIS. This indicates that ice is forming at the top of these clouds, thus adding to the evidence that they are fully-glaciated systems. Once ice has formed at the top of the cloud it will start to descend, and in a WV rich environment it will grow and eventually precipitate out to the surface, suggesting that these systems are snowing across the southeast central GIS as they move quickly towards Summit.

The regional mean SLPs and winds for the CLW snow cases are depicted in Fig. 6.8, Panel b, and show a relatively uniform pressure pattern over Greenland. The surface winds show weaker flow from the south approaching the Greenland coastline with stronger winds from the southwest at Summit Station. The SLP anomalies for the CLW snow cases are much weaker than those seen in the IC cases (Fig. 6.8, Panel d). In general, there is a broad, weak anti-cyclonic anomaly over most of the GIS and to the south and southeast, with a weak cyclonic anomaly near the United Kingdom. The wind anomalies show more moisture is coming from the south and southwest when compared to the mean state, which is consistent with studies of precipitation over the GIS (Bromwich et al., 1998; Hanna et al., 2006). The SLP anomalies shown in Fig. 6.8, Panel d, are consistent with calm conditions and weak forcing of vertical motions as there is a broad high SLP anomaly over most of the GIS. These features are favorable for Arctic mixed-phase clouds (Morrison et al., 2012; Shupe et al., 2006) and therefore consistent with the CLW snowfall cases.

The 500 mb mean geopotential heights and winds for the CLW snowfall events show a very different picture from that of the IC snow: the mean geopotential height is fairly uniform across Greenland and the upper-level winds are calm and flowing over the GIS from the south-southwest. This indicates a weak, quiescent flow that is slowly traversing up and across the GIS from the southern and south-western coasts. As stated previously, Arctic mixed-phase clouds are resilient in weakly-forced conditions such as those illustrated in Fig. 6.9, Panel b, for the CLW snow events (Morrison et al., 2012). Since the CLW snow is connected to these longer lived and slower mixed-phase cloud systems, they are likely to periodically snow over the GIS on their way to Summit. Figure 6.9, Panel d, shows the 500 mb geopotential height and wind anomalies for the CLW snow events. The CLW snow cases show that the mostly flat 500 mb mean geopotential heights across Greenland are, on average, anomalously high over a spatially extensive region, and even though the upper-level mean winds are fairly weak, they are anomalously strong compared to the background conditions (Fig. 6.9, Panel d). This is consistent with studies that have shown that higher than average 500 mb geopotential heights over Greenland are coupled to precipitation over the central GIS (Hanna et al., 2016).

6.3.3 Back-trajectories for each snow type

Using data from the NCAR/NCEP reanalysis project and the NOAA HYSPLIT modeling tool, we construct 36-hour back-trajectories for the IC and CLW events. We present results from back-trajectories of air masses at 3 km above Summit Station – although we looked at other heights, 3 km seemed to be the best compromise to capture motions associated with each precipitation classification (top of the CLW and middle of the IC snow cases) while minimizing localized artifacts from the GIS topography. Figure

6.10 shows the spatial movement and vertical motions (mean and standard deviation) for IC cases (left, top and bottom) and CLW (right). The backtrajectory above ground level (AGL) values represent the altitude above the model terrain (or ocean) height respective to the path of each trajectory. The IC snow events are mostly originating from over the North Atlantic Ocean, these air masses are moving very quickly over the GIS (with respect to the 36-hour reanalysis period), and these events are lifted a total of 5 km on average (from a mean of 1 km AGL over the ocean surface, to 3 km AGL over Summit) by the strong vertical motions off the coast of Greenland. For the CLW snowfall cases (Fig. 6.10, right), the back-trajectories originate to the south and southwest of Summit, these air masses are moving slower than the IC events, and the mean vertical motion is only slightly upwards, though the variance is larger with some air masses descending. In general, the HYSPLIT modeled back-trajectories confirm the dynamics that were inferred from the SLP and geopotential height maps, as well as the ICECAPS observations of cloud and precipitation properties for each snow regime.

6.4 Summary

Observations from ICECAPS instruments demonstrate that the CLW snow is the dominant regime of precipitation with 51 % accumulation, almost all of which occurs in the summer months. The IC snow, however, is a large component of the accumulation at Summit – accounting for about 35 % of the total. The IC snow is the main source of accumulation during the non-summer months and is capable of producing relatively more accumulation with less available PWV. IC snow events have higher than average winds, predominately from the southeast, indicating that the events are likely coming over the steepest part of the Greenland coast. The CLW snow events have moderate winds from

the south and southwest, traversing up a gentler slope to Summit. The coincident MMCR observations for the IC snow cases show deep clouds indicative of ice growth throughout the column: the reflectivity and Doppler velocity distributions are both relatively narrow and the mean values increase as the hydrometeors reach the surface. Contrarily, MMCR observations for the CLW snow cases illustrate shallower clouds with broader ranges of reflectivities and more frequent occurrence of lower Doppler velocities, indicating layers of supercooled CLW droplets, the shallow dynamics associated with these clouds, and different ice particle distributions.

The large-scale dynamics, as indicated by the ERA Interim reanalysis, find distinct synoptic regimes associated with IC and CLW snow that are consistent with the observations from the instruments at Summit. The mean SLP map for the IC snow cases shows a strong low to the east of the southern tip of Greenland implying that these topographical lee cyclones are a key mechanism for air mass advection during these precipitation events (Rogers, 2004; Schuenemann et al., 2009). Additionally, the SLP anomaly map for the IC snow shows two low pressure anomalies – one in Baffin Bay and one wrapping around the horn of Greenland – implying that these storms are potentially bifurcated by the Greenland ridge topography, a storm pattern which is correlated with precipitation atop the GIS (Schuenemann and Cassano, 2009; Schuenemann et al., 2009). The mean SLP map for the CLW snow cases show a calm, flat high pressure across most of Greenland. The SLP anomalies are slightly positive over much of Greenland and there is a large anticyclone feature from the southwest to the northeast over the North Atlantic correlated with the CLW snow. The mean high SLP over Greenland promotes calm advection of mixed-phase clouds from the southwest and south up and over the central

GIS, which is consistent with previous observations (Appenzeller et al., 1998; Bromwich et al., 1999).

The 500 mb geopotential mean heights and anomalies and HYSPLIT back-trajectories illustrate how precipitation is formed and how it may be affecting the central GIS. The mean 500 mb geopotential height maps show how the IC and CLW snow regimes are advected to Summit and are consistent with the observations from the ICECAPS instruments. The mean 500 mb geopotential heights for the IC snow have a large, coupled trough and ridge feature centered over Greenland. To the east of the trough is an area of upper-level divergence, which induces large vertical updrafts throughout the column. The IC snow is characterized by deep cloud systems where the ice can grow and precipitate out over the GIS. The evidence of upper-level divergence implies that large-scale upward motion creates low-pressure systems, which transport water vapor upwards along the south-eastern slope of Greenland. These deep systems are then advected over the central GIS and likely also precipitate over the southeast central GIS as they travel towards Summit. The mean 500 mb geopotential heights associated with the CLW snow cases are very flat and show a region of quiescent upper-level flow. The CLW snow is associated with shallower systems with evidence of supercooled CLW at the top of the clouds. The quiescent flow, slowly advecting up and over the south and southwest Greenland topography is an environment favorable for long-lived mixed-phase clouds (Morrison et al., 2012, Shupe et al., 2006). The vertical motions and relative speed of the air masses for each snow regime from the HYSPLIT back-trajectory analyses illustrate similar mechanisms.

These dynamics have implications for both how precipitation is formed and how it arrives at Summit. The patterns of the SLP and 500 mb geopotential height anomalies for the IC and CLW are very different. Features seen in the anomaly maps may relate to climate indices – particularly the North Atlantic Oscillation (NAO) and the Greenland Blocking Index (GBI), as both have been linked to precipitation over the central GIS (Bromwich et al., 1999; Hanna et al., 2016). The conclusions from this study warrant further work investigating the dynamics of the IC and CLW snow cases by season and comparing the resulting SLP and 500 mb geopotential height anomalies to the seasonal NAO and GBI.

This study illustrates that there are two distinctive regimes of snowfall at Summit Station: snow from ice clouds and snow from mixed-phase clouds. The two identified snow classifications have dissimilar dynamics governing how the precipitation reaches the central GIS and may therefore have very different responses to a changing climate. Historically, it is found that changes in atmospheric circulations and storm systems are the dominant force for changes in precipitation over the GIS and not increases in temperature (Kapsner et al., 1995). The distinct large-scale dynamical drivers for each snowfall type suggest potential differences in response to climate change. If these precipitation regimes respond in different ways to rapid climate change in the Arctic, the magnitude of the mass balance of the central GIS over time is highly uncertain.

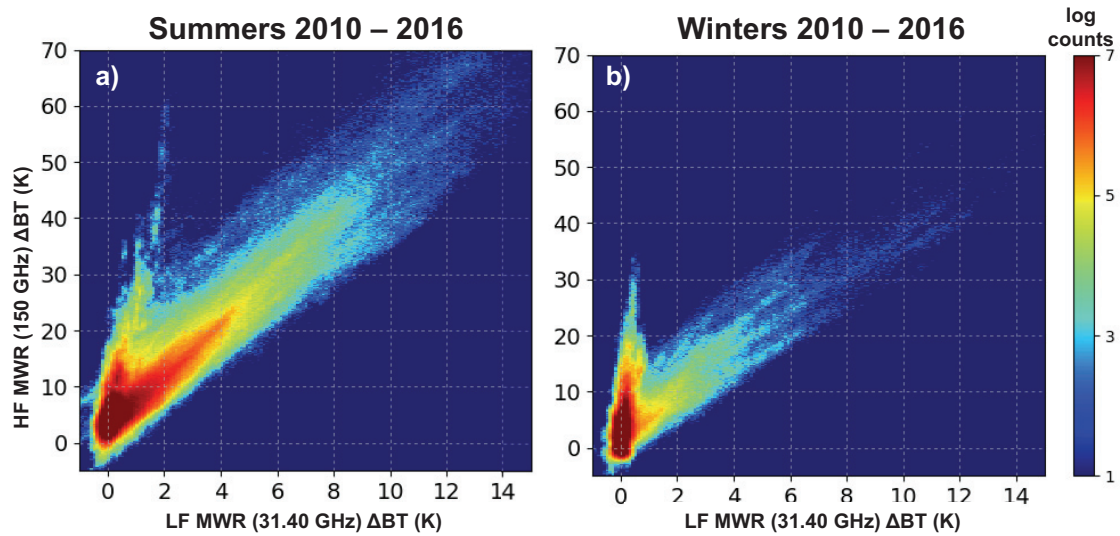


Figure 6.1 These are the MWR observations minus the clear-sky contribution, for all available data during precipitation events from 2010 to 2015. The summer precipitation is shown in Panel a (left; summer is defined as May through September), and the winter precipitation is shown in Panel b (right; winter is defined as October through April). The summer MWR observations indicate both IC and CLW snow events occur through the season, though more CLW events. The winter season tends to strongly favor the IC snow events.

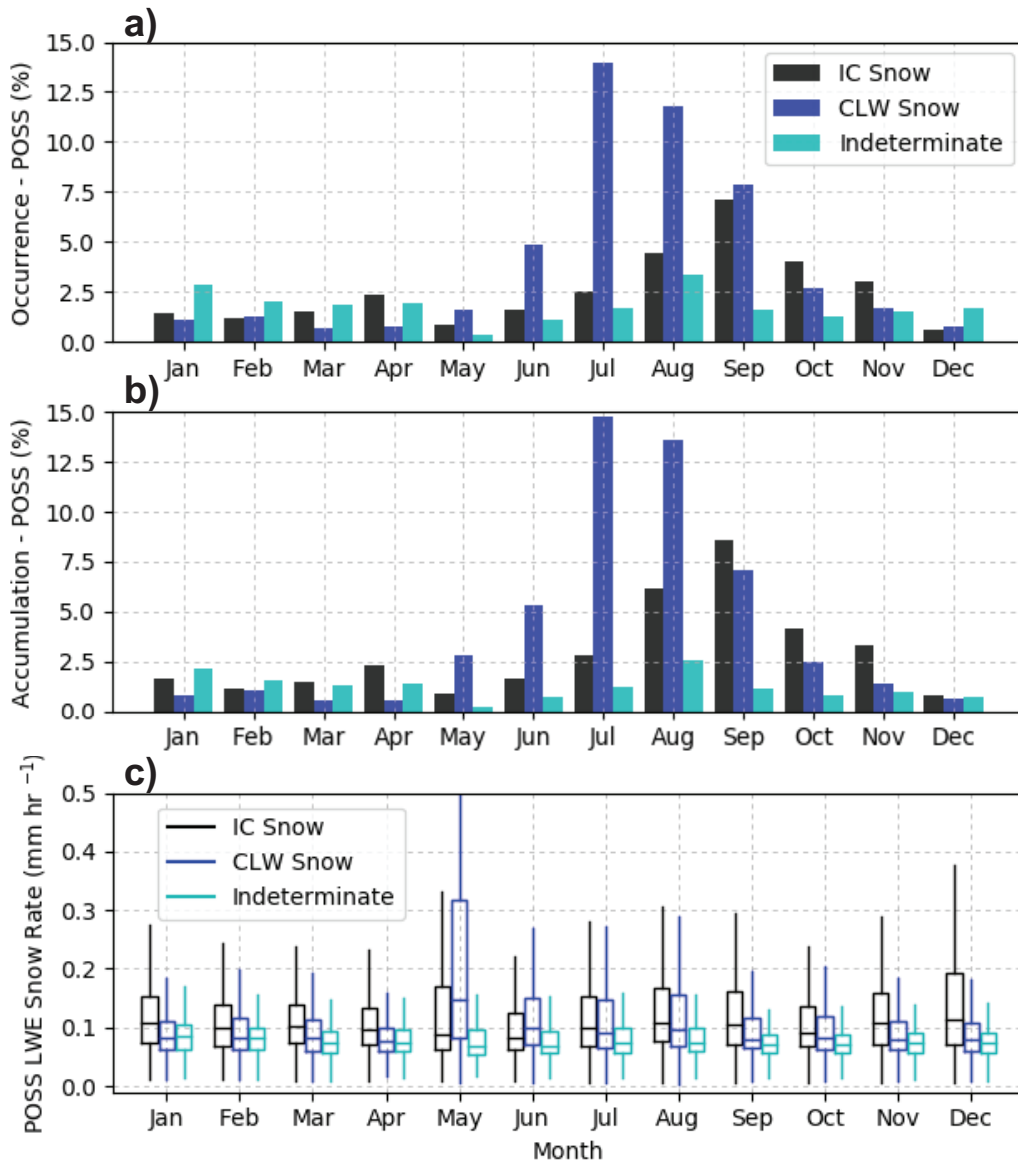


Figure 6.2 The POSS statistics from 2010 – 2015 for the MWR filtered precipitation events. Panel a (top) shows snow amounts by Occurrence (POSS) for all data: IC – 30.5 %, CLW – 48.5 %, and Indeterminate – 21 %. Panel b (bottom) shows snow amounts by Accumulation (POSS) for all data: IC – 35 %, CLW – 51 %, and Indeterminate – 14 %. The POSS snowfall amounts and snow rates were calculated using the Joe and Sheppard (2008) Z to S relationship. (Note: Panel c shows very high values for the CLW snow in May, which is due to an unusually large storm dominating the results).

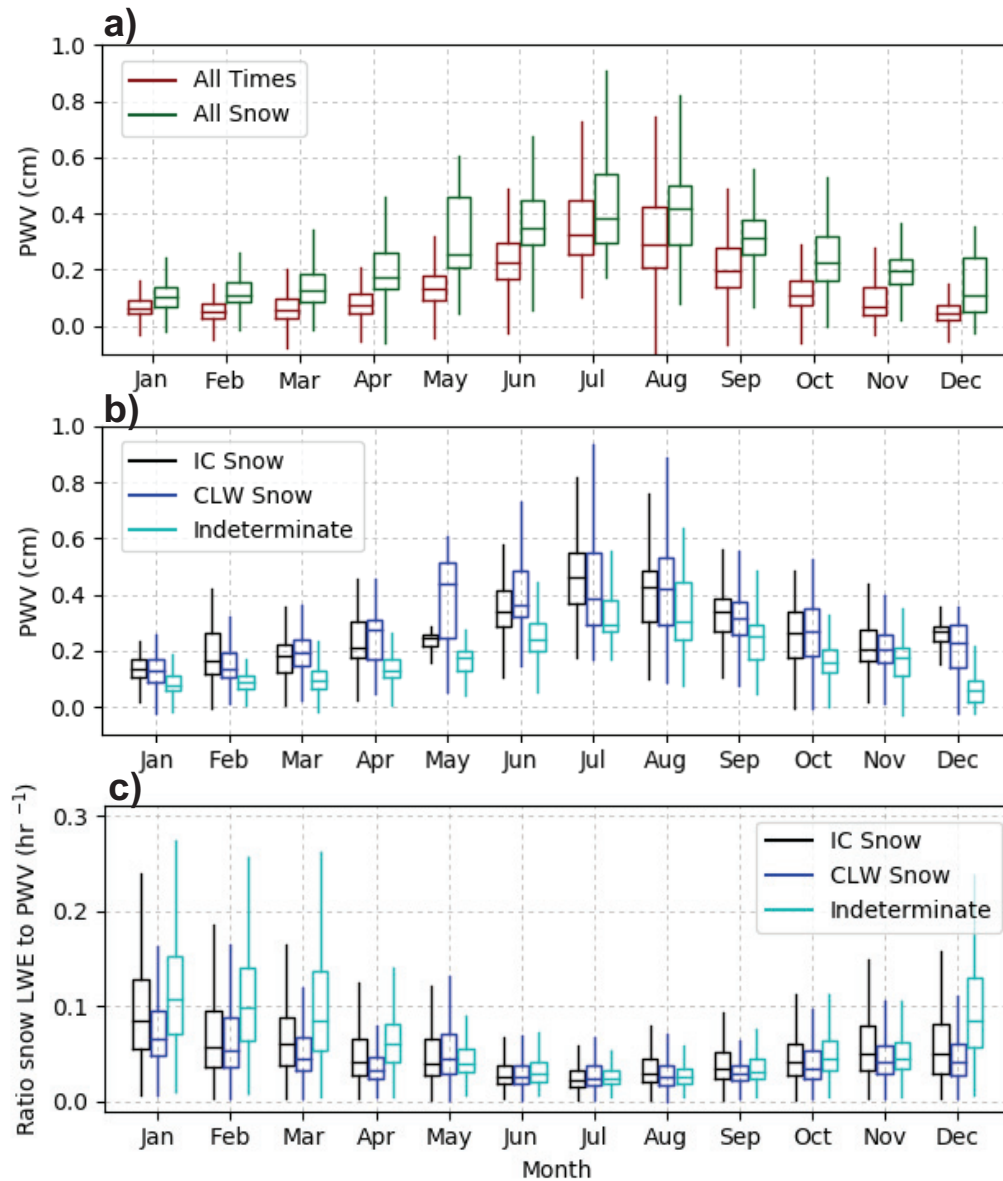


Figure 6.3 Panel a shows the average annual PWV as a function of the month for MWR data from 2010–2015. The PWV values during snowfall events, regardless of type, are higher than that of the PWV averages during all times (precipitation and non-precipitating). Panel b shows the average PWV associated with each MWR-determined type of snowfall. Panel c shows the ratio of the average snow rate measured by the POSS in LWE mm hr^{-1} to the associated PWV in mm, thus giving a rate of how efficiently the PWV converts to precipitation for each month and snow type.

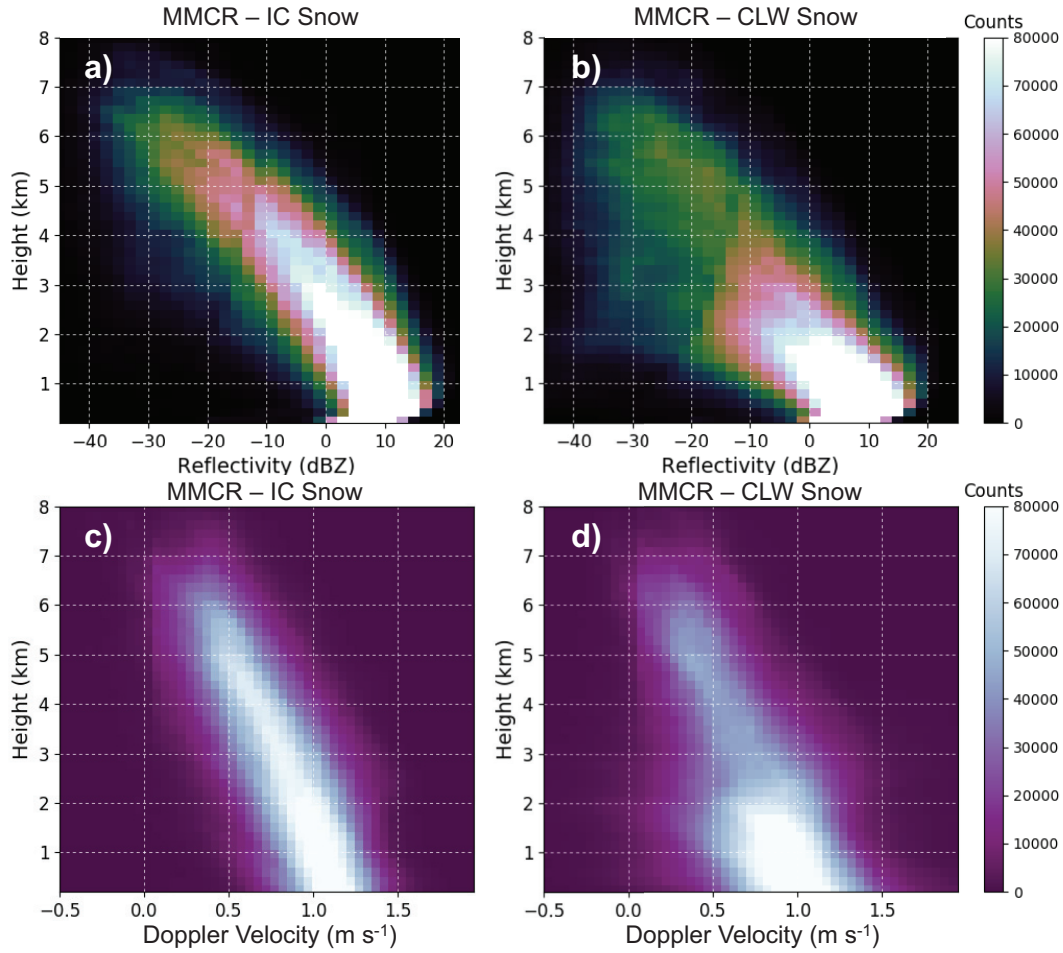


Figure 6.4 Composite two-dimensional histograms of MMCR properties for each MWR-determined snow type are shown. Each histogram uses a linear color scale with a maximum value of 80,000 counts. Panels a (top, left) and b (top, right) show the MMCR reflectivity as a function of height for all the IC and CLW snow cases, respectively. Panels c (bottom, left) and d (bottom, right) show the MMCR Doppler velocities as a function of height. These composites of the IC and CLW precipitation highlight different characteristics between the two snow modes.

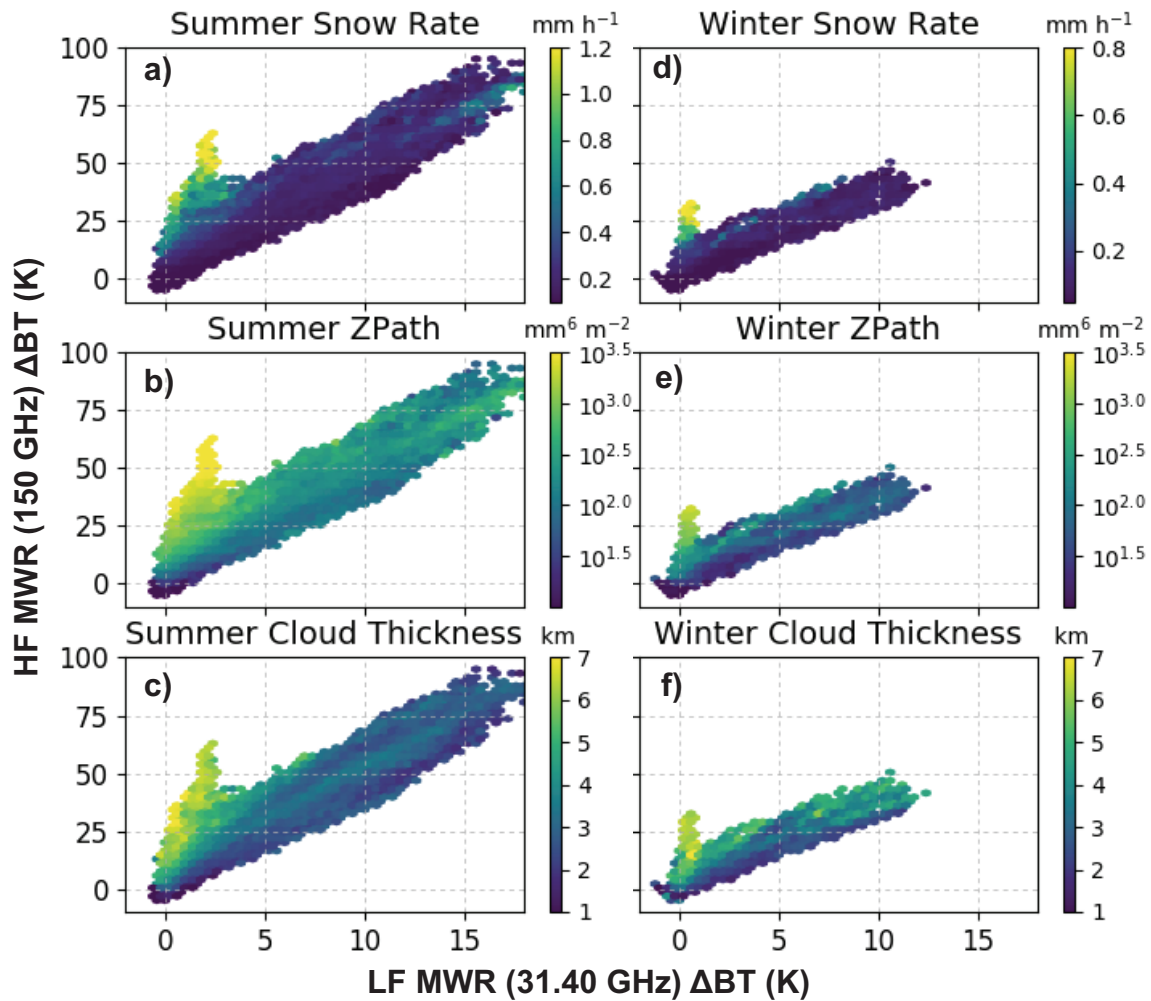


Figure 6.5 Values of MMCR calculated snow rate, Z_{PATH} , and cloud thickness are calculated for all the precipitation events and plotted with the associated HF and LF MWR observations. The top Panels (a, b, and c) depict these characteristics for the summer months and the bottom Panels (d, e, and f) for the winter months. Regardless of season, the IC precipitation has a higher instantaneous snow rate than the CLW cases. Additionally, the Z_{PATH} values for the IC snow cases are much higher than the CLW cases. And the IC snow tends to be associated with deeper clouds than the CLW snow.

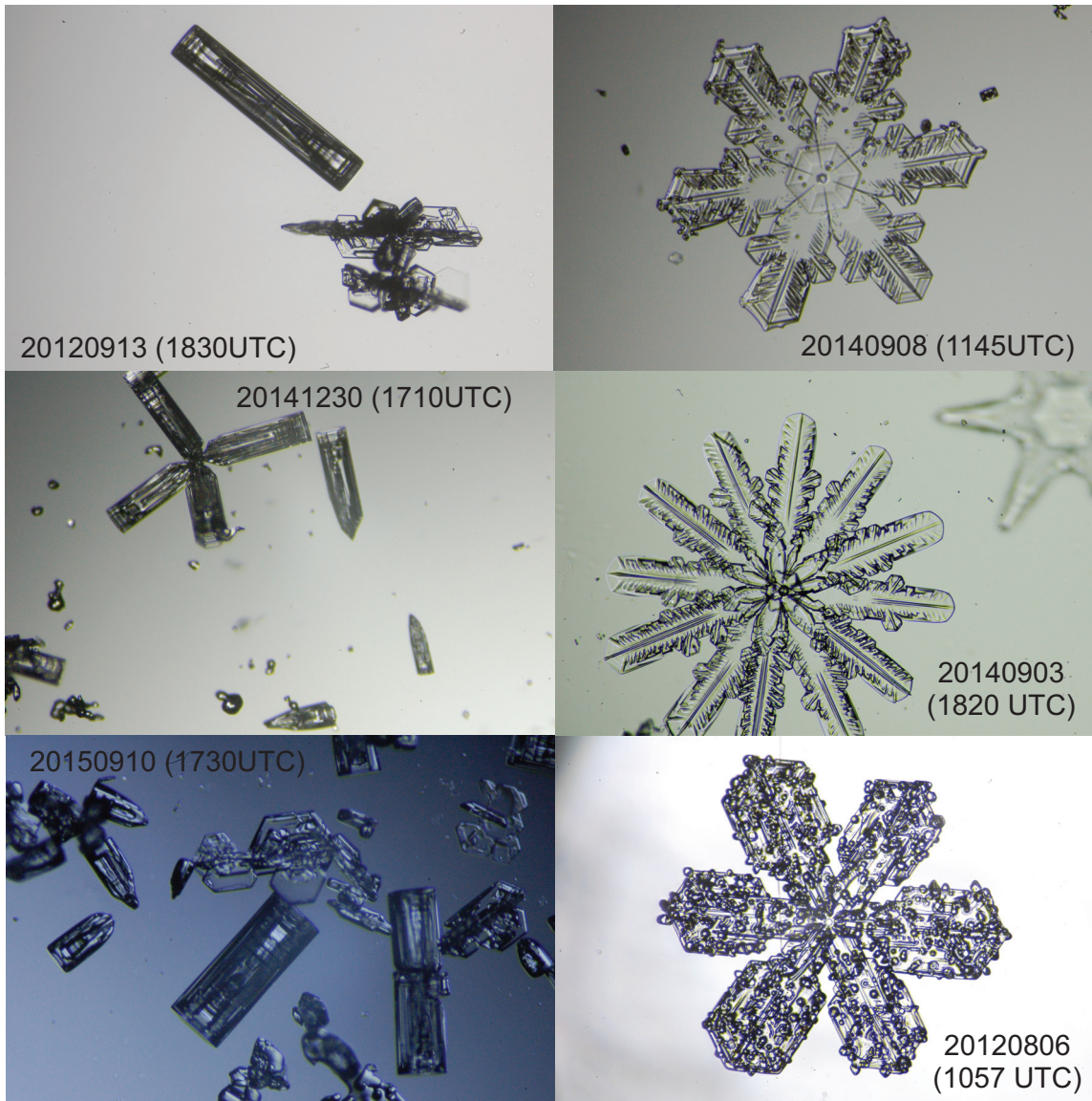


Figure 6.6 Examples images from the IcePIC camera of ice cloud (IC) originating snow events (left) and for mixed-phase CLW containing snow events (right).

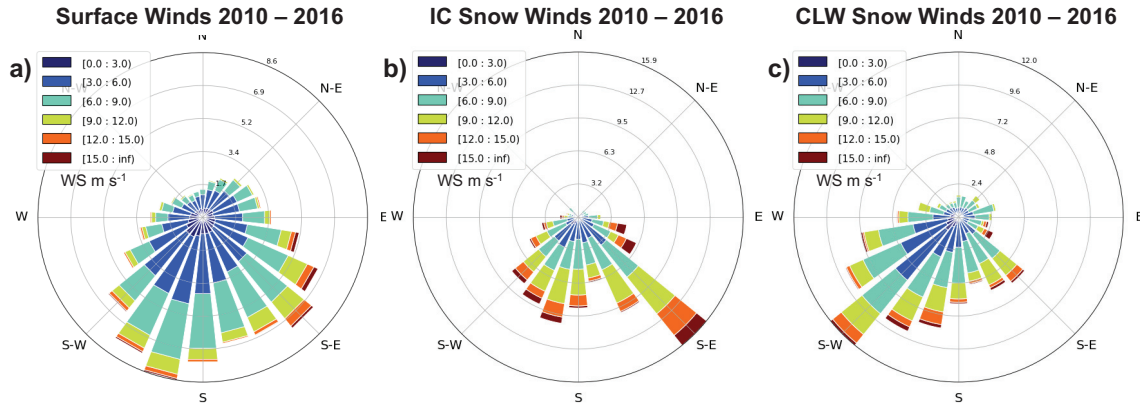


Figure 6.7 Surface winds from the Summit NOAA meteorological data are shown. For reference, Panel a shows all surface winds from 2010 –2015 for all times. Panel b (middle) shows the surface winds for the MWR-determined IC snow cases. These winds tend to come out of the southeast with little variability and are much stronger than the average winds. Panel c (right) shows the surface winds for the MWR-determined CLW containing snow cases. Associated winds tend to be from the west to south with a maximum amount from the southwest direction. Though the CLW snow cases have stronger winds than average, they are not as strong as the winds associated with the IC snow.

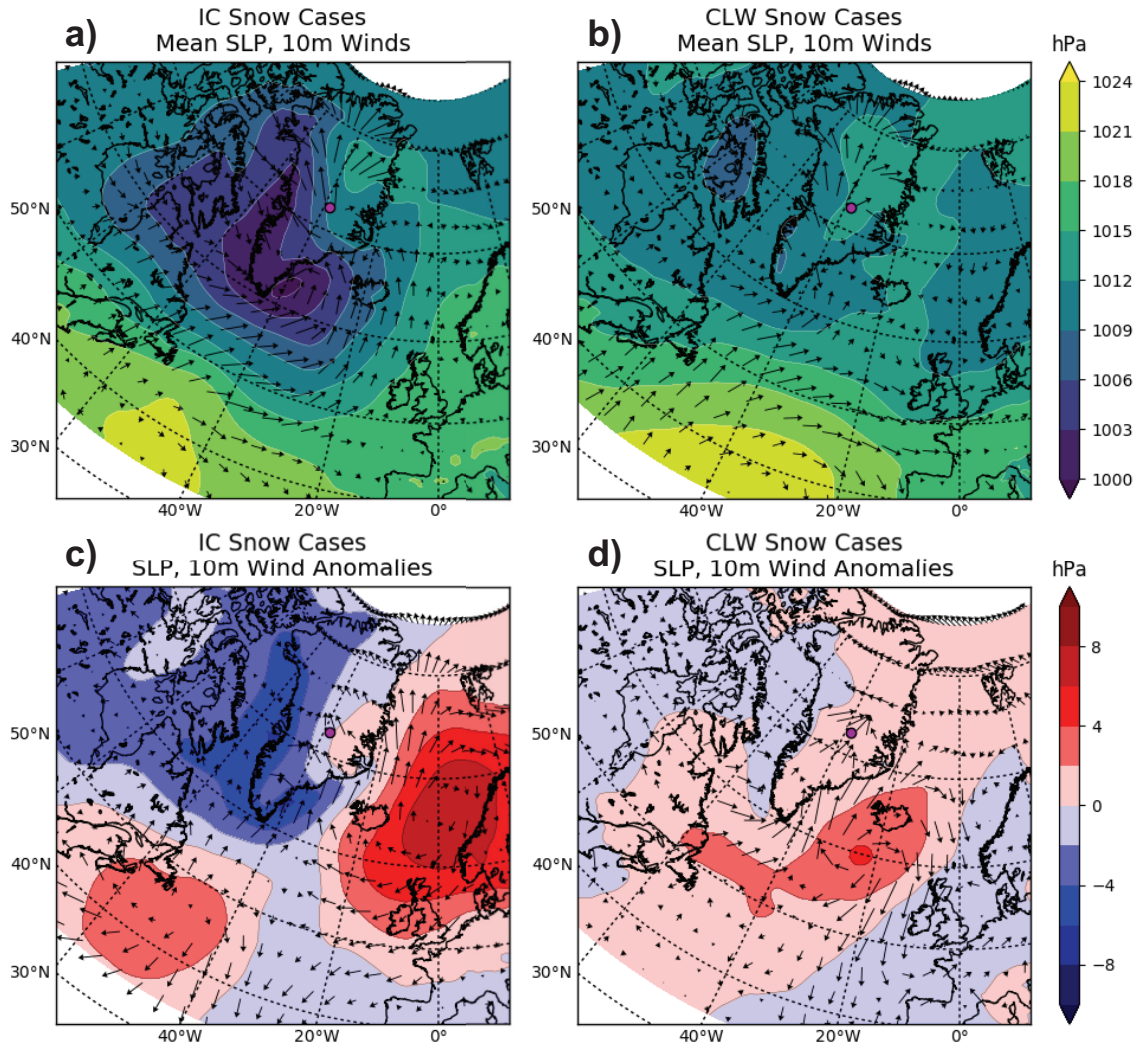


Figure 6.8 Panel a (top, left) shows the ERA-Interim derived average SLP and 10 meter winds for 90 IC snow events. Panel b (top, right) shows the same, but for 84 CLW snow events. Both plots are on the same scale. Panels c and d show the anomalies for the SLP and 10 meter winds for the respective cases. The persistent low pressure and strong 10-meter winds are evident for the IC snow cases. In the cases for the CLW snow, there are relatively calm winds and uniform mean SLPs. Both the cyclone and anti-cyclone structure features in the IC snow cases are quite anomalous, whereas the broad high-pressure field in the CLW cases is weakly anomalous.

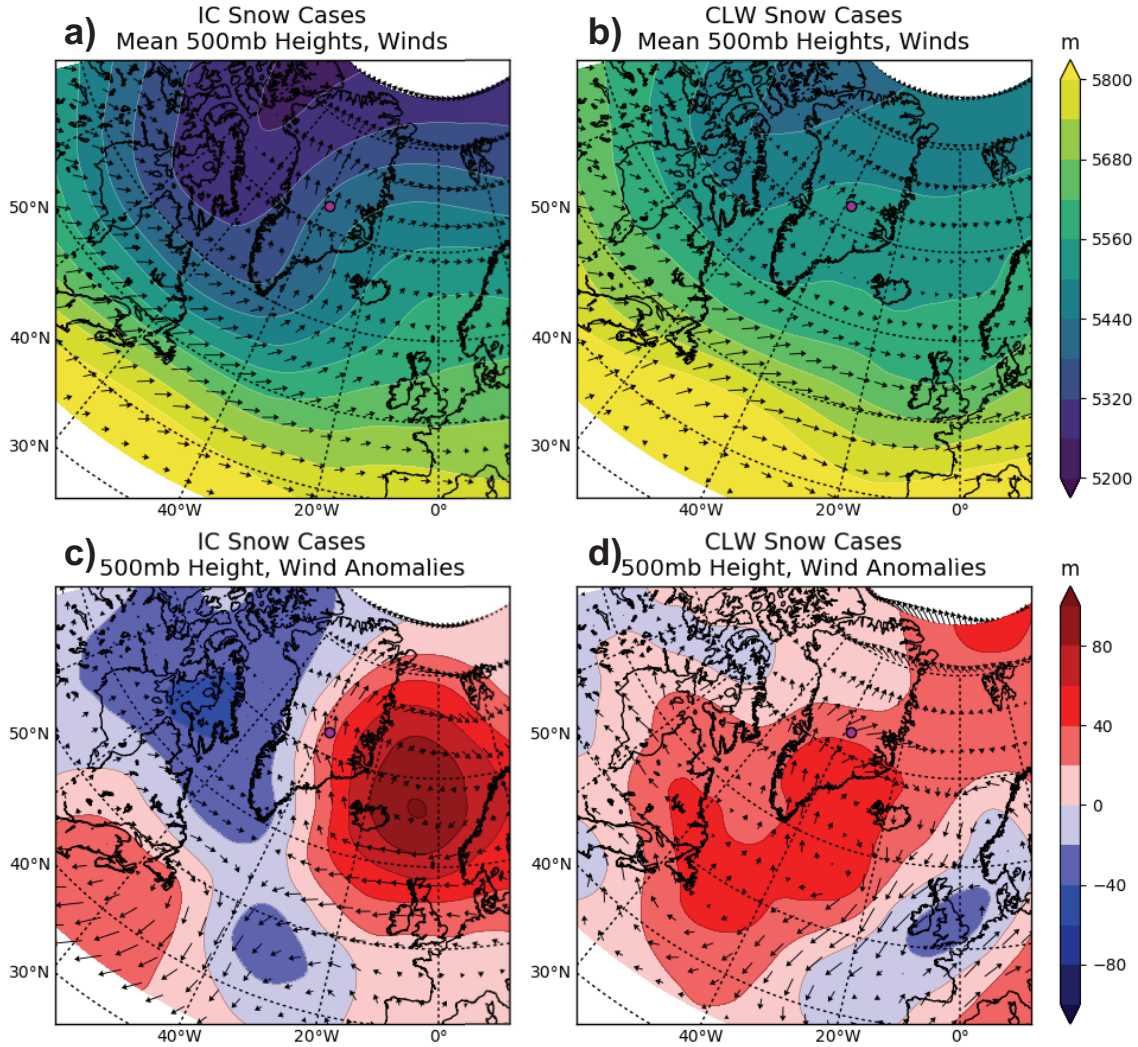


Figure 6.9 Panel a (top, left) shows the ERA-Interim derived average 500mb geopotential heights and winds for 90 IC snow events. Panel b (top, right) shows the same, but for 84 CLW snow events. Both plots are on the same scale. Panels c and d show the anomalies for the 500mb heights and winds for the respective cases. There is an incredibly strong trough and ridge feature in the IC snow cases. This feature indicates diverging upper-level winds just to the east of the trough, over the SE Greenland coast, which would induce strong vertical motions in the column and the upper level winds up show strong SE flow over the GIS. The CLW cases depict relatively calm and flat features, indicating quiescent flow of air up over the GIS from the S and SW.

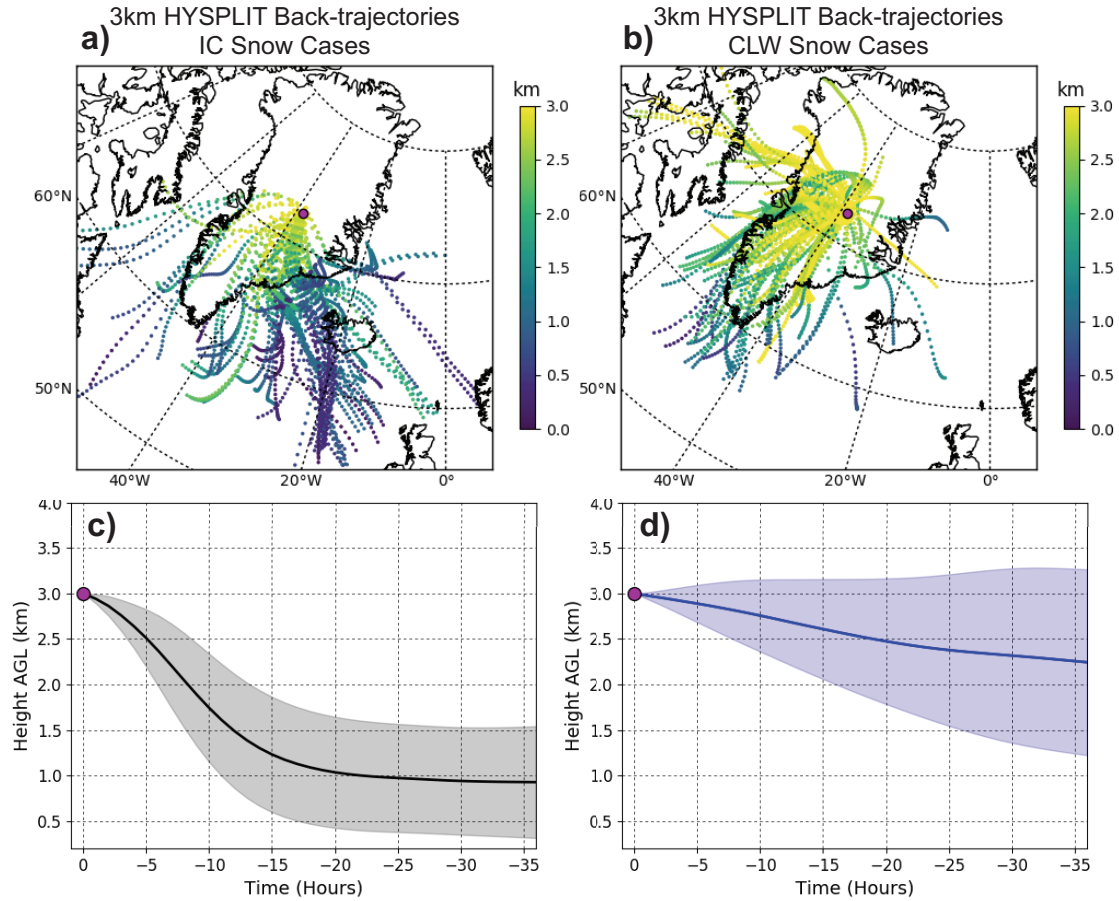


Figure 6.10 Panel a (top, left) shows the HYSPLIT calculated, 36 hour backtrajectories for the air at 3 km AGL originating at Summit using GFS for the IC snow cases. The backtrajectory AGL values represent the altitude above ground along each trajectory path. Panel b (top, right) shows the same, but for the CLW cases. The bottom two Panels (c and d), show the mean vertical motions (dark line) and standard deviation (lighter fill) for the IC and CLW cases, respectively. These are consistent with the previous figures: the IC snow cases being vertically lifted and advected over the GIS from the SE. While the CLW cases come from the S and SW along the mean flow.

Chapter 7

7 Precipitation regimes, climate indices, and storm tracks

7.1 Introduction

Recent work has indicated a thinning along the edges of the GIS due to melt and a thickening of the central region due to precipitation (Hanna et al., 2006; Hanna et al., 2013). The interior thickening is not well constrained (Thomas et al., 2000). Previous work has explored the connection of precipitation to both climate variability in the North Atlantic (Appenzeller et al., 1998; Bromwich et al., 1999; Hutterli et al., 2005; Mosely-Thompson et al., 2005; Hanna et al., 2013, Hanna et al., 2016) and the interactions of cyclones with Greenland (Chen et al., 1997; Bromwich et al., 1998; Rogers et al., 2004; Schuenemann et al., 2009). Historically, work has focused on connecting variations of the North Atlantic Oscillation (NAO) with precipitation patterns over the GIS (Appenzeller et al., 1998; Bromwich et al., 1999). More recently, a newer metric, the Greenland Blocking Index (GBI), has been linked to precipitation patterns in Greenland (Hanna et al., 2016). Additionally, there have been several studies of specific North Atlantic storm track intensity and location and the resulting influence on precipitation variation over regions of the GIS (Chen et al., 1997; Schuenemann et al., 2009; Schuenemann and Cassano, 2009).

We explore connections of precipitation at Summit Station to the NAO, GBI, and storm tracks using the dataset available from the ICECAPS project. Using our novel snow classification tool, introduced and described in Chapter 5, we can partition snow into two regimes: snow from fully-glaciated clouds (IC) and snow from mixed-phase clouds

(CLW). Prior work by Pettersen et al. (2017) found that IC snow accounted for 35 % of the precipitation accumulation at Summit Station while CLW snow was about 51 %, and found that each snow regime is associated with distinctive cloud characteristics and large-scale dynamics (see Chapter 6). In this work, we aim to investigate possible connections of each snow regime to either climate variability or storm tracks or both. We look at longer duration IC and CLW events as observed by ICECAPS and their associated NAO and GBI indexes. We then will look at the associated mean sea level pressure (SLP) and 500 mb geopotential height (GPH) anomalies for all events and as a function of the season of occurrence. By combining the large-scale patterns with climate indices, we may be able to attribute snow types to either climate indices or specific North Atlantic storm tracks.

7.1.1 Event selection and methods

The regional meteorological patterns were created using the ERA-Interim reanalysis described in Chapter 3, Sect. 3.3.1. We are using the surface SLP, 10 meter wind, and the height and wind values at the 500 mb geopotential level. The anomalies are calculated by subtracting the all-times monthly mean value from the event specific value at each latitude and longitude (i.e., the mean value for all other Junes would be subtracted from the June 12, 2012 event). The NAO index values used in this work are from the NOAA NCEP data repository, described in Chapter 3, Sect. 3.3.3 (Barnston and Livezey, 1987; Hurrell 1995). The GBI is calculated by averaging all the 500 mb GPH heights within a region of 60 – 80 N and 20 – 80 W, and values are obtained from NOAA ESRL, and are available from 1948 – 2015 (further described in Chapter 3, Sect. 3.3.3; Hanna et al., 2016).

For this work, we are using 6 years of ICECAPS data combined with the MWR classification tool outlined in Chapter 5. The IC and CLW events used in the study are identified using criteria of occurring for 50 minutes in a given hour and within 2 hours of an ERA-Interim reanalysis time step. Additionally, since there is only one index value per day, we do not use repeated hours within the same day. Using this method, we acquired 98 IC events and 82 CLW events. As illustrated in Table 7.1, the IC tend to occur in September, October, November (SON). While the CLW events occur mostly in June, July, August (JJA). There are a few IC snow events in December, January, and February (DJF), and one CLW snow event March, April, May (MAM).

7.2 Climate index results

The relationship between the NAO and the IC and CLW events is shown in Fig. 7.1. The top panel of Fig. 7.1 shows the normalized counts of NAO for all times (black solid line) and during the ICECAPS period from 2010 – 2016 (dashed black line) from -2.2 to 2.2. These two distributions are fairly similar indicating there is no relative shift in the NAO index values for the ICECAPS time range versus the entire time range. The middle panel shows the NAO index distribution of the 98 IC events in black and the bottom panel shows the distribution of the 82 CLW events in blue. The IC events are distributed fairly symmetrically about 0, while the CLW events are shifted towards the NAO negative phase index values. The mean and standard deviation of the NAO index values for the IC events are -0.05 ± 0.77 and for the CLW events are -0.51 ± 0.73 . These results indicate that the IC events are not correlated to a particular phase of the NAO, while the CLW events occur typically for the negative phase of the NAO, though with a fairly broad range of index values.

The GBI values vary as a function of season with the 500 mb geopotential heights generally higher in the warmer months over Greenland as illustrated in Fig. 7.2 (grey, small dots). The IC (black stars) and CLW (blue circles) snow events are over plotted to illustrate their annual cycle as well. Due to the seasonal variation of GBI heights, we need to consider the distribution of both the GBI heights and their anomalies (with respect to the 1948 – 2015 climatology) associated with each snow regime. To account for the seasonality of the GBI heights, the anomalies are calculated for a given day by subtracting the mean GBI height value for all other years for that same day (i.e., for June 12, 2012, we would subtract a mean value from the June 12 date for all other years from 1948 – 2015). Since the GBI daily data is currently available only through June 2015, we have fewer events: 65 IC and 72 CLW snow events. The majority of the CLW events are in JJA, the season that tends to have the highest average geopotential heights, while the majority of IC events are in SON.

Figure 7.3 shows the distribution of the GBI heights (left panel) and anomalies (right panel). The left, top panel shows the GBI heights for all times (black solid line) and during the ICECAPS period (black dashed line) and mostly shows a similar distribution, however the ICECAPS time period shows slightly higher height values. The left, middle panel shows the distribution of GBI heights for the IC events (black) and the left, bottom panel shows the CLW events (blue). The CLW events have high corresponding GBI with a fairly narrow range of heights. While the IC snow cases are broadly dispersed across a range of GBI heights. The mean and standard deviation of the GBI heights for the IC events are 5389 ± 139 meters and for the CLW events are 5516 ± 74 meters.

The right, top panel shows the normalized counts of GBI height anomalies from 1948 to 2015 (black solid line) and during the ICECAPS time range (from 2010 – 2015; black dashed line). In general, the GBI height anomalies are evenly distributed from -300 to 300 meters, however, there is evidence of a shift towards positive GBI anomalies during the ICECAPS time period. The IC snow event associated GBI anomalies are in the right, middle panel (black), and the CLW snow events are in the right, bottom panel (blue). In general, the IC snow events are fairly evenly distributed from -100 to 100 meters, with a few events greater than 100 meters. The CLW events tend to be associated with positive GBI height anomalies with the majority being between 0 and 175 meters. Interestingly, there are no events for either type with GBI height anomalies less than about -100 meters, whereas the positive anomalies range up to 300 meters. The mean and standard deviation of the GBI height anomalies for the IC events are 7.1 ± 71.1 meters and for the CLW events are 54.4 ± 75.9 meters.

We also examined the NAO index, GBI heights, and GBI height anomaly values compared to mean snow rate associated with an individual IC or CLW event. Figure 7.4 shows a scatter plot of mean snow rate versus NAO index (top), GBI height (middle), and GBI height anomalies (bottom). The IC snow events are depicted with black stars and the CLW events are depicted with blue circles. In general, there is little or no correlation of mean snow rate and any of the indices for the IC snow events. There is a slight indication of higher mean snow rates for the CLW events that coincide with the negative NAO phase, however there is also very large variance in the values. There also seems to be a connection of higher mean snow rates and GBI height for the CLW events. However, the

mean snow rates and GBI height anomalies seem to have no correlation for the CLW cases.

7.3 Sea level pressure and geopotential height anomaly results

Similar to Chapter 6, Sect. 6.3.2, we use the ERA-Interim Reanalysis products to examine the regional meteorological patterns at the surface and the upper levels for the IC and CLW events. We examine the anomalies of SLP and 10 meter winds, as well as the anomalies of the 500 mb GPH and upper level winds for the IC and CLW events. In the previous work, we looked at the anomaly patterns for all events in each classification as a composited value, however we did not look at the anomalies as a function of season of occurrence. Due to the general weakening of the NAO and the higher GBI height values during the JJA period, we organized our reanalysis figures to illustrate the mean anomaly patterns from: all events, those in JJA, and those in SON for both the IC and CLW snow, respectively.

Figure 7.5 shows the patterns for the anomalies of SLP and 10 meter winds for both the IC and CLW snow events. The top, left panel shows the mean anomalies for all IC snow events, the top, middle panel shows the IC events that occurred in JJA, and the top, right panel shows the IC events that occurred in SON. The mean SLP anomalies for the JJA IC events illustrate an anomalous weak to moderate low in Baffin Bay and over most of the GIS, with a weak high anomaly to the southeast toward the United Kingdom. The IC events in SON show a stronger low-pressure anomaly (<-8 hPa) through the Baffin Bay and wrapping around the southern tip of Greenland to the southeast coast. There is also a strong anti-cyclone anomaly just off the east coast of Greenland. The SLP anomaly map for all IC events looks similar to the SON patterns, which is due to the majority of the IC

events occurring in SON. In all three maps, the 10 meter wind anomalies at Summit Station (denoted with the purple circle) are from the southeast, which is consistent with the surface wind observations seen at Summit Station during the IC snow events (see Fig 6.7).

In the bottom panels of Fig. 7.5, the SLP and 10 meter wind anomalies for all CLW events (bottom, left panel), the CLW events in JJA (bottom, middle panel), and the CLW events in SON (bottom, right panel) are shown. In JJA, the CLW events are coupled with a very weak mean SLP anomaly pattern over the majority of the GIS with slightly higher SLP anomalies to the south of Greenland. The SON CLW events are coincident with a large area of high SLP anomalies (>8 hPa) covering the majority of the selected region. The composited result for all CLW cases shows a broad region of high SLP anomalies with an anticyclonic anomaly feature just south of Iceland. In all the CLW cases, regardless of the season, the wind anomalies are from the southwest at Summit Station. Again, this is consistent with the surface wind observations for the CLW events at Summit Station (see Fig 6.7).

Figure 7.6 shows similar maps, but for the upper-level conditions using the 500 mb geopotential height (GPH) and wind anomalies. In the top panels of Fig. 7.6 the mean anomalies for the 500 mb GPH and winds are shown for all IC events (top, left), the IC events in JJA (top, middle), and the IC events in SON (top, right). In all three maps, there is a dipole pattern with an anomalous trough to the west of Greenland and a ridge to the east. This dipole is situated along the long axis of Greenland, though shifted east in JJA and west in SON. The low and high 500 mb GPH anomalies in SON are larger than JJA, ranging from -60 meters to >80 meters. In all the anomaly maps for the IC events, the

upper-level wind anomalies are from the southeast, from off the southeastern coast of Greenland to Summit Station.

The CLW events for all times are depicted in Fig. 7.6, bottom, left panel, while JJA CLW events are in the bottom, middle panel, and SON CLW events are in the bottom, right panel. In all three maps for the CLW snow, there is a broad high anomaly of GPH over all of Greenland and most of the featured region. This anomalous ridge is slightly lower in JJA, ranging 40 – 60 meters, while a much larger anomaly in SON with most of the area over the GIS higher than 80 meters. In all the CLW events, regardless of season, the 500 mb wind anomalies are from the south to southwest, and southwest over Summit Station.

7.4 Discussion

The IC snow events identified are seemingly uncorrelated with the NAO index and the GBI heights as depicted in the histograms in Fig. 7.1 and 7.3. This is consistent with the SLP anomaly maps patterns for the IC snow events, shown in Fig. 7.5, as there is a SLP anomaly dipole near Iceland, but no strong evidence of a weakened Icelandic Low. The GPH height anomalies for the IC snow events illustrated in Fig. 7.6 again show a dipole structure with a trough and ridge centered along the long axis of Greenland. The GBI value is an average height over most of Greenland and would include both the negative and positive GPH anomalies, therefore an average value would not be representative of the dipole structure (GBI calculation region shown in yellow in left panels of Fig. 7.6). Consequently, it is not surprising that there is not a correlation between either the NAO or the GBI with the IC snow events.

The SLP anomaly maps indicate the presence of low-pressure storms in the Baffin Bay and around the southern tip of Greenland during the IC snow events. Additionally, the GPH height anomalies for the IC snow events indicate a trough and ridge dipole structure that is consistent with frontal systems (Holton, 2004). Chen et al. (1997), showed that cyclone tracks along the western coast of Greenland into Baffin Bay and along the southern tip of the island lead to positive precipitation anomalies over the southern GIS (see Fig 2.6 in Chapter 2). Additionally, Schuenemann et al. (2009), found that lows along the Baffin Bay, low-pressure storms split by the topography of the southern tip of Greenland, and cyclones adjacent to the southeastern coast all produced positive precipitation anomalies over the southern and central GIS. Furthermore, studies find that Greenland lee cyclogenesis is coupled to increased convection precipitation in the southeastern part of the GIS (Chen et al., 1997; Bromwich et al., 1998; Rogers et al., 2004). Schuenemann et al. (2009) found that the Baffin Bay lows in the summer months were weaker while the intense cyclones were more frequent in fall and winter, which is consistent with patterns seen in the JJA and SON IC events, respectively. The SLP and 500 mb GPH height anomaly patterns observed for the JJA and SON IC events are consistent with previous studies of the North Atlantic storm tracks that lead to precipitation over the GIS.

The CLW events are related to the negative phase of the NAO with a mean index of -0.51 ± 0.73 , however this is somewhat weak and there is a large variance in the values. The positive phase of the NAO has been connected to a general reduction of precipitation over the GIS (Hurrell, 1995; Chen et al., 1997; Bromwich et al., 1999). While the negative phase of the NAO is connected to weaker westerly winds, which generally leads to large

scale atmospheric flow from the southwest coast of Greenland onshore advecting moisture onto the GIS (Hurrell, 1995; Bromwich et al., 1999). The mean SLP anomalies for the CLW snow events in Fig. 7.5 show positive SLP anomalies over most of Greenland and just to the south of Iceland, which is consistent with the regional characteristics of the negative phase of the NAO as the Iceland Low is weakened. The 10 meter wind anomalies are mainly from south and southwest coast of Greenland, approaching Summit Station from the southwest, implying that the mixed phase clouds associated with the CLW precipitation likely advected over the GIS from the southwest of Summit Station. Previous studies in western and southern Greenland linked ice core derived accumulations with a correlation to the negative phase of the NAO (Appenzeller et al., 1998; Mosely-Thompson et al., 2005).

The CLW events are co-located with a range of GBI heights on the high end of the height climatology (see Fig. 7.3). This is not surprising as the majority of these events (80 %) occurred in JJA when the GBI heights are highest. However, the CLW events are also related to phases of high GBI anomalies, when compared to the climatology from 1948 – 2015, with a mean value of 54.4 ± 75.9 meters. This is consistent with previous studies, which showed that GBI is anti-correlated with the NAO with higher than average 500 mb GPH observed during the negative phase (Hanna et al., 2016). The GPH anomalies for the CLW snow events are almost exclusively positive over Greenland and throughout the region (see Fig. 7.6.). High GBI values are connecting to large regions of high surface pressure and warmer than average temperatures over the GIS (Hanna et al., 2013). The 500 mb GPH anomaly maps also indicate large regions of calm conditions where mixed phase clouds have been shown to persist and last long periods of time, possibly

precipitating on the way to Summit (Morrison et al., 2012). Additionally, the occurrence of long-lived mixed-phase clouds as detected by ICECAPS is shown to be connected to the negative phase of the NAO (Edwards-Oppenheimer et al., 2017).

7.5 Summary

This work connects six years of observations from a single point in the central GIS to the associated large-scale dynamics and anomalies; therefore we can comment briefly on the implications of some of the well-used indexes and the impacts of major North Atlantic storm tracks. We first examined the associated NAO indexes for the IC and CLW snow cases. For the majority of the CLW cases, the NAO phase is weakly negative and this parallels previous studies of snowfall over the GIS (Appenzeller et al., 1998; Bromwich et al., 1999; Mosely-Thompson et al., 2005). The IC snow cases have no correlation with an NAO phase. Hanna et al. (2016) found that during precipitation over the GIS, the GBI index is high as “milder, moister southerly winds are advected over the ice sheet.” We found that the calculated mean GBI for the identified CLW events was positive, which agrees with findings from Hanna et al., 2016. However the GBIs that correlated to the IC snow events were not especially high. Though GBI may accurately represent the dynamical forcing for the CLW snow events, which do have a high anomaly over much of the GIS, it is not representative of the dynamics in the IC snow events. The dipole structure in the 500 mb GPH anomalies associated with the dynamics of the IC snow is centered in the middle of the GBI determined region, and therefore a single height is not an accurate representation.

Preliminary comparisons to precipitation predictions based on climatological indexes shows that the GBI positive mode and NAO negative mode are consistent in the

literature for describing the dynamics connected with CLW snow precipitation. CLW snow events originating from mixed-phase clouds are coupled to slowly advecting air masses from the south and southwest coasts of Greenland, which is consistent with current literature for the GBI and NAO indexes (Hanna et al., 2016; Bromwich et al., 1999). However, these index modes do not represent the dynamics of the IC snow cases. The implication is that IC snow processes are more connected to specific storm systems that interact with the Greenland ice sheet, in particular Greenland ridge lee cyclones, Baffin Bay lows, and the bifurcation of Baffin Bay low-pressure systems. Previous work has shown that these types of individual storms generate precipitation on the central GIS (Kapsner et al., 1995; Chen et al., 1997; Schuenemann et al., 2009).

Table 7.1 The IC and CLW snow events as a percentage of occurrence for each season.

	JJA	SON	DJF	MAM
IC Snow Events	30 %	63 %	7 %	0 %
CLW Snow Events	78 %	20 %	0 %	2 %

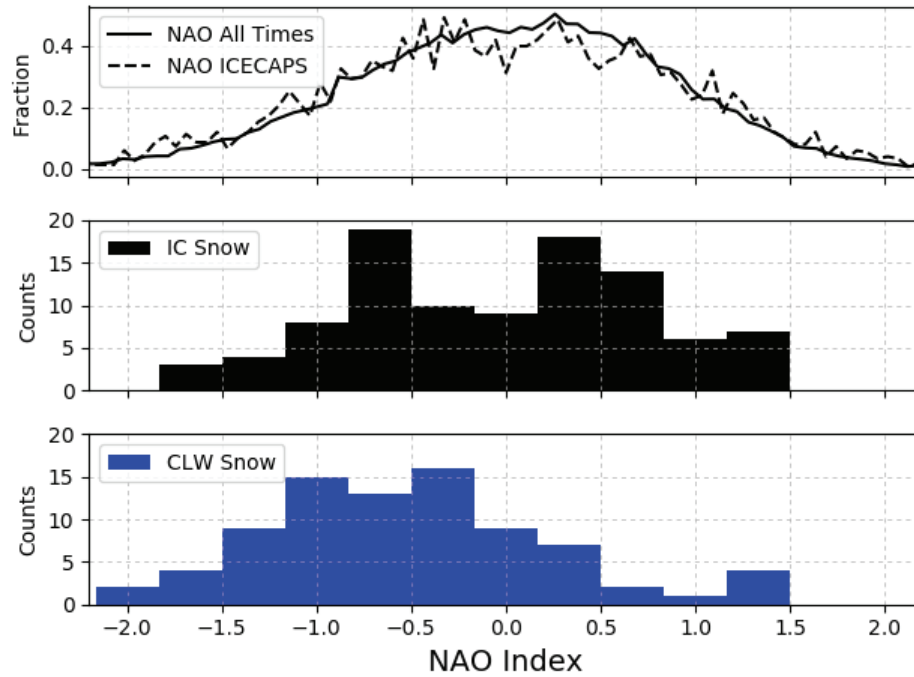


Figure 7.1 NAO index for all times (1950 – 2017), black solid line, and NAO index for ICECAPS time frame (2010 – 2017), black dashed line. These are shown in fraction of counts. The middle black is a histogram of IC snow events (98) and the bottom blue is a histogram of CLW snow events (82). The mean and standard deviation of the NAO index for the IC events are -0.05 ± 0.77 and for the CLW events are -0.51 ± 0.73 .

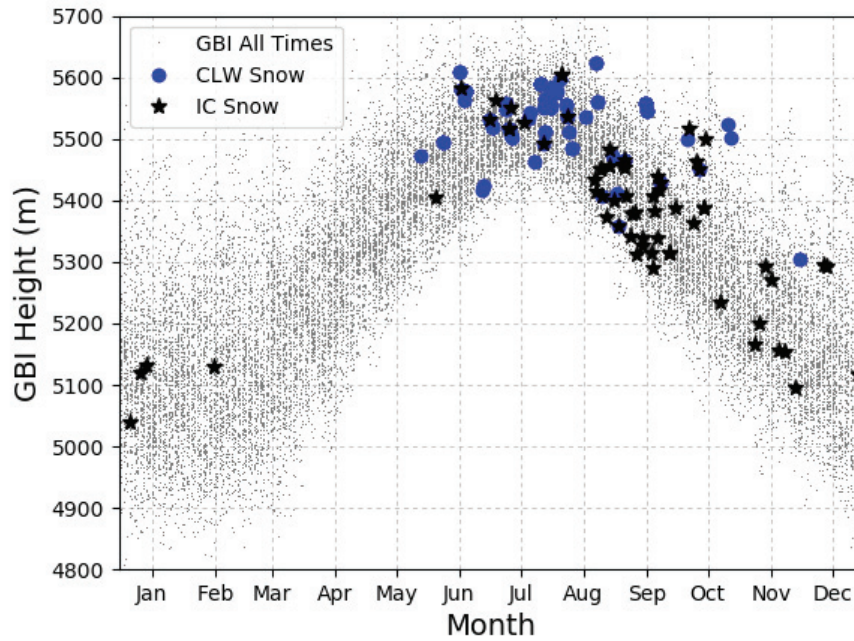


Figure 7.2 Annual cycle of GBI values shown in height versus the day of the year. Each blue point is a value for the days from 1948 – 2015. There is a large dependence on the height as a function of the season. For example, the January mean GBI height is ~5100 meters, while in July it is ~5500 meters. There is the largest variance of values in the northern hemisphere winter months. The IC events are plotted in black stars and the CLW events are plotted in blue circles.

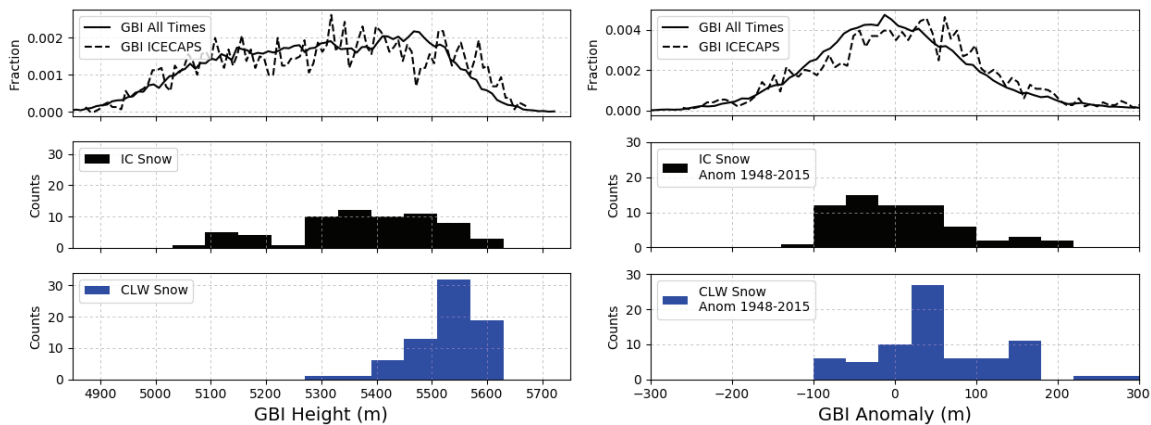


Figure 7.3 The left panels show the GBI heights for all times (1948 – 2015), black solid line, and GBI heights for ICECAPS time frame (2010 – 2015), black dashed line, shown in fraction of counts (top). The left, middle panel in black is a histogram of IC snow events (65) and the left, bottom panel in blue is a histogram of CLW snow events (72). The right top panel in green is the ICECAPS time range GBI anomalies (versus the days from 1948 – 2015). The right, middle panel is the histogram of the GBI anomalies compared to the 1948 – 2015 time period for the IC events (black). The right, bottom panel is the histogram of the GBI anomalies compared to the 1948 – 2015 time period for the CLW events (blue).

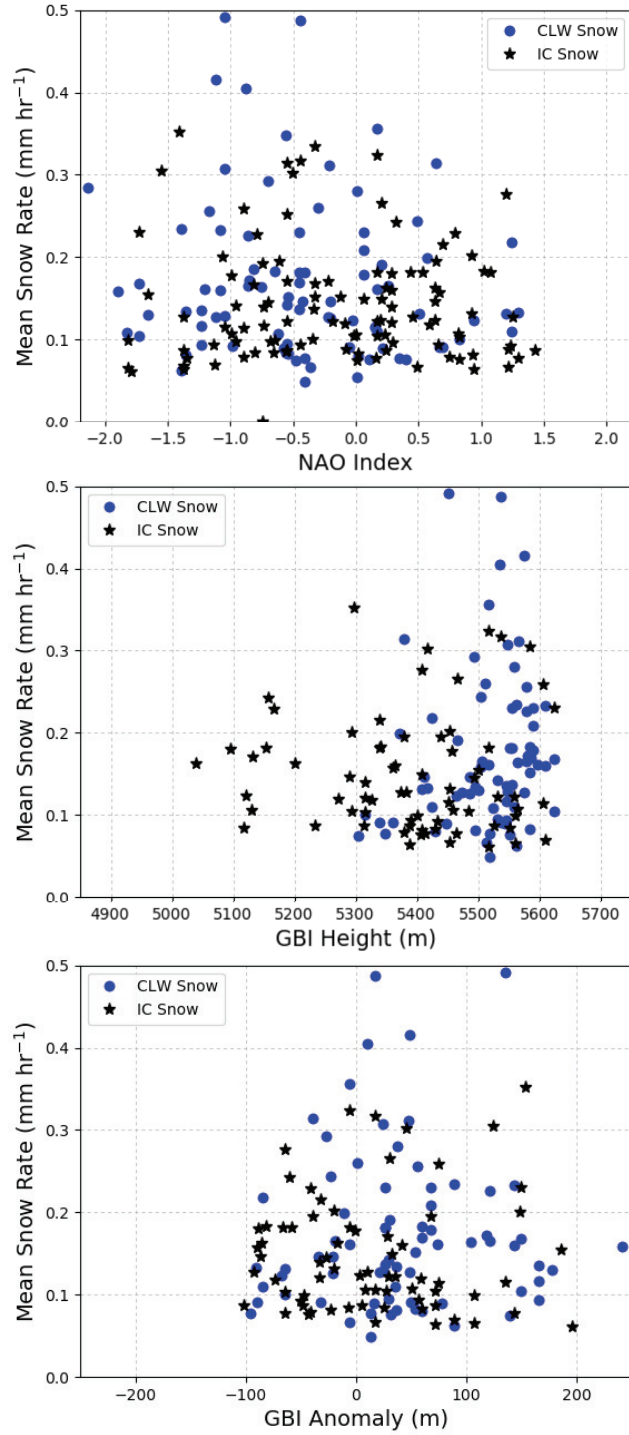


Figure 7.4 Scatter plots for the mean snow rate values and the various indices: NAO (top), GBI height (middle), GBI anomaly (bottom). The IC events are depicted with black stars and the CLW events are depicted with blue circles.

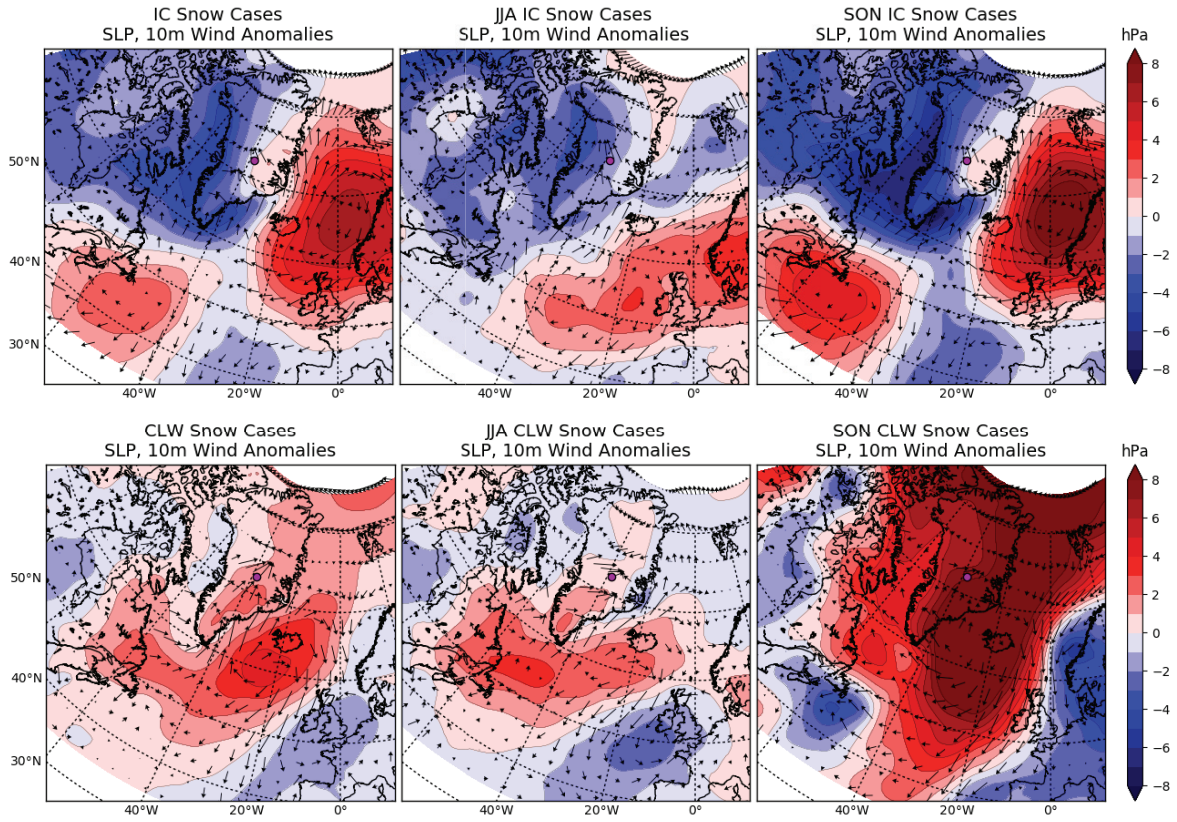


Figure 7.5 The SLP and 10 meter wind anomalies for the IC snow cases (top) and the CLW snow cases (bottom). The left panels show the SLP and 10 meter wind anomalies for all IC cases (top) and CLW cases (bottom). The middle panels show the SLP and 10 meter wind anomalies for the JJA events for each snow type (IC, top; CLW, bottom). The right panels show the SLP and 10 meter wind anomalies for the SON events for each snow type (IC, top; CLW, bottom).

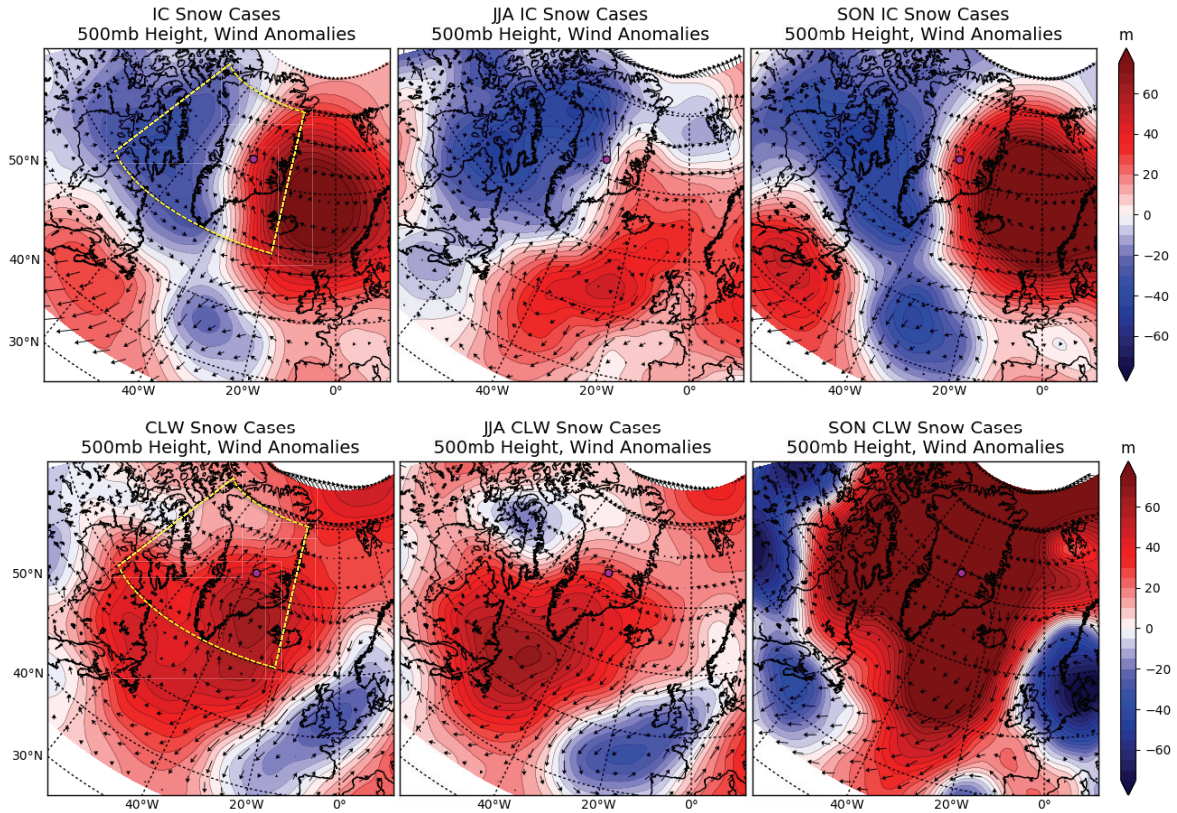


Figure 7.6 The 500 mb GPH and wind anomalies for the IC snow cases (top) and the CLW snow cases (bottom). The left panels show the 500 mb GPH and wind anomalies for all IC cases (top) and CLW cases (bottom). The middle panels show the 500 mb GPH and wind anomalies for the JJA events for each snow type (IC, top; CLW, bottom). The right panels show the 500 mb GPH and wind anomalies for the SON events for each snow type (IC, top; CLW, bottom). The yellow dashed lines outline the area used for averaging the 500 mb GPH heights to calculate the single GBI value.

Chapter 8

8 Conclusions

Using ground-based remote sensing and in-situ instrumentation, we are able to better characterize the precipitation events at Summit Station. By utilizing measurements from the ICECAPS suite and NOAA TAWO meteorological data, as well as implementing radiative transfer models and using reanalysis products outlined in Chapter 3, we are able to further our understanding of the precipitation processes in the central GIS. Adding information about specific snow regimes occurring at Summit Station help to constrain the mass balance of the central GIS and enable a better understanding of the regional meteorological conditions that lead to precipitation over Greenland.

In Chapter 4, we outlined a method to isolate the ice hydrometeor signature in high-frequency MWR channels and examined several summers of observations from the ICECAPS data record. We found that the cloud and precipitation characteristics observed by the MMCR for events with less than 40 g m^{-2} LWP were very different from those events with more than 40 g m^{-2} LWP. Additionally, through this work we learned that the LWP retrievals during precipitation events at Summit Station were biased by the ice hydrometeors. This discovery led to the development of a novel tool, which uses the low-frequency and high-frequency MWR window channels to partition precipitation events into distinct snow regimes (see Chapter 5).

We find that precipitation observed at Summit Station can be broadly classified into two regimes: snow originating from a fully-glaciated ice cloud (IC snow) and snow originating from an Arctic mixed-phase cloud (CLW snow). In Chapter 6, we summarized properties of each snow type: IC snow accounts for $\sim 35\%$ of all accumulation at Summit

Station and occurs throughout the year with higher accumulations in August through November; while CLW snow accounts for about half the accumulated precipitation and occurs almost exclusively from June through September. We found that IC snow is coupled to deep clouds, while the CLW snow was associated with shallower clouds. In general, the snow regimes originate from different directions with the IC snow associated with stronger than average winds from the southeast and the CLW snow associated with moderate winds from the south and southwest. Additionally, we found that very different dynamics seemed to be driving each snow regime and in Chapters 6 and 7, we explored further the dynamics associated with each snow regime. We found that IC snow events are coupled to low-pressure systems tracking through Baffin Bay or across the southern tip of Greenland, while the CLW snow events seem to be connected to the negative phase of the NAO and anomalously high values of GBI.

8.1 Future work and applications

The snow regime classification tool has proved useful in illuminating some of the questions concerning the origination and transport of air masses that produce precipitation at Summit Station. However, there are many additional complimentary studies that could be performed:

- The snow classification regime tool could be applied to similar Arctic ground-based instrument sites, such as the DOE ARM sites at Barrow and Oliktok Point.
- Current work uses reanalysis products to capture a regional picture of the precipitation processes, but satellite products could be explored as a means to further augment and strengthen these findings.

- The IC snow events identified in this work are ideal cases in which to test and refine PSDs and ice habit assumptions in ice scattering models.
- Studies of the different snow regimes could lead to information about ice nucleating particles and their origins.

As stated earlier, the ICECAPS suite of instruments is similar to those at DOE ARM ground-based climate research facilities (Ackerman and Stokes, 2003). Currently, there are two Arctic-based atmospheric observatories with similar instruments: a permanent facility on the North Slope of Alaska (NSA), near Barrow, and a mobile facility at Oliktok Point, Alaska (OLI). Both sites have MWRs with a low-frequency window channel (31.40 GHz), the NSA facility has an MWRHF (90 and 150 GHz channels) and OLI has an MWR with a 90 GHz channel. The MWR snow classification tool outlined in Chapter 5 could be applied to the MWR data from both NSA and OLI with a similar characterization of the snow processes. It would be interesting to see if similar snow regimes exist in other regions of the Arctic, or if these precipitation events are unique to the central GIS. There are potential challenges in employing the MWR snow classification technique to other Arctic sites as the extremely dry environment at Summit Station is unique, and it may be difficult to apply to NSA and OLI with similar success due to the higher optical depths in a more WV-rich environment.

Studies of clouds in the Arctic using active and passive remotely sensed measurements from satellites highlight these spaceborne systems as potential tools for expanding this work beyond Summit Station. Recent work using observations from satellite illustrated that Arctic clouds are enhancing GIS meltwater runoff when compared to clear sky conditions (Van Tricht et al., 2016). Additionally, satellite-based studies of

precipitation over the GIS, showed that the southeastern region of Greenland is dominated by deeper snowfall structures (Kulie et al., 2016). We can use observations from the CloudSat Cloud Profiling Radar (Stephens et al. 2002) coincident with identified snow events from each regime to obtain a regional picture of the corresponding clouds and their physical and spatial characteristics. By using the added spatial context from available satellite observations, we can further connect the observations from ICECAPS to the greater GIS.

Modeling the scattered microwave radiation from the ice hydrometeors in the atmosphere is a non-trivial task and requires a-priori knowledge of PSDs and ice habits (Kulie et al., 2010). This is further complicated by accurately modeling the emission from the CLW present in the atmosphere. We can better test the likely PSDs and ice habits present at Summit Station by using the ICECAPS observations during IC snow events. During the IC snow events, we do not need to consider the effects of the CLW and this simplifies the approach. In-situ measurements of the temperature, relative humidity, and pressure from radiosondes and reflectivity profile data from the MMCR can both be utilized as inputs into a radiative transfer model. We can use databases of PSDs available and test their applicability to the environment at Summit Station during the IC events (Matrosov et al., 2003; McFarquhar and Cober, 2004; Heymsfield et al., 2013). Additionally, we can use IcePIC images to choose likely ice habits for modeling the ice scattering. This modeling work can lead to a better understanding of likely PSDs and ice habits present during IC snow events, which aids in creating more accurate values of ice water path (IWP). Using these improvements, we can then create a joint MWR-based

retrieval of the PWV, LWP, and IWP through improved modeling of the IWP combined with the existing PWV and LWP retrieval method.

The amount of ice hydrometeors present directly affects the precipitation properties and radiative characteristics of a cloud. The formation of ice hydrometeors within the cloud is strongly modified by the availability of ice nucleating particles (INP) within an air mass. INPs are aerosols that allow ice to heterogeneously freeze at higher temperatures or lower relative humidity than would in a clean (aerosol free) environment, as CLW droplets have been observed to remain liquid down to $-40\text{ }^{\circ}\text{C}$. Understanding the sources of INP and how they may be connected to the IC snow events at Summit Station is a worthwhile study. For example, feldspar is an excellent INP and found in the Saharan Air Layer (Atkinson et al., 2013) and it would be useful to know if there are particularly high amounts concurrent with the IC snow events. Additionally, recent work by Wilson et al. (2015) found a marine biogenic source of INP in high concentration around the southern tip of Greenland and off the southeastern coast. Connecting the IC snow events with their possible sources of INPs would be a key component in understanding in how these air masses produce snow over the central GIS.

These are only a few examples of combining the available ICECAPS observations and products with outside instrumentation or datasets to potentially enhance our understanding of precipitation origin, formation, transport, and deposition over the GIS. We aim to highlight the flexibility and worth of the ice hydrometeor and snow classification method as a means to add to the expanding collective knowledge of Arctic precipitation characteristics and processes. We feel that the body of work presented in this

dissertation contributes to a better understanding of precipitation accumulation and constraining the processes that lead to mass deposition in the central GIS.

Appendix A: Acronyms

Acronym	Name
2DH	Two-Dimensional Histogram
AGL	Above Ground Level
AMOC	Atlantic Meridional Overturning Circulation
AMP	Arctic Mixed Phase
AO	Arctic Oscillation
ARM	Atmospheric Radiation Measurement
ASIAA	Academia Sinica Institute of Astronomy and Astrophysics
BT	Brightness Temperature
CBH	Cloud Base Height
CBH1	First Cloud Base Height
CLW	Cloud Liquid Water
CPC	Climate Prediction Center
DJF	December, January, and February
ECMWF	European Centre for Medium-Range Weather Forecasts
GBI	Greenland Blocking Index
GIS	Greenland Ice Sheet
GISP2	Greenland Ice Sheet Project 2
GPH	Geopotential Height
HATPRO	Humidity and Temperature Profiler
HYSPLIT	Hybrid Single-Particle Lagrangian Integrated Trajectory
IC	Ice Cloud
ICECAPS	Integrated Characterization of Energy, Clouds, Atmospheric State, and Precipitation at Summit
IcePIC	Ice Particle Imaging Camera
IPCC	Intergovernmental Panel on Climate Change
IWC	Ice Water Content
IWP	Ice Water Path
JJA	June, July, August
LDS	Dendrites
LR3	Liu Three-Bullet Rosettes
LSS	Liu Sectorized Snowflakes
LWC	Liquid Water Content
LWE	Liquid Water Equivalent
LWP	Liquid Water Path
MAM	March, April, May
MASC	Multi-Angle Snowflake Camera
MIXCRA	Mixed Phase Cloud Property Retrieval Algorithm
MMCR	Millimeter Wavelength Cloud Radar
MonoRTM	Monochromatic Radiative Transfer Model
MWR	Microwave Radiometer
MWRHF	High-Frequency Microwave Radiometer
MWRRET	MWR Retrieval

NAO	North Atlantic Oscillation
NCAR	National Center for Atmospheric Research
NCEP	National Centers for Environmental Prediction
NOAA	National Oceanic and Atmospheric Administration
OD	Optical Depth
POSS	Precipitation Occurrence Sensor System
Ppu	POSS Power Units
PSD	Particle Size Distribution
PWV	Precipitable Water Vapor
RT	Radiative Transfer
SLP	Sea Level Pressure
SLR	Sea Level Rise
SOI	Successive Order of Interaction
SON	September, October, November
SSA	Single Scatter Albedo
TAWO	Temporary Atmospheric Watch Observatory
UTC	Coordinated Universal Time
VCEIL	Vaisala Ceilometer
WV	Water Vapor
Z _{PATH}	Integrated Reflectivity

Bibliography

- Abdalati, W. and Steffen, K.: Snowmelt on the Greenland ice sheet as derived from passive microwave satellite data, *Journal of Climate*, 10, 165-175, 1997.
- Ackerman, T. P. and Stokes, G. M.: The Atmospheric Radiation Measurement Program, *Physics Today*, 55, 39-44, 2003.
- Alley, R.B., Meese, D.A., Shuman, C.A., Gow, A.J., Taylor, K.C., Grootes, P.M., White, J.W.C., Ram, M., Waddington, E.D., Mayewski, P.A. and Zielinski, G.A.: Abrupt increase in Greenland snow accumulation at the end of the Younger Dryas event, *Nature*, 362, 527-529, 1993.
- Alley, R.B., Shuman, C.A., Meese, D.A., Gow, A.J., Taylor, K.C., Cuffey, K.M., Fitzpatrick, J.J., Grootes, P.M., Zielinski, G.A., Ram, M. and Spinelli, G.: Visual - stratigraphic dating of the GISP2 ice core: Basis, reproducibility, and application, *Journal of Geophysical Research: Oceans*, 102, 26367-26381, 1997.
- Alley, R.B., Clark, P.U., Huybrechts, P. and Joughin, I.: Ice-sheet and sea-level changes, *Science*, 310, 456-460, 2005.
- Appenzeller, C., Schwander, J., Sommer, S. and Stocker, T.F.: The North Atlantic Oscillation and its imprint on precipitation and ice accumulation in Greenland, *Geophysical Research Letters*, 25, 1939-1942, 1998.
- Atkinson, J.D., Murray, B.J., Woodhouse, M.T., Whale, T.F., Baustian, K.J., Carslaw, K.S., Dobbie, S., O'sullivan, D. and Malkin, T.L.: The importance of feldspar for ice nucleation by mineral dust in mixed-phase clouds, *Nature*, 498, 355, 2013.
- Bennartz, R. and Bauer, P.: Sensitivity of microwave radiances at 85–183 GHz to precipitating ice particles, *Radio Science*, 38, 8075, doi:10.1029/2002RS002626, 2003.
- Bennartz, R., Shupe, M.D., Turner, D.D., Walden, V.P., Steffen, K., Cox, C.J., Kulie, M.S., Miller, N.B. and Pettersen, C.: July 2012 Greenland melt extent enhanced by low-level liquid clouds, *Nature*, 496, p.83, 2013.
- Bromwich, D.H., Robasky, F.M., Keen, R.A. and Bolzan, J.F.: Modeled variations of precipitation over the Greenland ice sheet, *Journal of Climate*, 6, 1253-1268, 1993.
- Bromwich, D. H., Cullather, R. I., Chen, Q., and Csatho, B. M.: Evaluation of recent precipitation studies for Greenland ice sheet, *J Geophys Res-Atmos*, 103, 26007-26024, 10.1029/98jd02278, 1998.
- Bromwich, D.H., Chen, Q.S., Li, Y., and Cullather, R.I.: Precipitation over Greenland and its relation to the North Atlantic Oscillation. *Journal of Geophysical Research: Atmospheres*, 104(D18), 22103-22115, 1999.

Cadeddu, M.P., J.C. Liljegren, and Turner, D.D.: The Atmospheric Radiation Measurement (ARM) program network of microwave radiometers: Instrumentation, data, and retrievals. *Atmos. Meas. Techniq.*, 6, 2359-2372, doi:10.5194/amt-6-2359-2013, 2013.

Castellani, B. B., Shupe, M. D., Hudak, D. R., and Sheppard, B. E.: The annual cycle of snowfall at Summit, Greenland, *Journal of Geophysical Research*, 120, 6654–6668. doi:10.1002/2015JD023072, 2015.

Chen, Q.S., Bromwich, D.H. and Bai, L.: Precipitation over Greenland retrieved by a dynamic method and its relation to cyclonic activity, *Journal of Climate*, 10, 839-870, 1997.

Church, J. A.: Changes in sea level, *Climate Change 2001: The Scientific Basis*. Cambridge University Press, 639–693, 2001.

Clough, S.A., Shephard, M.W., Mlawer, E.J., Delamere, J.S., Iacono, M.J., Cady-Pereira, K., Boukabara, S. and Brown, P.D.: Atmospheric radiative transfer modeling: a summary of the AER codes, *Journal of Quantitative Spectroscopy and Radiative Transfer*, 91(2), 233-244, 2005.

Compo, G.P., J.S. Whitaker, P.D. Sardeshmukh, N. Matsui, R.J. Allan, X. Yin, B.E. Gleason, R.S. Vose, G. Rutledge, P. Bessemoulin, S. Brönnimann, M. Brunet, R.I. Crouthamel, A.N. Grant, P.Y. Groisman, P.D. Jones, M. Kruk, A.C. Kruger, G.J. Marshall, M. Maugeri, H.Y. Mok, Ø. Nordli, T.F. Ross, R.M. Trigo, X.L. Wang, S.D. Woodruff, and Worley, S.J.: The Twentieth Century Reanalysis Project. *Quarterly J. Roy. Meteorol. Soc.*, 137, 1-28, 2011.

Crewell, S. and Löhnert, U.: Accuracy of cloud liquid water path from ground-based microwave radiometry 2. Sensor accuracy and synergy, *Radio Science*, 38, 8042–8051. doi:10.1029/2002RS002634, 2003.

Crewell, S., Ebell, K., Löhnert, U., and Turner, D. D.: Can liquid water profiles be retrieved from passive microwave zenith observations? *Geophysical Research Letters*, 36, L06803. doi:10.1029/2008GL036934, 2009.

Curry, J.A., Hobbs, P.V., King, M.D., Randall, D.A., Minnis, P., Isaac, G.A., Pinto, J.O., Uttal, T., Bucholtz, A., Cripe, D.G. and Gerber, H.: FIRE Arctic clouds experiment, *Bulletin of the American Meteorological Society*, 81, 5-29, 2000.

Dansgaard, W., Johnsen, S. J., Clausen, H. B., Dahl-Jensen, D., Gundestrup, N. S., Hammer, C. U., Hvidberg, C. S., Steffensen, J. P., Sveinbjörnsdottir, A. E., Jouzel, J., and Bond, G.: Evidence for general instability of past climate from a 250-kyr ice-core record. *Nature*, 364, 218-220, 1993.

- de Boer, G., Eloranta, E.W. and Shupe, M.D.: Arctic mixed-phase stratiform cloud properties from multiple years of surface-based measurements at two high-latitude locations, *Journal of the Atmospheric Sciences*, 66, 2874-2887, 2009.
- Deeter, Merritt N., and K. Franklin Evans.: A novel ice-cloud retrieval algorithm based on the Millimeter-Wave Imaging Radiometer (MIR) 150-and 220-GHz channels, *Journal of Applied Meteorology*, 39 (5), 623-633, 2000.
- Dee, D. P., and 35 co-authors: The ERA-Interim reanalysis: configuration and performance of the data assimilation system. *Quarterly Journal of the Royal Meteorological Society*, 137, 553–597. doi:10.1002/qj.828, 2011.
- Dolan, B. and Rutledge, S.A.: A theory-based hydrometeor identification algorithm for X-band polarimetric radars, *Journal of Atmospheric and Oceanic Technology*, 26, 2071-2088, 2009.
- Edwards-Opperman, J., S. Cavallo, and D.D. Turner, 2017: The occurrence and properties of long-lived liquid bearing clouds over the Greenland Ice Sheet and their relationship to the North Atlantic Oscillation. *J. Appl. Meteor. Clim.*, submitted.
- Fang, Z.F.: Statistical relationship between the northern hemisphere sea ice and atmospheric circulation during wintertime, *Observation, Theory and Modeling of Atmospheric Variability*, 131-141, 2004.
- Field, P. R., Hogan, R. J., Brown, P. R. A., Illingworth, A. J., Choulaton, T. W., and Cotton, R.: Parameterization of ice-particle size distributions for mid-latitude stratiform cloud, *Quarterly Journal of the Royal Meteorological Society*, 131, 1997-2017, doi:10.1256/qj.04.134, 2005.
- Field, P. R., Heymsfield, A. J., and Bansmer, A.: Snow Size Distribution Parameterization for Midlatitude and Tropical Ice Clouds, *Journal of the Atmospheric Sciences*, 64, 4346-4365, 2007.
- Francis, J.A. and Hunter, E.: New insight into the disappearing Arctic sea ice. *Eos, Transactions American Geophysical Union*, 87, 509-511, 2006.
- Frisch, A. D., Lenschow, D. H., Fairall, C. W., Schubert, W. H., and Gibson, J. S.: Doppler Radar Measurements of Turbulence in Marine Stratiform Cloud during ASTEX, *Journal of the Atmospheric Sciences*, 52, 2800-2808, 1995.
- Garrett, T. J., Fallgatter, C., Shkurko, K., and Howlett, D.: Fall speed measurement and high-resolution multi-angle photography of hydrometeors in free fall, *Atmospheric Measurement Techniques*, 5, 2625-2633, 2012.
- Gregory, J.M., Huybrechts, P. and Raper, S.C.: Climatology: Threatened loss of the Greenland ice-sheet, *Nature*, 428, 616-616, 2004.

- Grootes, P.M. and Stuiver, M.: Oxygen 18/16 variability in Greenland snow and ice with 10– 3 - to 105 - year time resolution, *Journal of Geophysical Research: Oceans*, 102, 26455-26470, 1997.
- Hanna, E., McConnell, J., Das, S., Cappelen, J., and Stephens, A.: Observed and modeled Greenland ice sheet snow accumulation, 1958–2003, and links with regional climate forcing. *Journal of Climate*, 19, 344-358, 2006.
- Hanna, E., Cropper, T.E., Hall, R.J. and Cappelen, J.: Greenland Blocking Index 1851–2015: a regional climate change signal, *International Journal of Climatology*, 36, 4847-4861, 2016.
- Heidinger, A. K., O'Dell, C. W., Bennartz, R., and Greenwald, T.: The Successive-Order-of-Interaction Radiative Transfer Model. Part I: Model Development, *Journal of Applied Meteorology and Climatology*, 45, 1388-1402, 2006.
- Held, I.M. and Soden, B.J.: Robust responses of the hydrological cycle to global warming, *Journal of climate*, 19, 5686-5699, 2006.
- Hobbs, P.V. and Rangno, A.L.: Microstructures of low and middle - level clouds over the Beaufort Sea, *Quarterly Journal of the Royal Meteorological Society*, 124, 2035-2071, 1998.
- Holton, J.: *An Introduction to Dynamical Meteorology*, Fourth Edition, 151 – 155, 2004.
- Hong G., Heygster, G., Miao, J., and Kunzi, K.: Detection of tropical deep convective clouds from AMSU-B water vapor channels measurements, *Journal of Geophysical Research*, 110, D05205, doi:10.1029/2004JD004949, 2005.
- Hurrell, J.W.: Decadal trends in the North Atlantic Oscillation: regional temperatures and precipitation, *Science-AAAS-Weekly Paper Edition*, 269, 676-678, 1995.
- Hutterli, M.A., Raible, C.C. and Stocker, T.F.: Reconstructing climate variability from Greenland ice sheet accumulation: An ERA40 study, *Geophysical Research Letters*, 32, 2005.
- Huybrechts, P., Letreguilly, A. and Reeh, N.: The Greenland ice sheet and greenhouse warming. *Global and Planetary Change*, 3, 399-412, 1991.
- Intrieri, J.M. and Shupe, M.D.: Characteristics and radiative effects of diamond dust over the western Arctic Ocean region, *Journal of climate*, 17, 2953-2960, 2004.
- Intrieri, J.M., Shupe, M.D., Uttal, T. and McCarty, B.J.: An annual cycle of Arctic cloud characteristics observed by radar and lidar at SHEBA, *Journal of Geophysical Research: Oceans*, 107, 2002.

Johnson, B. T., Petty, G. W., and Skofronick-Jackson, G.: Microwave Properties of Ice-Phase Hydrometeors for Radar and Radiometers: Sensitivity to Model Assumptions, *Journal of Applied Meteorology and Climatology*, 51, 2152-2171, 2012.

Kalnay, E., Kanamitsu, M., Kistler, R., Collins, W., Deaven, D., Gandin, L., Iredell, M., Saha, S., White, G., Woollen, J. and Zhu, Y.: The NCEP/NCAR 40-year reanalysis project. *Bulletin of the American Meteorological Society*, 77, 437-471, 1996.

Kapsner, W.R., Alley, R.B., Shuman, C.A., Anandakrishnan, S., and Grootes, P.M.: Dominant influence of atmospheric circulation on snow accumulation in Greenland over the past 18,000 years, *Nature*, 373, 52-54, 1995.

Kay, J.E., L'Ecuyer, T., Gettelman, A., Stephens, G. and O'Dell, C.: The contribution of cloud and radiation anomalies to the 2007 Arctic sea ice extent minimum. *Geophysical Research Letters*, 35, L08503, 2008.

Kay, J.E., L'Ecuyer, T., Chepfer, H., Loeb, N., Morrison, A. and Cesana, G.: Recent advances in Arctic cloud and climate research, *Current Climate Change Reports*, 2, 159-169, 2016.

Kintisch, E.: Meltdown, *Science*, 355, 788-791, 2017.

Kneifel, S., Löhnert, U., Battaglia, A., Crewell, S., and Siebler, D.: Snow scattering signals in ground based passive microwave radiometer measurements, *Journal of Geophysical Research*, 115, D16214, doi:10.1029/2010JD013856, 2010.

Kneifel, S., Bennartz, R., and Kulie, M. S.: A triple - frequency approach to retrieve microphysical snowfall parameters, *Journal of Geophysical Research*, 116, D11203, doi:10.1029/2010JD015430, 2011.

Kollias, P. and coauthors: Development and applications of ARM millimeter-wavelength cloud radars. *The Atmospheric Radiation Measurement Program: The First 20 Years*, Meteor. Monograph, 57, Amer. Meteor. Soc., 17.1-17.19, 2016.

Korolev, A.V., Isaac, G.A. and Hallett, J.: Ice particle habits in Arctic clouds, *Geophysical research letters*, 26, 299-1302, 1999.

Kulie, M.S. and Bennartz, R.: Utilizing spaceborne radars to retrieve dry snowfall, *Journal of Applied Meteorology and Climatology*, 48, 2564-2580, 2009.

Kulie, M. S., Bennartz, R., Greenwald, T., Chen, Y., and Weng, F.: Uncertainties in Microwave Properties of Frozen Precipitation: Implications for Remote Sensing and Data Assimilation, *Journal of Atmospheric Science*, 67, 3471-3487, 2010.

- Kulie, M.S., Milani, L., Wood, N.B., Tushaus, S.A., Bennartz, R., and L'Ecuyer, T.S.: A Shallow Cumuliform Snowfall Census Using Spaceborne Radar. *Journal of Hydrometeorology*, 17, 1261-1279, 2016.
- Lawson, R.P., Baker, B.A., Schmitt, C.G. and Jensen, T.L.: An overview of microphysical properties of Arctic clouds observed in May and July 1998 during FIRE ACE, *Journal of Geophysical Research: Atmospheres*, 106, 14989-15014, 2001.
- Lawson, R.P., Baker, B., Pilson, B. and Mo, Q.: In situ observations of the microphysical properties of wave, cirrus, and anvil clouds. Part II: Cirrus clouds, *Journal of the atmospheric sciences*, 63, 3186-3203, 2006.
- Lemke, P., Ren, J., Alley, R.B., Allison, I., Carrasco, J., Flato, G., Fujii, Y., Kaser, G., Mote, P., Thomas, R.H. and Zhang, T.: Observations: Changes in Snow, Ice and Frozen Ground, *Climate Change 2007: The Physical Science Basis. Contribution of Working Group I to the Fourth Assessment Report of the Intergovernmental Panel on Climate Change*, Cambridge University Press, 2007.
- Libbrecht, Kenneth. *The Art of the Snowflake: A Photographic Album*. Voyageur Press, 2007.
- Liebe, H., Hufford, G., and Manabe, T.: A model for the permittivity of water at frequencies below 1 THz, *International Journal of Infrared Millimeter and Terahertz Waves*, 12, 659-675, 1991.
- Liu, G.: A database of microwave single-scattering properties for nonspherical ice particles, *Bulletin of the American Meteorological Society*, 89, 1563-1570, 2008.
- Matrosov, S.Y.: Modeling backscatter properties of snowfall at millimeter wavelengths. *Journal of the atmospheric sciences*, 64, 1727-1736, 2007.
- Löhnert, U. and Crewell, S.: Accuracy of cloud liquid water path from ground-based microwave radiometry, 1, Dependency on cloud model statistics, *Radio Science*, 38(3), 8041, doi:10.1029/2002RS002654, 2003.
- Matrosov, S.Y.: Modeling backscatter properties of snowfall at millimeter wavelengths, *Journal of the atmospheric sciences*, 64, 1727-1736, 2007.
- Matrosov, S.Y., Reinking, R.F., Kropfli, R.A., Martner, B.E. and Bartram, B.W.: On the use of radar depolarization ratios for estimating shapes of ice hydrometeors in winter clouds, *Journal of Applied Meteorology*, 40, 479-490, 2001.
- Matsushita, S., Chen, M., Martin-Cocher, P., Asada, K., Chen, C., Inoue, M., Paine, S., Turner, D. D., and Steinbring, E.: 225 GHz Atmospheric Opacity Measurements from Two Arctic Sites, *Astrophysics from Antarctica Proceedings IAU Symposium*, doi:10.1017/S1743921312016882, 2013.

McClatchy, R. A., Fenn, R. W., Selby, J., Volz, F. E., and Garing, J. S.: Optical Properties of the Atmosphere, 1–113, 1972.

McIlhattan, E.A., L'Ecuyer, T.S. and Miller, N.B.: Observational evidence linking arctic supercooled liquid cloud biases in CESM to snowfall processes, *Journal of Climate*, 30, 4477-4495, 2017.

McMillan, M., Leeson, A., Shepherd, A., Briggs, K., Armitage, T.W., Hogg, A., Kuipers Munneke, P., Broeke, M., Noël, B., Berg, W.J. and Ligtenberg, S.: A high - resolution record of Greenland mass balance, *Geophysical Research Letters*, 43, 7002-7010, 2016.

Meese, D.A., Alley, R.B., Gow, T., Grootes, P.M., Mayewski, P., Ram, M., Taylor, K., Waddington, E. and Zielinski, G.: Preliminary depth-age scale of the GISP2 ice core, *Special CRREL Report*, 94, 1994.

Miller, N.B., Shupe, M.D., Cox, C.J., Walden, V.P., Turner, D.D. and Steffen, K.: Cloud radiative forcing at Summit, Greenland, *Journal of Climate*, 28, 6267-6280, 2015.

Moran, K. P., Martner, B., Post, M. J., Kropfli, R. A., Welsh, D. C., and Widener, K. B.: An unattended cloud-profiling radar for use in climate research, *Bulletin of the American Meteorological Society*, 79, 443–455, 1998.

Morlighem, M., Rignot, E., Mouginot, J., Seroussi, H., and Larour, E.: IceBridge BedMachine Greenland, Version 2, Ice Surface Elevation. Boulder, Colorado USA: NASA DAAC at the National Snow and Ice Data Center, doi:10.5067/AD7B0HQNSJ29, 2015.

Morrison, H., De Boer, G., Feingold, G., Harrington, J., Shupe, M.D., and Sulia, K.: Resilience of persistent Arctic mixed-phase clouds. *Nature Geoscience*, 5, 11-13, 2012.

Mosley - Thompson, E., Readinger, C.R., Craigmile, P., Thompson, L.G. and Calder, C.A.: Regional sensitivity of Greenland precipitation to NAO variability, *Geophysical research letters*, 32, 2005.

Mote, T.L.: Greenland surface melt trends 1973–2007: Evidence of a large increase in 2007, *Geophysical Research Letters*, 34, 2007.

Neff, W., Compo, G.P., Martin Ralph, F. and Shupe, M.D.: Continental heat anomalies and the extreme melting of the Greenland ice surface in 2012 and 1889, *Journal of Geophysical Research: Atmospheres*, 119, 6520-6536, 2014.

Nghiem, S.V., Hall, D.K., Mote, T.L., Tedesco, M., Albert, M.R., Keegan, K., Shuman, C.A., DiGirolamo, N.E. and Neumann, G.: The extreme melt across the Greenland ice sheet in 2012, *Geophysical Research Letters*, 39, 2012.

Nicholls, R.J. and Cazenave, A.: Sea-level rise and its impact on coastal zones, *Science*, 328, 1517-1520, 2010.

O'Dell, C. W., Heidinger, A. K., Greenwald, T., Bauer, P., and Bennartz, R.: The Successive-Order-of-Interaction Radiative Transfer Model. Part II: Model Performance and Applications, *Journal of Applied Meteorology and Climatology*, 45, 1403-1413, 2006.

Oue, M., Kumjian, M.R., Lu, Y., Verlinde, J., Aydin, K. and Clothiaux, E.E.: Linear depolarization ratios of columnar ice crystals in a deep precipitating system over the Arctic observed by zenith-pointing Ka-band Doppler radar, *Journal of Applied Meteorology and Climatology*, 54, 1060-1068, 2015.

Payne, V.H., J.S. Delamere, K.E. Cady-Pereira, R.R. Gamache, J.-L. Moncet, E.J. Mlawer, and Clough, S.A.: Air-broadened half-widths of the 22- and 183-GHz water-vapor lines. *IEEE Trans. Geosci. Remote Sens.*, 46, 3601-3617, 2008.

Payne, V.H., E.J. Mlawer, K.E. Cady-Pereira, and Moncet, J.-L.: Water vapor continuum absorption in the microwave. *IEEE Trans. Geosci. Remote Sens.*, 49, 2194-2208, doi:10.1109/TGRS.2010.2091416, 2011.

Pettersen, C., Bennartz, R., Kulie, M. S., Merrelli, A. J., Shupe, M. D., and Turner, D. D.: Microwave signatures of ice hydrometeors from ground-based observations above Summit, Greenland, *Atmos. Chem. Phys.*, 16, 4743-4756, <https://doi.org/10.5194/acp-16-4743-2016>, 2016.

Pettersen, C., Bennartz, R., Merrelli, A. J., Shupe, M. D., Turner, D. D., and Walden, V.P.: Precipitation regimes over central Greenland inferred from 5 years of ICECAPS observations, *Atmos. Chem. Phys.*, *in review*.

Petty, G. W. and Huang, W.: Microwave backscatter and extinction by soft ice spheres and complex snow aggregates, *Journal of Atmospheric Science*, 67, 769-787, 2010.

Pruppacher, H.R. and Klett, J.D.: *Microphysics of Clouds and Precipitation: Reprinted 1980*. Springer Science & Business Media, Vancouver, 2012.

Rauber, R.M. and Tokay, A.: An explanation for the existence of supercooled water at the top of cold clouds, *Journal of the atmospheric sciences*, 48, 1005-1023, 1991.

Reeh, N., Clausen, H.B., Dansgaard, W., Gundestrup, N., Hammer, C.U. and Johnsen, S.J.: Secular trends of accumulation rates at three Greenland stations, *Journal of Glaciology*, 20, 27-30, 1978.

Rignot, E., Velicogna, I., van den Broeke, M.R., Monaghan, A. and Lenaerts, J.T.: Acceleration of the contribution of the Greenland and Antarctic ice sheets to sea level rise, *Geophysical Research Letters*, 38, L05503, 2011.

Rigor, I.G., Wallace, J.M. and Colony, R.L.: Response of sea ice to the Arctic Oscillation, *Journal of Climate*, 15, 2648-2663, 2002.

Rogers, J.C., Bathke, D.J., Mosley - Thompson, E. and Wang, S.H.: Atmospheric circulation and cyclone frequency variations linked to the primary modes of Greenland snow accumulation, *Geophysical research letters*, 31, L23208, doi:10.1029/2004GL021048, 2004.

Rose, T., Crewell, S., Löhnert, U., and Simmer, C.: A network suitable microwave radiometer for operational monitoring of the cloudy atmosphere, *Atmospheric Research*, 75, 183-200, doi:10.1016/j.atmosres.2004.12.005, 2005.

Schiller, C., Krämer, M., Afchine, A., Spelten, N. and Sitnikov, N.: Ice water content of Arctic, midlatitude, and tropical cirrus, *Journal of Geophysical Research: Atmospheres*, 113, 2008.

Schuenemann, K.C. and Cassano, J.J.: Changes in synoptic weather patterns and Greenland precipitation in the 20th and 21st centuries: 1. Evaluation of late 20th century simulations from IPCC models, *Journal of Geophysical Research: Atmospheres*, 114, 2009.

Schuenemann, K.C., Cassano, J.J. and Finnis, J.: Synoptic forcing of precipitation over Greenland: Climatology for 1961–99, *Journal of Hydrometeorology*, 10, 60-78, 2009.

Schuenemann, K.C. and Cassano, J.J.: Changes in synoptic weather patterns and Greenland precipitation in the 20th and 21st centuries: 2. Analysis of 21st century atmospheric changes using self - organizing maps, *Journal of Geophysical Research: Atmospheres*, 115, 2010.

Screen, J.A. and Simmonds, I.: The central role of diminishing sea ice in recent Arctic temperature amplification, *Nature*, 464, 1334, 2010.

Serreze, M.C. and Barry, R.G.: *The Arctic climate system*, Cambridge University Press, 2014.

Serreze, M.C., Holland, M.M. and Stroeve, J.: Perspectives on the Arctic's shrinking sea-ice cover, *Science*, 315, 1533-1536, 2007.

Sheppard, B.E. and Joe, P.I.: Performance of the precipitation occurrence sensor system as a precipitation gauge. *Journal of Atmospheric and Oceanic Technology*, 25, 196-212, 2008.

Shuman, C.A., Bindschadler, R.A., Fahnestock, M.A., Alley, R.B. and Stearns, C.: Composite temperature record from the Greenland summit, 1987–1994: Synthesis of multiple automatic weather station records and SSM/I brightness temperatures, *Journal of climate*, 9, 1421-1428, 1996.

Shupe, M.D., Kollias, P., Persson, P.O.G. and McFarquhar, G.M.: Vertical motions in Arctic mixed-phase stratiform clouds, *Journal of the Atmospheric Sciences*, 65,1304-1322, 2006.

Shupe, M.D., Daniel, J.S., De Boer, G., Eloranta, E.W., Kollias, P., Luke, E.P., Long, C.N., Turner, D.D., and Verlinde, J.: A focus on mixed-phase clouds: The status of ground-based observational methods. *Bulletin of the American Meteorological Society*, 89, 1549-1562, 2008.

Shupe, M. D., Walden, V. P., Eloranta, E., Uttal, T., Campbell, J. R., Starkweather, S. M., and Shiobara, M.: Clouds at Arctic atmospheric observatories, Part I. Occurrence and macrophysical properties, *Journal of Applied Meteorology and Climatology*, 50, 626-644, 2011.

Shupe, M. D., Turner, D. D., Walden, V. P., Bennartz, R., Cadeddu, M., Castellani, B. B., Cox, C. J., Hudak, D. R., Kulie, M. S., Miller, N. B., Neely, R. R., Neff, W. D., and Rowe, P. M.: High and Dry: New Observations of Tropospheric and Cloud Properties above the Greenland Ice Sheet, *Bulletin of the American Meteorological Society*, 94, 169-186, 2013.

Solomon, A., Shupe, M.D., Persson, P.O.G. and Morrison, H.: Moisture and dynamical interactions maintaining decoupled Arctic mixed-phase stratocumulus in the presence of a humidity inversion, *Atmospheric Chemistry and Physics*, 11, 10127-10148, 2011.

Spencer, R.W., Goodman, H.M. and Hood, R.E.: Precipitation retrieval over land and ocean with the SSM/I: Identification and characteristics of the scattering signal, *Journal of Atmospheric and Oceanic Technology*, 6, 254-273, 1989.

Stein, A.F., Draxler, R.R., Rolph, G.D., Stunder, B.J., Cohen, M.D. and Ngan, F.: NOAA's HYSPLIT atmospheric transport and dispersion modeling system, *Bulletin of the American Meteorological Society*, 96(12), 2059-2077, 2015.

Stephens, G.L., Vane, D.G., Boain, R.J., Mace, G.G., Sassen, K., Wang, Z., Illingworth, A.J., O'Connor, E.J., Rossow, W.B., Durden, S.L. and Miller, S.D.: The CloudSat mission and the A-Train: A new dimension of space-based observations of clouds and precipitation, *Bulletin of the American Meteorological Society*, 83, 1771-1790, 2002.

Stroeve, J.C., Serreze, M.C., Holland, M.M., Kay, J.E., Malanik, J. and Barrett, A.P.: The Arctic's rapidly shrinking sea ice cover: a research synthesis. *Climatic Change*, 110, 1005-1027, 2012.

Taylor, K.C., Lamorey, G.W., Doyle, G.A., Alley, R.B., Grootes, P.M., Mayewski, P.A., White, J.W.C. and Barlow, L.K.: The 'flickering switch' of late Pleistocene climate change, *Nature*, 361, 432-436, 1993.

Tedesco, M., Fettweis, X., Van den Broeke, M. R., Van de Wal, R. S. W., Smeets, C. J. P. P., van de Berg, W. J., Serreze, M. C., and Box, J. E.: The role of albedo and accumulation in the 2010 melting record in Greenland, *Environmental Research Letters*, 6, 014005, 2011.

Thomas, R.H.E.A., Akins, T., Csatho, B., Fahnestock, M., Gogineni, P., Kim, C. and Sonntag, J.: Mass balance of the Greenland Ice Sheet at high elevations, *Science*, 289, 426-428, 2000.

Thompson, D.W. and Wallace, J.M.: The Arctic Oscillation signature in the wintertime geopotential height and temperature fields, *Geophysical research letters*, 25, 1297-1300, 1998.

Turner, D. D., Lesht, B. M., Clough, S. A., Liljegren, J. C., Revercomb, H. E., and Tobin, D. C.: Dry bias and variability in Vaisala radiosondes: The ARM experience, *Journal of Atmospheric and Oceanic Technology*, 20, 117-132, 2003.

Turner, D. D.: Improved ground-based liquid water path retrievals using a combined infrared and microwave approach, *Journal of Geophysical Research*, 112, doi:10.1029/2007JD008530, 2007a.

Turner, D. D., Clough, S. A., Liljegren, J. C., Clothiaux, E. E., Cady-Pereira, K., and Gaustad, K. L.: Retrieving Liquid Water Path and Precipitable Water Vapor From the Atmospheric Radiation Measurement (ARM) Microwave Radiometers, *IEEE Transactions on Geoscience and Remote Sensing*, 45, 3680-3690, 2007b.

Turner, D. D., Vogelmann, A. M., Austin, R. T., Banard, J., Cady-Pereira, K., Chiu, J. C., Clough, S. A., Flynn, C., Khaiyer, M. M., Liljegren, J. C., Johnson, K., Min, Q., Minnis, P., O'Hirok, W., Wang, Z., and Wiscombe, W.: Thin liquid water clouds: Their importance and our challenge, *Bulletin of the American Meteorological Society*, 88, 177-190, 2007c.

Turner, D.D., U. Loehnert, M. Cadeddu, S. Crewell, and Vogelmann, A.: Modifications to the water vapor continuum in the microwave suggested by ground-based 150 GHz observations. *IEEE Trans. Geosci. Remote Sens.*, 47, 3326-3337, doi:10.1109/TGRS.2009.202262, 2009.

Turner, D.D., S. Kneifel, and Cadeddu, M.P.: An improved liquid water absorption model at microwave frequencies for supercooled liquid water clouds. *J. Atmos. Oceanic Technol.*, 33, 33-44, doi:10.1175/JTECH-D-15-0074.1, 2016.

Uttal, T., and 53 coauthors.: International Arctic systems for observing the atmosphere (IASOA): An international polar year legacy consortium. *Bulletin of the American Meteorological Society*, 97, 1033-1056, 2016.

van den Broeke, M., Bamber, J., Ettema, J., Rignot, E., Schrama, E., van de Berg, W.J., van Meijgaard, E., Velicogna, I. and Wouters, B.: Partitioning recent Greenland mass loss, *Science*, 326, 984-986, 2009.

Van Tricht, K., Lhermitte, S., Lenaerts, J.T., Gorodetskaya, I.V., L'Ecuyer, T.S., Noël, B., van den Broeke, M.R., Turner, D.D. and Van Lipzig, N.P.: Clouds enhance Greenland ice sheet meltwater runoff, *Nature communications*, 7, 2016.

Verlinde, J., Harrington, J.Y., Yannuzzi, V.T., Avramov, A., Greenberg, S., Richardson, S.J., Bahrmann, C.P., McFarquhar, G.M., Zhang, G., Johnson, N. and Poellot, M.R.: The mixed-phase Arctic cloud experiment. *Bulletin of the American Meteorological Society*, 88, 205-221, 2007.

Verlinde, J., Rambukkange, M.P., Clothiaux, E.E., McFarquhar, G.M. and Eloranta, E.W.: Arctic multilayered, mixed - phase cloud processes revealed in millimeter - wave cloud radar Doppler spectra, *Journal of Geophysical Research: Atmospheres*, 118, 2013.

Wang, X. and Key, J.R.: Recent trends in Arctic surface, cloud, and radiation properties from space. *Science*, 299, 1725-1728, 2003.

Wilson, T.W., Ladino, L.A., Alpert, P.A., Breckels, M.N., Brooks, I.M., Burrows, S.M., Carslaw, K.S., Huffman, J.A., Judd, C., Kilhau, W.P. and Mason, R.H.: A marine biogenic source of atmospheric ice-nucleating particles, *Nature*, 525, p.234, 2015.

Yan, B., Weng, F., and Meng, H.: Retrieval of snow surface microwave emissivity from the advanced microwave sounding unit, *Journal of Geophysical Research*, 113, D19206, doi:10.1029/2007JD009559, 2008.

Zwally, H.J., Abdalati, W., Herring, T., Larson, K., Saba, J. and Steffen, K.: Surface melt-induced acceleration of Greenland ice-sheet flow, *Science*, 297, 218-222, 2002.